

Development of Novel Titanium-Based Oxide Electrode
Materials for Sodium-Ion Batteries

July 2015

Shaohua Guo

Development of Novel Titanium-Based Oxide Electrode
Materials for Sodium-Ion Batteries

Graduate School of Systems and Information Engineering
University of Tsukuba

July 2015

Shaohua Guo

ABSTRACT

Based on low cost and rich resources, sodium-ion batteries have been regarded as a promising candidate for the next generation energy storage devices in large-scale energy application for renewable energy and smart grid. However, there are some critical drawbacks limiting its application, such as safety and stability problems. Many efforts have been made in search for electrode materials to improve sodium storage performance. Many electrode materials including layered oxides and complex polyanion frameworks in cathode side and carbon compounds and titanium-based oxides in anode side have been extensively investigated. In terms of large specific capacity and reversible deintercalation and intercalation, layered sodium oxide Na_xMeO_2 (where Me is 3d transition-metal) has always been a hot research topic over recent years. Several Na_xMeO_2 polytypes with O3, P2 and P3 structures can be obtained by chemical solid-state synthesis. In this doctoral research, we present a series of titanium-based oxide with dissimilar structures, especially for layered structures, and investigated their electrochemical performance.

Firstly, O3-type $\text{NaTi}_{0.5}\text{Ni}_{0.5}\text{O}_2$ with redox couple of $\text{Ni}^{2+}/\text{Ni}^{4+}$ is explored as a cathode material for sodium ion battery. It exhibits electrochemical activity operating at an average potential of 3.1 V (vs Na^+/Na) and delivers a reversible capacity of about 100 mAh g^{-1} with smooth charge-discharge curves. In addition, this material shows excellent cycle stability and rate capability. The cycle life of 100 cycles at a 0.2C rate can be 93%, and that of 300 cycles at 1C rate is 75%. The above results indicate its superiority as a promising positive electrode candidate for sodium ion battery.

A tunnel $\text{Na}_{0.61}\text{Ti}_{0.48}\text{Mn}_{0.52}\text{O}_2$ material is explored as cathode of sodium-ion batteries by utilizing the redox couple of $\text{Mn}^{3+}/\text{Mn}^{4+}$ for the first time. It can deliver a reversible discharge capacity of 86 mAh g^{-1} with an average voltage of 2.9 V at 0.2C rate in a sodium half cell, exhibiting good rate capability and capacity retention in the cut-off voltage of 1.5-4 V. The ex-situ XRD results in the different charge stage of the first cycle suggested that the original structure could stay unchanged before charge

to 4.0 V. These results indicate that tunnel $\text{Na}_{0.61}\text{Ti}_{0.48}\text{Mn}_{0.52}\text{O}_2$ has a great potential application in large scale energy storage.

By directly using the redox couple of $\text{Ti}^{4+}/\text{Ti}^{3+}$, we developed new layered P-type $\text{Na}_{0.6}\text{Ti}_{0.4}\text{Cr}_{0.6}\text{O}_2$ materials as negative electrode of sodium-ion batteries for the first time. The two phases with layered P2 and P3 structures are synthesized at the different heat temperature. The electrochemical performances of P2 and P3 are compared in detail by galvanostatic discharge-charge test. The similar reversible capacities are obtained in P2 and P3 electrode materials. Note that P2 phase shows more superior rate capability, longer cycle life of 77.5% capacity retention after 1000 cycles as well as possess a lower potential plateau than those of P3, demonstrating that P2 is very suitable anode candidate for large scale application. Two sodium sites for P2 and only one sodium site for P3 result into the completely dissimilar sodium diffusion behaviour. First principles calculation is employed to study the influence of sodium migration on the electrochemical performance in the two P-type structures. Beyond single vacancy, the migration barrier of Na ions in P2 phase is significantly reduced, corresponding to a facile Na diffusion. Consequently, the P2 phase demonstrates a higher Na-ion mobility relative to the P3 phase, which is perfectly match the experimental data.

Finally, a stable symmetric sodium-ion battery based on bipolar active material O3-type $\text{Na}_{0.8}\text{Ti}_{0.6}\text{Ni}_{0.4}\text{O}_2$ is developed. This bipolar material shows a typical O3-type layered structure, containing two electrochemically active transition metals with redox couples of $\text{Ni}^{4+}/\text{Ni}^{2+}$ and $\text{Ti}^{4+}/\text{Ti}^{3+}$, respectively. This $\text{Na}_{0.8}\text{Ni}_{0.4}\text{Ti}_{0.6}\text{O}_2$ -based symmetric cell exhibits a high voltage of 2.8 V, a reversible discharge capacity of 85 mAh g^{-1} , 75% capacity retention after 150 cycles and good rate capability. This full symmetric cell will greatly contribute to the development of room-temperature sodium-ion batteries towards safety, low cost, long life, and will stimulate further research on symmetric cells using the same active materials as both cathode and anode.

TABLE OF CONTENTS

ABSTRACT.....	1
TABLE OF CONTENTS	3
LIST OF FIGURES	5
LIST OF TABLES	12
Chapter 1. General Introduction	13
1.1 Sodium-ion batteries	13
1.1.1 Brief introduction of sodium-ion batteries.....	13
1.1.2 Composites and Working principle of sodium ion batteries	14
1.2 Cathode materials for sodium-ion batteries	15
1.2.1 Layered oxide compounds	15
1.2.2 Polyanion compounds.....	18
1.2.3 Other materials as positive electrodes.....	18
1.3 Anode materials for sodium-ion batteries.....	20
1.3.1 Carbon Compounds	20
1.3.2 Layered titanium-based oxide.....	21
1.3.3 Other materials as positive electrodes.....	23
1.4 Target and outline of this dissertation	24
1.4.1 Motivation of this research	24
1.4.2 Targets of this research	26
1.4.3 Outline of this thesis	26
Chapter 2 Layered O3-type $\text{NaTi}_{0.5}\text{Ni}_{0.5}\text{O}_2$ as positive electrode materials for sodium-ion batteries.....	29
2.1 Introduction.....	29
2.2 Experimental and Characterization.....	30
2.2.1 Preparation of O3- $\text{NaTi}_{0.5}\text{Ni}_{0.5}\text{O}_2$	30
2.2.2 Characterization	30
2.2.3 Electrochemical test	30
2.3 Results and Discussion	30
2.3.1 Structural characterization	30
2.3.2 Electrochemical performance and analysis.....	33
2.4 Conclusions.....	36
Chapter 3 Tunnel $\text{Na}_{0.61}\text{Ti}_{0.48}\text{Mn}_{0.52}\text{O}_2$ as positive electrode materials for sodium-ion batteries	38
3.1 Introduction.....	38
3.2 Experimental and Characterization.....	39
3.2.1 Preparation of tunnel $\text{Na}_{0.61}\text{Ti}_{0.48}\text{Mn}_{0.52}\text{O}_2$	39
3.2.2 Characterization	39
3.2.3 Electrochemical test	40
3.3 Results and discussion	40
3.3.1 Structural characterization	40
3.3.2 Electrochemical performance and analysis.....	42
3.4 Conclusions.....	46

Chapter 4 Layered P2 and P3-type $\text{Na}_{0.6}\text{Cr}_{0.6}\text{Ti}_{0.4}\text{O}_2$ as negative electrode materials for sodium-ion batteries.....	47
4.1 Introduction.....	47
4.2 Experimental and Characterization.....	49
4.2.1 Material preparation.....	49
4.2.2 Characterizations.....	50
4.2.3 Electrochemistry.....	50
4.2.4 First-principles calculation.....	51
4.3 Results and discussion.....	52
4.3.1 Structural characterization.....	52
4.3.2 Electrochemical performance and analysis.....	56
4.3.3 Sodium storage mechanism.....	59
4.3.4 First principles calculation.....	61
4.4 Conclusions.....	68
Chapter 5 Layered $\text{Na}_{0.8}\text{Ni}_{0.4}\text{Ti}_{0.6}\text{O}_2$ as bipolar electrode materials for sodium-ion batteries.....	69
5.1 Introduction.....	69
5.2 Experimental and Characterization.....	71
5.2.1 Preparation of O3-type $\text{Na}_{0.8}\text{Ni}_{0.4}\text{Ti}_{0.6}\text{O}_2$	71
5.2.2 Characterization.....	71
5.2.3 Electrochemical test.....	71
5.3 Results and discussion.....	72
5.3.1 Structural characterization.....	72
5.3.2 Electrochemical performance and analysis.....	77
5.3.3 Sodium storage mechanism.....	80
5.4 Conclusions.....	85
Chapter 6 conclusion.....	86
List of publication.....	89
Acknowledgement.....	91
REFERENCE.....	92

List OF FIGURES

- Figure 1.1** The abundance of chemical elements in Earth's crust (Wikipedia).
- Figure 1.2** Schematic illustration of Sodium-ion batteries.
- Figure 1.3** Crystal structure of various layered Na_xMeO_2 : (a) P2-type structure, (b) O3-type structure and (c) P3-type structure.
- Figure 1.4** Representation of diffusion paths of sodium ions in the different structures with O-type (O2 and O3) and P-type (P2 and P3) stacks. The blue and yellow balls represent the sodium and oxygen atoms, respectively. The shadow parts show the interspace between the two sites.
- Figure 1.5** Crystal structures of various polyanion compounds: (a) $\text{Na}_3\text{V}_2(\text{PO}_4)_3$, and (b) NaFePO_4 (Na: yellow, V/Fe: blue, O: red).
- Figure 1.6** (a) The charge-discharge profile of layered NaMn_3O_5 with Birnessite structure; (b) the corresponding dQ/dV plots; (c) Discharge profiles at different rates after charging at 0.1C rate. (d) The cycle profiles of layered NaMn_3O_5 at a charge/discharge rate of 0.1C.
- Figure 1.7** (a) The charge-discharge profile of $\text{Na}_{2.8}\text{MnHFC}$ with interstitial H_2O , the inset is the corresponding crystal structure. (b) The charge-discharge profile of $\text{Na}_{2.8}\text{MnHFC}$ without interstitial H_2O , the inset is the corresponding crystal structure.
- Figure 1.8** Typical discharge-charge profiles of hard-carbon electrodes, and its capacity retention is also shown in the inset.
- Figure 1.9** (a) The discharge-charge profiles of P2- $\text{Na}_{0.66}\text{Li}_{0.22}\text{Ti}_{0.78}\text{O}_2$ electrodes at a current of C/10 between 0.4 and 2.5 V. (b) Rate capability. (c) The cycling performance and Coulombic efficiency at a rate of 2C. (d) Discharge profiles of $\text{Na}_{0.66}\text{Li}_{0.22}\text{Ti}_{0.78}\text{O}_2//\text{Na}_3\text{V}_2(\text{PO}_4)_3/\text{C}$ sodium-ion full cell at various rates, Inset is the cyclic performance of the full cell at 1C rate.
- Figure 1.10** (a) The typical discharge-charge profiles of P2- $\text{Na}_{2/3}\text{Co}_{1/3}\text{Ti}_{2/3}\text{O}_2$ electrodes at a current rate of 0.2 C in the different voltage ranges. (b) Rate capability. Insert is the discharge-charge curves at different rates. (c) The discharge-charge curves at different cycles. Insert is the dQ/dV curves variation within 200 cycles. (d) Long-term cycle stability of 1000 cycles and 3000 cycles at rates of 2 C and 5 C, respectively. Insert is the related Coulombic

efficiency within 3000 cycles.

Figure 2.1 (a) XRD pattern of O3-NaNi_{0.5}Ti_{0.5}O₂ material with NiO impurity (indicated by blue short arrows). (b) XRD pattern and Rietveld refinement profile excluding NiO impurity: the observed intensities is shown in cyan circles; the calculated pattern in a red solid line; the difference in a blue curve; the position of Bragg reflections in green short vertical bars corresponding to rhombohedral NaTi_{0.5}Ni_{0.5}O₂ phase; blue arrows indicate the position of NiO phase.

Figure 2.2 Schematic illustration of the crystal structure for O3-NaTi_{0.5}Ni_{0.5}O₂ consisting of Me (metal) octahedron (blue) and Na octahedron (green).

Figure 2.3 SEM images of as-synthesized O3-NaTi_{0.5}Ni_{0.5}O₂ with different magnifications, showing apparent sheet-like morphology.

Figure 2.4 (a) Initial charge and discharge curves of the O3-NaNi_{0.5}Ti_{0.5}O₂/Na cell at a rate of 0.2 C (1C corresponds to 100 mA g⁻¹) in the voltage ranges of 2.0-4.7 V versus sodium metal. (b) The corresponding dQ/dV curves. (c) The cycling performance and the corresponding coulombic efficiency over 50 cycles.

Figure 2.5 (a) The initial charge-discharge profiles at a 0.2 C rate in the voltage ranges of 2.0-4.0 V. (b) The initial CV curves at a scan rate of 0.5 m V s⁻¹.

Figure 2.6 (a) Cycling performance and corresponding coulombic efficiency of the O3-NaNi_{0.5}Ti_{0.5}O₂/Na cells at a 0.2 C rate. (b) Rate performance of the O3-NaNi_{0.5}Ti_{0.5}O₂/Na cell at different rates of 0.2 C, 0.5 C, 1 C, 2 C, 5 C and 10 C. (c) Cycling performance and corresponding coulombic efficiency of the O3-NaNi_{0.5}Ti_{0.5}O₂/Na cells at a 1C rate.

Figure 3.1 (a) XRD pattern of tunnel Na_{0.61}Ti_{0.48}Mn_{0.52}O₂ sample and Rietveld refinement profile. (b) The schematic shows the crystal structure of Na_{0.61}Ti_{0.48}Mn_{0.52}O₂ isostructural with Na₄Mn₄Ti₅O₁₈ consisting of Ti (Mn) octahedron (blue) and Na octahedron (green).

Figure 3.2 (a) and (b) SEM images of tunnel Na_{0.61}Ti_{0.48}Mn_{0.52}O₂ sample with different magnification. (c), (d) and (e) TEM images corresponding to different crystal planes and

corresponding FFT (insets); the rectangle area in Figure 3.2e shows the analysis area of EDX maps. (f) The relative EDX analysis results.

Figure 3.3 (a) First charge-discharge profile at a 0.2C rate in the cut-off voltage of 1.5-4.7 V versus Na^+/Na . (b) The corresponding dQ/dV curve. (c) The cycling performance and corresponding coulombic efficiency.

Figure 3.4 (a) Initial charge-discharge profiles at a 0.2C rate in the cut-off voltage of 1.5-4 V. (b) The corresponding dQ/dV curves.

Figure 3.5 (a) Discharge profiles at 0.2C, 0.5C, 1C, 2C and 5C rate after charging at 0.2C rate. (b) Cycle performance and coulombic efficiency at a 0.2C rate.

Figure 3.6 Ex-situ XRD patterns for tunnel $\text{Na}_{0.61}\text{Ti}_{0.48}\text{Mn}_{0.52}\text{O}_2$ electrode with the voltage range of 1.5-4.7 V in the initial charge process. The peak position and corresponding lattice plane is marked in the inset. On the right, the corresponding voltages for ex-situ XRD measurement are indicated.

Figure 4.1 Classification of layered sodium oxides (Na_xMeO_2), electrochemical phase-transition induced by sodium extraction and Na ions migration paths in different layered structures. Note that P2-phase more easily maintain its original structure, while O3-phase always transforms to P3-phase during sodiation process. The yellow and blue balls represent the sodium and transition-metal atoms, respectively. The red circles and shadow parts indicate the intermediate site during sodium diffusion and the interspace between the two sites, respectively. The red lines below show the direct Na migration for P2- and P3-phases, and the indirect migration for O2- and O3-phases.

Figure 4.2 XRD patterns of $\text{Na}_{0.6}\text{Ti}_{0.4}\text{Cr}_{0.6}\text{O}_2$ materials at different heat temperatures, and the dotted lines indicate an overlapping of the (00 l) reflections for both layered P-type phases.

Figure 4.3 Structure of P-type NTCO materials. (a) XRD and Rietveld plots of P2-NTCO compounds with experimental data in black dots, calculated curves in red and difference curve in blue, and standard Bragg reflections in pink short vertical bars. (b) P2-type crystal structure viewed along a-axis showing the two different Na ions sites by green and yellow colors. (c)

P2-type crystal structure viewed along c-axis showing that every Na^I (edge-sharing) site is surrounded by the three Na^{II} (face-sharing) site, while every Na^{II} site is surrounded by the three Na^I sites. **(d)** XRD and Rietveld plots for refined P3-NTCO with experimental data in black dots, calculated curves in red and difference curve in blue, and standard Bragg reflections in pink short vertical bars. **(e)** P3-type crystal structure viewed along a-axis showing the only one Na ions site by green-yellow color. **(f)** P3-type crystal structure viewed along c-axis showing that every Na site is edge-sharing in one side, and face-sharing in the other side. Note that part of sodium prisms are open to show short distances between sodium sites which cannot be occupied simultaneously.

Figure 4.4 STEM imaging of P-type NTCO materials. **(a)** experimental SAED patterns of P2-NTCO viewed along [010] zone axis. **(b)** simulated SAED patterns of P2-NTCO viewed along [010] direction. **(c)** HADDF-STEM image of P2-NTCO. **(d)** ABF-STEM image of P2-NTCO. **(e)** experimental SAED patterns of P3-NTCO viewed along [010] zone axis. **(f)** simulated SAED patterns of P3-NTCO viewed along [010] direction. **(g)** HADDF-STEM image of P3-NTCO. **(h)** ABF-STEM image of P2-NTCO. **(i)** and **(j)** enlarged ABF-STEM image extracted from **(C)** and **(D)**, showing the ABBAAB stacking of P2. **(k)** and **(l)** enlarged ABF-STEM image extracted from **(G)** and **(H)**, showing the ABBCCAAB stacking of P2.

Figure 4.5 The electrochemical performance of P2- and P3-NTCO compounds. **(a)** The typical charge-discharge profiles between 0.15 and 2.5 V region at a 0.2C rate (1C rate corresponding to 100 mA g⁻¹). **(b)** The rate capability at different rates of 0.2C, 0.5C, 1C, 2C, 5C, and 10C. **(c)** The plots of reversible capacity versus C rates. **(d)** The cycling performance with Coulombic efficiency of 400 cycles at a 5C rate. **(e)** The cycling performance with Coulombic efficiency of 1000 cycles only for P2-NTCO at a 5C rate.

Figure 4.6 **(a)** The first discharge-charge profile of P2-NTCO. **(b)** The first discharge-charge profile of P3-NTCO. **(c)** The typical dQ/dV curves of P2-NTCO. **(d)** The typical dQ/dV curves of P3-NTCO.

Figure 4.7 **(a)** The ex-situ XRD of fully sodiated (discharge to 0.15 V) P2-NTCO. The standard Bragg reflections of P2 phase are shown in pink short vertical bars. **(b)** The ex-situ XRD of fully sodiated (discharge 0.15 V) P3-NTCO. The standard Bragg reflections of P3 phase are shown in pink short vertical bars. The red inverted triangles indicate the broaden reflections resulted from the sealed Kapton film of ex-situ XRD test, and the blue inverted triangles

correspond to the reflections resulted from Al substrate.

Figure 4.8 The EELS analysis showing the remarkable valence change of titanium in P2- and P3-NTCO compounds. **(a)** EELS mapping of the pristine P2-NTCO, and the white rectangle of STEM image indicates the analysis area. Atomic resolution STEM-EELS line scanning of Ti and Cr along the c-axis before and after discharge is observed in the colourful images. **(b)** EELS mapping of the pristine P3-NTCO, and the white rectangle of STEM image indicates the analysis area. Atomic resolution STEM-EELS line scanning of Ti and Cr along the c-axis before and after discharge is observed in the colourful images. **(c)** the high-resolution EELS profiles of P2- and P3-NTCO compounds.

Figure 4.9 **(a)** 2D view of the Na layer for both P2 and P3 phases. The $\text{Na}^{\text{I}}\text{O}_6$ and $\text{Na}^{\text{II}}\text{O}_6$ prisms are represented by green and yellow colors, respectively. **(b)** the schematic of sodium diffusion path under single vacancy approximation. **(c)** the calculated energy barriers and trajectories of Na-ion diffusion under single vacancy approximation of P2 structure. **(d)** the calculated energy barriers and trajectories of Na-ion diffusion under single vacancy approximation of P3 structure. **(e)** Na layer configurations with two adjacent Na^{II} site vacancies before relaxation. **(f)** Na layer configurations with two adjacent Na^{II} site vacancies after relaxation, showing that all Na ions are “fixed” in the case of divacancy.

Figure 4.10 Calculated energy barriers and trajectories of Na-ion diffusion in P2- and P3- NaTiO_2 . **(a)** Schematic of Na-ion diffusion path in layered P-type structures in the case of three Na vacancies. The $\text{Na}^{\text{I}}\text{O}_6$ and $\text{Na}^{\text{II}}\text{O}_6$ prisms are represented by green and yellow colors, respectively. **(b)** Na-ion diffusion barrier of P2-type phase under condition of three Na vacancies. **(c)** Na-ion diffusion barrier of P3-type phase under condition of three Na vacancies. **(d)** Schematic of Na-ion diffusion path in layered P-type structures in the case of four Na vacancies. **(e)** Na-ion diffusion barrier of P2-type phase under condition of three Na vacancies. **(f)** Na-ion diffusion barrier of P3-type phase under condition of three Na vacancies.

Figure 4.11 Calculated energy barrier of Na ion diffusion process, in the case of three vacancies (3v) and four vacancies (4v), in NaTiO_2 (solid bars) and $\text{NaTi}_{0.44}\text{Cr}_{0.56}\text{O}_2$ (shaded bars) with layered P2 (green) and P3 (orange) structures.

Figure 4.12 **(a)** GITT potential profiles of layered P2-NTCO in the second discharge-charge process at the current density of 6 mA g^{-1} with the time interval of 3h. **(b)** GITT potential profiles

of layered P3-NTCO in the second discharge-charge process at the current density of 6 mA g^{-1} with the time interval of 3h. (c) diffusion coefficients of Na^+ in layered P2-NTCO at different discharge-charge states. (d) diffusion coefficients of Na^+ in layered P3-NTCO at different discharge-charge states.

Figure 5.1 (a) A diagram of the proposed symmetric cell based on O3-type $\text{Na}_{0.8}\text{Ni}_{0.4}\text{Ti}_{0.6}\text{O}_2$. (b) schematic of energy vs. density of states plot, showing the relative positions of the Fermi energy level of $\text{Ni}^{4+}/\text{Ni}^{2+}$ ($\text{Ni}^{4+}/\text{Ni}^{3+}$ and $\text{Ni}^{3+}/\text{Ni}^{2+}$) and $\text{Ti}^{4+}/\text{Ti}^{3+}$ redox couples for O3-type $\text{Na}_{0.8}\text{Ni}_{0.4}\text{Ti}_{0.6}\text{O}_2$. (c) The CV curve of $\text{Na}_{0.8}\text{Ni}_{0.4}\text{Ti}_{0.6}\text{O}_2/\text{Na}$ half cell in the whole voltage range of 0-4 V vs. Na^+/Na , and the background shows the lighted LED bulbs driven up by the designed bipolar $\text{Na}_{0.8}\text{Ni}_{0.4}\text{Ti}_{0.6}\text{O}_2$ -based symmetric cells.

Figure 5.2 (a) HR-SXRD pattern and Rietveld refinement of layered $\text{Na}_{0.8}\text{Ni}_{0.4}\text{Ti}_{0.6}\text{O}_2$ material. A red line represents the observed intensities; The calculated pattern is shown with black circles; The difference between the observed and calculated intensities is presented by a blue curve; Pink short vertical bars indicate the position of standard Bragg reflections. The inset shows SEM image of $\text{Na}_{0.8}\text{Ni}_{0.4}\text{Ti}_{0.6}\text{O}_2$ samples. (b) Schematic illustration of the crystal structure for O3-type $\text{Na}_{0.8}\text{Ni}_{0.4}\text{Ti}_{0.6}\text{O}_2$.

Figure 5.3 (a) and (b) SAED patterns. (c) HADDF and (d) ABF-STEM images of $\text{Na}_{0.8}\text{Ni}_{0.4}\text{Ti}_{0.6}\text{O}_2$ samples projected along [001] direction. The insets of (d) and (e) in top-right corners shows sodium (blue balls) and transition metal (green balls) occupancies. (e) HRTEM image of $\text{Na}_{0.8}\text{Ni}_{0.4}\text{Ti}_{0.6}\text{O}_2$ samples.

Figure 5.4 The electrochemical performance of the O3-type $\text{Na}_{0.8}\text{Ni}_{0.4}\text{Ti}_{0.6}\text{O}_2$ in the half cell vs. Na^+/Na (a) The CV curves of O3-type $\text{Na}_{0.8}\text{Ni}_{0.4}\text{Ti}_{0.6}\text{O}_2$ in the voltage range of 2-4 V for $\text{Ni}^{4+}/\text{Ni}^{2+}$ (green) and 0.01-2.5 V for $\text{Ti}^{4+}/\text{Ti}^{3+}$ (brown) vs. Na^+/Na . (b) Schematic of potential of the $\text{Ni}^{4+}/\text{Ni}^{3+}$, $\text{Ni}^{3+}/\text{Ni}^{2+}$ and $\text{Ti}^{4+}/\text{Ti}^{3+}$ redox couples vs. Na/Na^+ in layered $\text{Na}_{0.8}\text{Ni}_{0.4}\text{Ti}_{0.6}\text{O}_2$ materials. The insets display the average potentials of the $\text{Na}_{0.8}\text{Ni}_{0.4}\text{Ti}_{0.6}\text{O}_2/\text{Na}$ half cells as cathode and anode, respectively. (c) The typical charge-discharge or discharge-charge profiles of the $\text{Na}_{0.8}\text{Ni}_{0.4}\text{Ti}_{0.6}\text{O}_2/\text{Na}$ half cells in the voltage range of 2-4 V (green) and 0.01-2.5 V (brown) vs. Na^+/Na . The inset (yellow parts) shows the predicted average voltage of 2.8 V in the bipolar $\text{Na}_{0.8}\text{Ni}_{0.4}\text{Ti}_{0.6}\text{O}_2$ -based symmetric cells.

Figure 5.5 (a) The initial charge profile of $\text{Na}_{0.8}\text{Ni}_{0.4}\text{Ti}_{0.6}\text{O}_2/\text{Na}$ half cells. (b) The XPS

spectra of Ni-2p peaks of the desodiated $\text{Na}_{0.8-x}\text{Ni}_{0.4}\text{Ti}_{0.6}\text{O}_2$ after initial charge process.

Figure 5.6 (a) Cycle performance and relative coulombic efficiency of $\text{Na}_{0.8}\text{Ni}_{0.4}\text{Ti}_{0.6}\text{O}_2/\text{Na}$ half cell with the voltage range of 2-4 V for 250 cycles at a 1C rate. (b) Cycle performance and relative coulombic efficiency of $\text{Na}_{0.8}\text{Ni}_{0.4}\text{Ti}_{0.6}\text{O}_2/\text{Na}$ half cell with the voltage range of 0.01-2.5 V for 250 cycles at a 1C rate.

Figure 5.7 The electrochemical performance of bipolar $\text{Na}_{0.8}\text{Ni}_{0.4}\text{Ti}_{0.6}\text{O}_2$ -based symmetric cells. (a) The CV curve in the voltage range of 0.6-3.8 V. (b) The typical charge-discharge profiles in the voltage range of 0.6-3.8 V; inset is the initial charge-discharge profile. (c) The rate capability at different rates of 0.2C, 0.5C and 1C. (d) The cycling performance with Coulombic efficiency at a 1C rate.

Figure 5.8 Structural evolution using $\text{Na}_{0.8}\text{Ni}_{0.4}\text{Ti}_{0.6}\text{O}_2$ as cathode (a) The first charge-discharge profile of the $\text{Na}_{0.8}\text{Ni}_{0.4}\text{Ti}_{0.6}\text{O}_2/\text{Na}$ half cell in a low potential area, and the green points correspond to the different charge-discharge states conducted by ex-situ XRD experiment. (b) The ex-situ XRD patterns of $\text{Na}_{0.8}\text{Ni}_{0.4}\text{Ti}_{0.6}\text{O}_2$ at the different charge-discharge states shown in a. (c) The SAED patterns and TEM image of the fully charged $\text{Na}_{0.8}\text{Ni}_{0.4}\text{Ti}_{0.6}\text{O}_2$ samples projected along $[1\bar{1}0]$ direction. (d) The expanded view in the regions of $15-17^\circ$ and $30-38^\circ$ for the ex-situ XRD patterns shown in b.

Figure 5.9 Schematic of the phase transition from O3-type $\text{Na}_{0.8}\text{Ni}_{0.4}\text{Ti}_{0.6}\text{O}_2$ to P3-type $\text{Na}_{0.8-x}\text{Ni}_{0.4}\text{Ti}_{0.6}\text{O}_2$ in the half cell of $\text{Na}_{0.8}\text{Ni}_{0.4}\text{Ti}_{0.6}\text{O}_2/\text{Na}$ with the voltage range of 2-4 V.

Figure 5.10 (a) The first discharge-charge profile of the $\text{Na}_{0.8}\text{Ni}_{0.4}\text{Ti}_{0.6}\text{O}_2/\text{Na}$ half cell, and the different colorful points correspond to the different discharge-charge states conducted by ex-situ XRD experiment. (b) The ex-situ XRD patterns of $\text{Na}_{0.8}\text{Ni}_{0.4}\text{Ti}_{0.6}\text{O}_2$ at the different discharge-charge states shown in a.

Figure 5.11 (a) The SAED patterns (b) HAADF-STEM image and (c) ABF-STEM image of the fully discharged $\text{Na}_{0.8}\text{Ni}_{0.4}\text{Ti}_{0.6}\text{O}_2$ samples projected along $[100]$ direction. (d) and (e) The enlarged area corresponding to the white rectangle in (b) and (c), showing the typical sodium (blue) and transition metal (green) occupancies in O3 layered structure.

Figure 5.12 Differential scanning calorimetry (DSC) spectra of the pristine $\text{Na}_{0.8}\text{Ni}_{0.4}\text{Ti}_{0.6}\text{O}_2$, desodiated $\text{Na}_{0.8-x}\text{Ni}_{0.4}\text{Ti}_{0.6}\text{O}_2$ (charging to 4 V) and sodiated $\text{Na}_{0.8+y}\text{Ni}_{0.4}\text{Ti}_{0.6}\text{O}_2$ (discharging to 0.01 V).

LIST OF TABLES

Table 1.1 Sodium versus Lithium characteristics.

Table 2.1 Lattice parameters of the pristine O3-NaTi_{0.5}Ni_{0.5}O₂ sample after Rietveld refinement.

Table 3.1 Lattice parameters of tunnel Na_{0.61}Ti_{0.48}Mn_{0.52}O₂ sample after Rietveld refinement.

Table 4.1 Lattice parameters of P2 and P3-type Na_{0.6}Ti_{0.4}Cr_{0.6}O₂ samples after Rietveld refinement.

Table 4.2 Factors influencing the energy of the Na^I site relative to that of the Na^{II} site. Two major factors, i.e., the intralayer Na interaction and the transition metal repulsion, are considered. The up/down arrow indicates an increase/decrease in the relative Na^I site energy. The consequent Na^I site energy is a combination of the two factors and quantitatively represented by the blue arrow.

Table 5.1 Lattice parameters of O3-type Na_{0.8}Ni_{0.4}Ti_{0.6}O₂ sample after Rietveld refinement.

Chapter 1. General Introduction

1.1 Sodium-ion batteries

1.1.1 Brief introduction of sodium-ion batteries

Since the emergence of energy and environmental problems became more and more prominent during last decade, renewable energy such as wind and solar power has been widespread used in the modern electrical grid and are playing an increasing role in the future than ever.¹ However, renewable energy is intermittent, varying from time to time. To smooth out the intermittency of renewable energy and integrate it into the grid safely, low-cost electrical energy storage (EES) is extremely necessary.² A number of potential technologies have been proposed for the utility applications, such as pumped hydroelectric, compressed air, fly-wheel and electrochemical batteries. Among them, electrochemical batteries can efficiently store electricity in chemicals and reversibly release it as required, therefore, battery technology represent one of the most promising candidates for stationary applications. Note that, stationary batteries should be characterized by long cycle life, low cost and high safety, which is completely different from those of power batteries. As a vital component of batteries, electrode materials with abundant elements, and structural stability need to be well developed for large-scale and long-term applications.

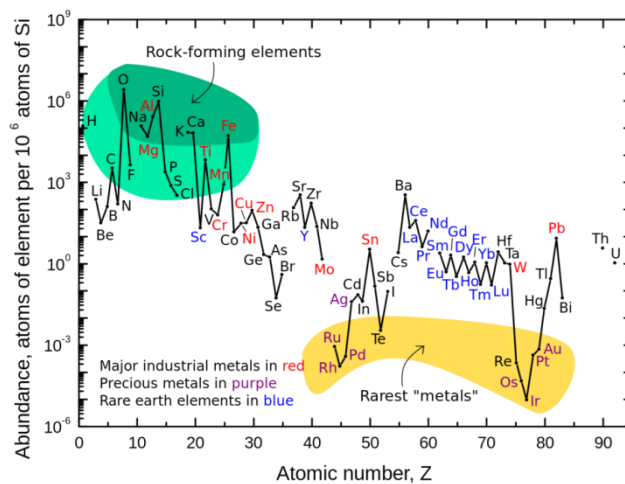


Figure 1.1 The abundance of chemical elements in Earth's crust (Wikipedia).

Due to the success in the domain of power electronics, lithium ion batteries

(LIBs) are also being considered for electric grid storage.^{3, 4} However, the worldwide demand of lithium sources might grow very rapidly with large-scale application, and the limited availability (70% lithium sources in South American) and increasing cost are unable to meet this need for large scale application. Alternative low-cost and sustainable chemistries are particularly suitable for large applications.

Figure 1.1 shows the elemental abundance in Earth's crust, and it is found that lithium abundance is only 20 ppm. In contrast, sodium resources are distributed everywhere, as sodium is the most fourth abundant elements in the Earth's crust. Vast sodium resources are also contained in the ocean. Additionally, sodium is the second-lightest and second-smallest alkali metal next to lithium. The comparison between sodium and lithium is listed in Table 1.1. Considering the abundance, distribution and their carbonate price, sodium chemistries are the ideal alternative to lithium in large scale application. Based on the wide availability and low cost of sodium, room-temperature sodium-ion batteries have the potential for meeting large scale grid energy storage needs.^{5, 6}

Table 1.1 Sodium versus Lithium characteristics.

	Na	Li
Cation radius	97 pm	68 pm
Atomic weight	23 g mol ⁻¹	6.9 g mol ⁻¹
E _o vs. SHE	-2.7 V	-3.04 V
A-O coordination	Octahedral or prismatic	Octahedral or tetrahedral
Melting point	97.7 °C	180.5 °C
Abundance	23.6 × 10 ³ mg kg ⁻¹	20 mg kg ⁻¹
Distribution	Everywhere	70% in South America
Price, carbonates	~25 Yen per kg	~800 Yen per kg

1.1.2 Composites and Working principle of sodium ion batteries

Actually, sodium-ion batteries were studied from the 1970s to the 1980s in parallel with lithium-ion batteries.⁷⁻⁹ The success of the commercial application of LIBs significantly decreased the investigation of SIBs.^{10, 11} Nowadays, owing to

sodium abundance and its low cost, the research about SIBs operated at ambient temperature attracted much attention again. Room-temperature “rocking-chair” sodium-ion batteries have the similar working principle with that of LIBs, shown in Figure 1.2.¹² Structures, components, and charge-discharge mechanisms of SIBs are essentially the same except that sodium ions take the place of lithium ions. SIBs consist of sodium insertion materials on both sides and aprotic solvent as electrolyte in the middle, therefore, can be free from sodium metal.¹³ Full sodium ion cells do not employ metallic sodium as the negative electrode: they are comprised of hard carbons or metal oxide intercalation compounds. The negative electrode is one of the most troublesome components because typical graphitic carbons employed in LIBs do not intercalate sodium ions. The finding of safe, low-cost and long-life anode materials suitable for the practical application still is a huge challenge.

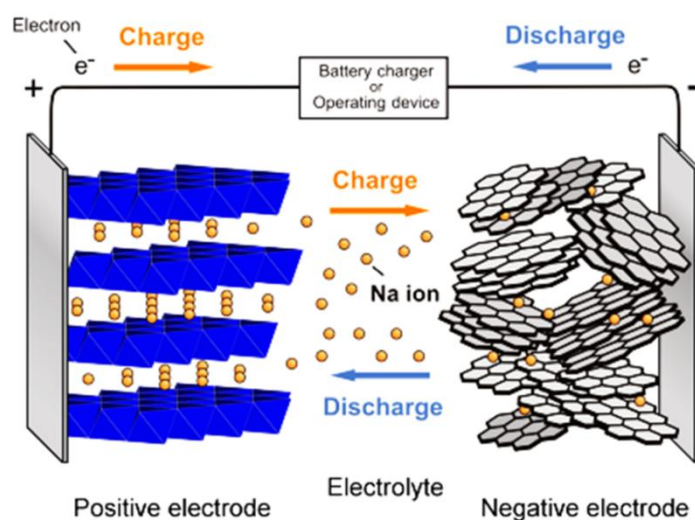


Figure 1.2 Schematic illustration of Sodium-ion batteries.¹²

1.2 Cathode materials for sodium-ion batteries

1.2.1 Layered oxide compounds

Two-dimensional layered oxides are the most important class of the positive electrode materials as evidenced by their success in commercial high-energy LIBs. Certainly, layered sodium oxides are the most extensively studied topic in the SIBs research area. In early 1980s, Delmas and co-workers have made great contribution

to layered sodium oxides (Na_xMeO_2 Me = 3d transition metals).¹⁴⁻¹⁶ The electrochemical behavior of layered compounds in SIBs frequently is different from that of the lithium counterparts in LIBs. Layered LiFeO_2 is inactive, and layered LiCrO_2 undergoes unfavorable and irreversible phase transitions after the lithium extraction in LIBs. In contrast, their sodium counterparts, all layered sodium oxide of 3d transition metals with layered structures can be highly activated as sodium insertion host.^{17, 18}

Several Na_xMeO_2 polytypes with O3, P2 and P3 structures can be obtained by chemical solid-state synthesis. According to the nomenclature proposed by Delmas et. al., symbols of O or P denote the octahedral or prismatic environment for Na sites, and symbols of 2 or 3 indicates the minimum number of transition metal layers in the repeating cell unit.¹⁹ Figure 1.3 shows the main three typical crystal structure of layered P2, O3 and P3, respectively.

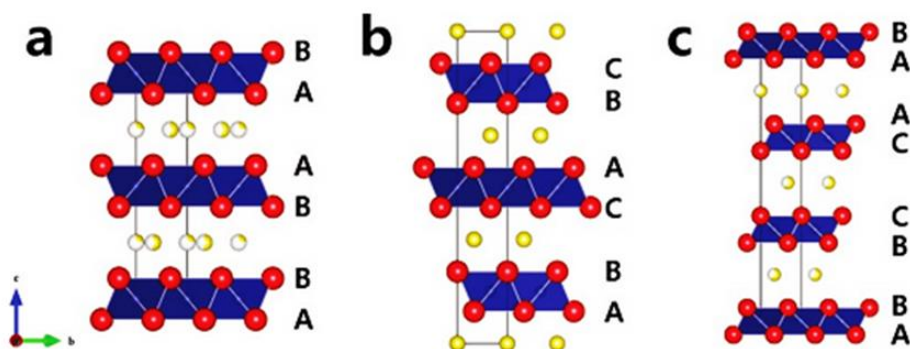


Figure 1.3 Crystal structure of various layered Na_xMeO_2 : (a) P2-type structure, (b) O3-type structure and (c) P3-type structure.⁵

Owing to the different in-plane ordering and sodium chemical environment, O3 and P2 phases have different sodium diffusion paths, shown in Figure 1.4.²⁰ Sodium migration in O3 structure must go across the intermediate sites between the adjacent sodium octahedral sites, which needs to overcome a high energy barrier and will result into the inevitable complex phase transition during extraction and insertion. Sodium ions can diffuse directly between two face-sharing trigonal prismatic sites in the sodium layers. Therefore, P2 phase always show better rate capability and easily

maintain the original structure during sodium migration, while O3 phase often undergoes the complex phase transition due to the intervention of intermediate sites.²¹

O3 phase is empirically known to be stabilized with a sodium-sufficient condition (in general, $x = 1$ in Na_xMeO_2), associated with a large theoretical capacity. P2-type layered materials are thermodynamically stabilized under a sodium-deficient condition (in general, $x = 0.7$ in Na_xMeO_2). Therefore, a large capacity for P2 phase is only achieved after the compensation of deficient sodium ions in the structure.²² Although a half-cell with metallic sodium has enough sodium ions to compensate on the negative electrode side, it cannot be utilized in the practical application.

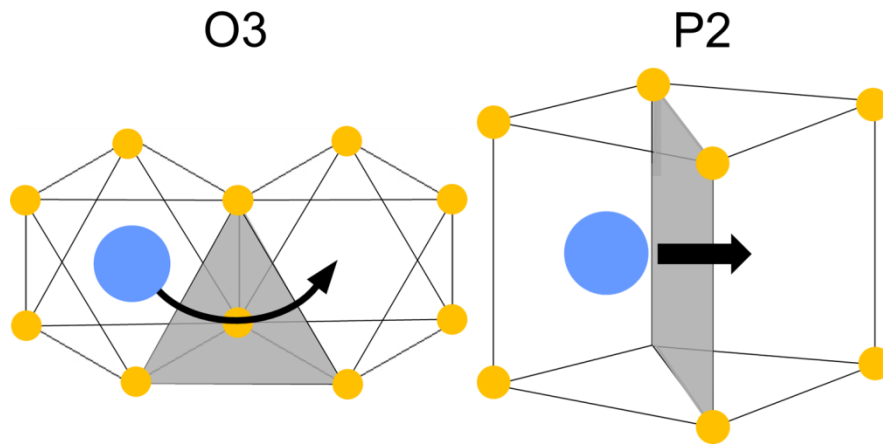


Figure 1.4 Representation of diffusion paths of sodium ions in the different structures with O-type (O2 and O3) and P-type (P2 and P3) stacks. The blue and yellow balls represent the sodium and oxygen atoms, respectively. The shadow parts show the interspace between the two sites.²⁰

Layered P2 and O3 composite is proposed toward a sodium-ion battery with high energy density and long cycle life, which has been reported by our group recently.²⁰ The integration of P2 and O3 structures in this layered oxide is clearly characterized by XRD refinement, SAED and HAADF and ABF-STEM at atomic resolution. The biphasic synergy in this layered P2+O3 composite is well established during the electrochemical reaction. This layered composite can deliver a high reversible capacity with the largest energy density of 640 mAh g^{-1} , and it also presents good capacity retention over 150 times of sodium extraction and insertion.

1.2.2 Polyanion compounds

Polyanion compounds are another attractive positive electrode, providing some advantages in the high potential plateau and open channels. Carbon-coated $\text{Na}_3\text{V}_2(\text{PO}_4)_3$ shows the attractive cycle performance as SIB electrode materials, and the crystal structure is shown in Figure 1.5a.²³ Two distinct plateaus near 1.63 V and 3.40 V are identified, which contribute to the $\text{V}^{2+}/\text{V}^{3+}$ and $\text{V}^{3+}/\text{V}^{4+}$ redox couples, respectively. A reversible capacities of 93 mAh g^{-1} and 59 mAh g^{-1} can be obtained with the voltages ranges of 2.7-3.8 V and 1.0-3.0 V, respectively. Meta-stable olivine NaFePO_4 phase could be synthesized by delithiation and subsequent sodiation of the olivine LiFePO_4 ,²⁴ and the crystal structure is shown in Figure 1.5b. Approximately 0.9 Na ions were seen to be reversibly extracted and inserted with an average voltage near 2.92 V. Maricite NaFePO_4 is reported to show electrochemical activity during Na-ion deintercalation and insertion process.²⁵

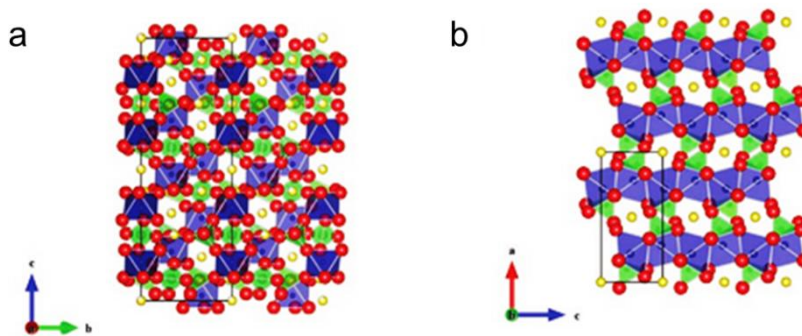


Figure 1.5 Crystal structures of various polyanion compounds: (a) $\text{Na}_3\text{V}_2(\text{PO}_4)_3$, and (b) NaFePO_4 (Na: yellow, V/Fe: blue, O: red).⁵

1.2.3 Other materials as positive electrodes

Some manganese, iron and vanadium oxides have been developed for positive electrode materials. Most of these metal oxides have been demonstrated to reversibly cycle up to more than 1.0 Na-ion, associated with a large capacity.²⁶ However, the complication relative to these metal oxides is that they have no sodium

supply in the intrinsic materials, which stayed at the charged state at the beginning. Very recently, a layered sodium-containing manganese oxide with Birnessite structure is developed by our group for cathode of SIBs.²⁷ This structure has a large layered spacing of 0.72 nm, supplying an open framework for sodium migration. This layered material is electrochemically characterized by galvanostatic charge-discharge test, shown in Figure 1.6. Electrochemical tests suggest that it can deliver a particularly large discharge capacity of 219 mAh g⁻¹ in the voltage rang of 1.5-4.7 V vs. Na/Na⁺. With an average potential of 2.75 V versus sodium metal, it exhibits an energy density of 602 Wh kg⁻¹, much higher than the other reported cathode materials of sodium-ion batteries. Layered NaMn₃O₅ cathode also presents superior rate capability. At a discharge rate of 5C, it delivers a discharge capacity of 115 mAh g⁻¹ after charging at 0.1 C. Furthermore, sodium ions diffusion efficiency of 10⁻¹⁴ cm² s⁻¹ in the layered NaMn₃O₅ electrode is calculated by galvanostatic intermittent titration technique. These results will greatly attribute to the development of room-temperature sodium-ion batteries from the earth-abundant elements.

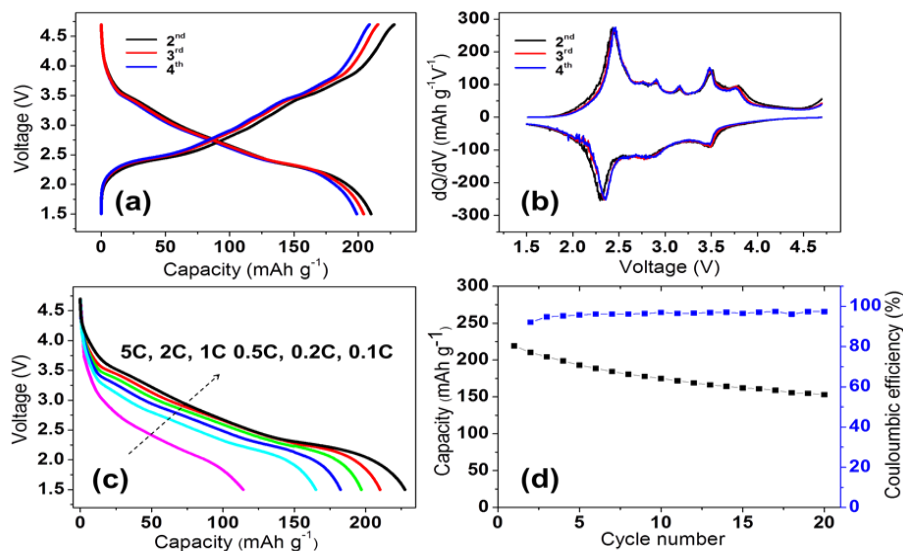


Figure 1.6 (a) The charge-discharge profile of layered NaMn₃O₅ with Birnessite structure; (b) the corresponding dQ/dV plots; (c) Discharge profiles at different rates after charging at 0.1C rate. (d) The cycle profiles of layered NaMn₃O₅ at a charge/discharge rate of 0.1C.²⁷

Prussian blue also can serve as interesting alternative positive electrode materials

for SIBs since its open framework can stand the large lattice volume expansion/contraction induced by the large radius of Na-ion. As a consequence of their low cost and facile synthesis, the hexacyanoferrates (MB=Fe) are the most popular PBAs. Since 2012, Goodenough et al. introduced the $\text{KMFe}(\text{CN})_6$ family ($\text{M}^{\text{II}} = \text{Mn, Fe, Co, Ni, Zn}$) as non-aqueous sodium ion cathodes.²⁸ Recently, this group greatly improved the electrochemical performance of $\text{Na}_2\text{MnFe}(\text{CN})_6 \cdot z\text{H}_2\text{O}$ ($\text{Na}_{2-\delta}\text{MnHFC}$) as a superior cathode by removing the interstitial H_2O .²⁹ The charge-discharge curve and crystal structure with and without interstitial H_2O is indicated in Figure 1.7. This newly discovered dehydrated Hexacyanometallates exhibit a very high average voltage of 3.5 V with a reversible capacity of 150 mAh g^{-1} in a sodium half cell, and after 500 cycles the capacity retention of this material is 75%. The sodium full cell also is assembled with a hard-carbon anode, delivers a capacity of 140 mAh g^{-1} , and it also can be cycled approaching 30 cycles.

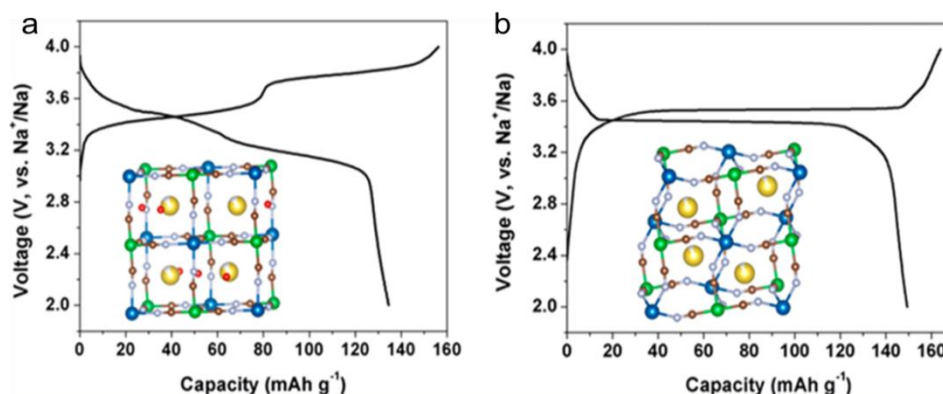


Figure 1.7 (a) The charge-discharge profile of $\text{Na}_{2-\delta}\text{MnHFC}$ with interstitial H_2O , the inset is the corresponding crystal structure. (b) The charge-discharge profile of $\text{Na}_{2-\delta}\text{MnHFC}$ without interstitial H_2O , the inset is the corresponding crystal structure.²⁹

1.3 Anode materials for sodium-ion batteries

1.3.1 Carbon Compounds

Graphite is the most commonly used negative electrode in LIBs, however, cannot be inserted sodium ions to any acceptable extent. Hard carbons synthesized at high temperatures of about $1000 \text{ }^\circ\text{C}$ have been extensively investigated in SIBs. The

discharge-charge profiles of a Na half cell with hard carbon are shown in Figure 1.8.³⁰ An irreversible reduction plateau at around 0.8 V results from decomposition of electrolyte solvent, salts, and additives a passivation layer on the surface of hard carbon. In the subsequent cycles, a large reversible capacity approaching 300 mAh g⁻¹ is achieved in hard carbon materials, especially a reversible capacity of approximately 200 mAh g⁻¹ is observed near 0 V vs. Na/Na⁺. Hard carbon electrodes exhibit good capacity retention during the subsequent cycles with fluoroethylene carbonate (FEC) as an electrolyte additive. However, the voltage plateau of most reversible capacity is at 0.1 V, very close to the sodium plating voltage, which is potentially unsafe in the practical application. Therefore, the discovery of suitable negative electrode materials is a major challenge.

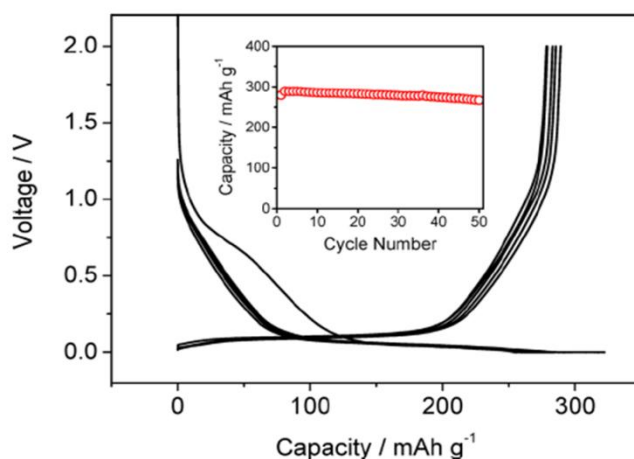


Figure 1.8 Typical discharge-charge profiles of hard-carbon electrodes, and its capacity retention is also shown in the inset.³⁰

1.3.2 Layered titanium-based oxide

Layered sodium titanium-based oxides have attracted much attention because of their suitable potential plateau and high structural stability. Layered lithium-substituted titanium oxide with P2 structure and Na_{0.66}Li_{0.22}Ti_{0.78}O₂ composition is reported by Hu's group, shown in Figure 1.9.³¹ This materials show a reversible capacity of 116 mAh g⁻¹ with an average voltage of 0.75 V. Most

importantly, a good capacity retention of 76% is obtained after long cycle life over 1200 cycles. It is claimed that the zero-strain of volume change is characterized by the in-situ and ex-situ XRD. Otherwise, an unusual quasi-single-phase electrochemical storage behavior is discovered in this P2-type layered material in contrast to most of other P2-type materials.

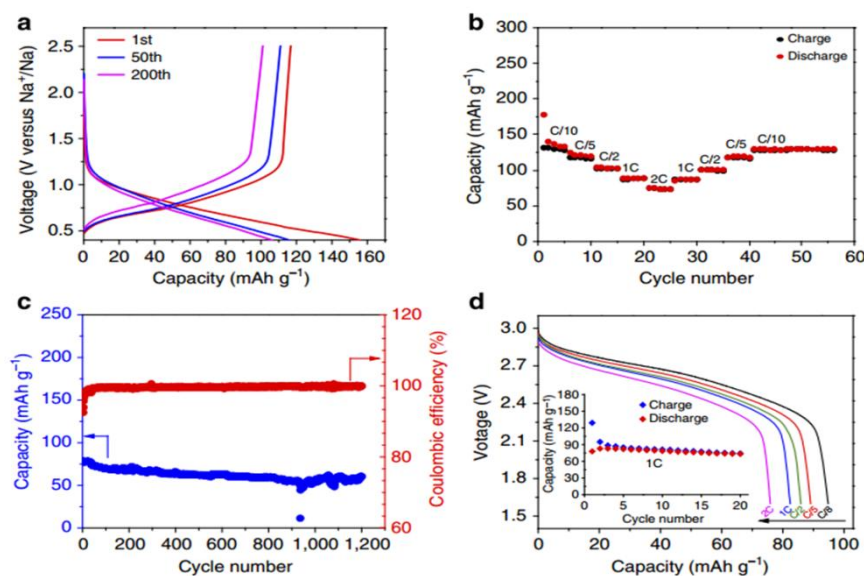


Figure 1.9 (a) The discharge-charge profiles of P2- $\text{Na}_{0.66}\text{Li}_{0.22}\text{Ti}_{0.78}\text{O}_2$ electrodes at a current of C/10 between 0.4 and 2.5 V. (b) Rate capability. (c) The cycling performance and Coulombic efficiency at a rate of 2C. (d) Discharge profiles of $\text{Na}_{0.66}\text{Li}_{0.22}\text{Ti}_{0.78}\text{O}_2/\text{Na}_3\text{V}_2(\text{PO}_4)_3/\text{C}$ sodium-ion full cell at various rates, Inset is the cyclic performance of the full cell at 1C rate.³¹

Up to recently, A $\text{Na}_{2/3}\text{Co}_{1/3}\text{Ti}_{2/3}\text{O}_2$ layered oxide with the P2-type structure (space group P63/mmc) was prepared by a solid-state reaction method by our group.³² Excellent structural stability was observed during the sodium storage process, shown in Figure 1.10. Even after 500 cycles of sodium interstion/extraction processes, the P2-type structure was still preserved, and no new phase appear. This superior stable P2-type structure effectively ensures the electrochemical cycle stability of this material, and after 3000 cycles the capacity retention still amounted to 84.84%. In addition, the good rate performance (40 % of the reversible capacity can be kept even at the 10 C rate) and a reversible capacity of ca. 90 mAh g⁻¹ at a safe average storage voltage of ~ 0.7 V are also attractive to be used in SIBs.

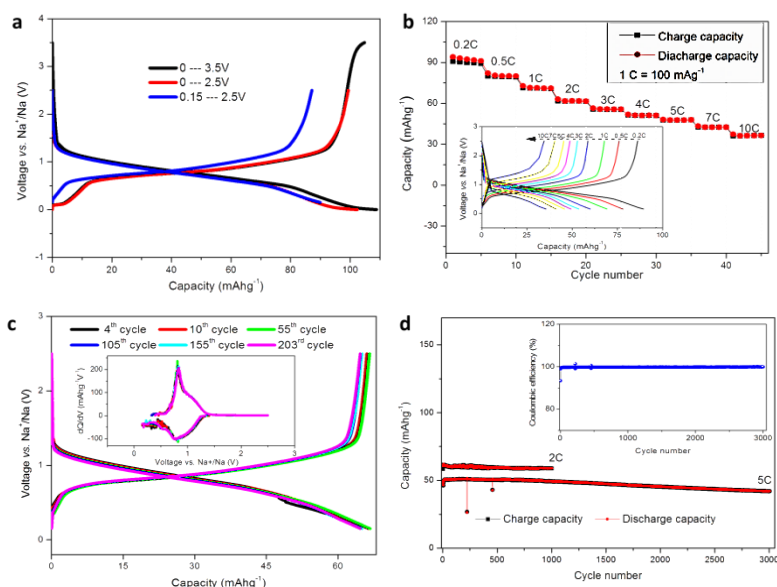


Figure 1.10 (a) The typical discharge-charge profiles of P2- $\text{Na}_{2/3}\text{Co}_{1/3}\text{Ti}_{2/3}\text{O}_2$ electrodes at a current rate of 0.2 C in the different voltage ranges. (b) Rate capability. Insert is the discharge-charge curves at different rates. (c) The discharge-charge curves at different cycles. Insert is the dQ/dV curves variation within 200 cycles. (d) Long-term cycle stability of 1000 cycles and 3000 cycles at rates of 2 C and 5 C, respectively. Insert is the related Coulombic efficiency within 3000 cycles.³²

1.3.3 Other materials as positive electrodes

Some electrode materials have been investigated to be alloyed with Na as potential negative electrodes for rechargeable SIBs, and have the characteristics to react with a larger number of Na, leading to a much higher capacity than hard carbon and titanium-based oxides. With an average voltage of 0.3 V versus Na and a theoretical capacity of 790 mAh g^{-1} , tin is a more promising candidate.³³ Despite a volume expansion of 420%, composite electrodes of tin powder with a polyacrylate binder show a reversible capacity of 500 mAh g^{-1} over 20 cycles at a slow cycling rate. On a positive note, a large reversible capacity of 600 mAh g^{-1} over 160 cycles at a rate of C/10 with an average voltage of 0.8 V versus Na was reported for microcrystalline antimony. The rate capability of this material is excellent, showing a reversible capacity of 500 mAh g^{-1} at a rate of 4C. The insertion of sodium into

amorphous phosphorus achieves a remarkable capacity of 1500 mAh g⁻¹ during first cycles at C/10, with an average potential of 0.6 V versus Na.³⁴ About 1000 mAh g⁻¹ is retained after 80 cycles, and a decrease in the reversible capacity is observed at higher rates. The promising electrochemical properties can be attributed in large part of the high-energy milling of red phosphorus (70%) and super P carbon (30%) that results in an amorphous composite.

1.4 Target and outline of this dissertation

1.4.1 Motivation of this research

To smoothly integrate the renewable energy to the smart grid, a low-cost and long-life energy storage device is extensively necessary for large scale application. The increasing cost and limited availability of lithium suggest that an alternative to lithium-ion batteries should be developed to meet this need for large scale application. Rechargeable sodium-ion batteries (SIBs) have similar chemical storage mechanism with their lithium-ion counterparts, and are expected to be low-cost and chemically sustainable due to almost infinite supply of sodium. Another great advantage is feasible replacement of copper with aluminium current collectors, since the alloying action between sodium and copper doesn't occur, unlike lithium and copper, and it would save substantial cost and weigh for next generation batteries.

Many efforts have been made in search for electrode materials to improve sodium storage performance. As positive electrode materials, layered oxide compounds, polyanion compounds, fuorosulfates/sulfates, prussian blue and others have been extensively investigated. In case of negative electrode materials, carbon compounds layered sodium oxides, transition-metal oxides, alloys and others have attracted much attention. Especially layered sodium oxide Na_xMeO₂ (where Me is 3d transition-metal) of O3, P2 and P3 structures with reversible deintercalation and intercalation aroused researchers' wide concern over recent years. Due to the large Na-ion radius, the extraction and insertion of sodium always induce the obvious volume change even direct phase transition in cathode side. The concern about

anode side is that most of reversible capacity is contributed to the low plateau of 0.1V, potentially leading to the serious safety problems. In the other words, the structural stability and long life in cathode side and safety concerns mainly in anode side are the bottlenecks to the future developments.

Titanium is a good structure stabilizer, which has been evidenced by the superior electrochemical performance of the zero-strain $\text{Li}_4\text{Ti}_5\text{O}_{12}$, and it also can be serve as redox center with a suitable negative potential. In the cathode side, most of these materials present complicated charge-discharge curves and are revealed possessing irreversible structure transition during cycling. The introduction of titanium in transition-metal site can greatly smooth the charge-discharge profile and depress the complex phase transition in the positive materials of $\text{O}3\text{-NaTi}_{0.5}\text{Ni}_{0.5}\text{O}_2$, tunnel $\text{Na}_{0.61}\text{Ti}_{0.48}\text{Mn}_{0.52}\text{O}_2$ and $\text{O}3\text{-NaTi}_{0.6}\text{Ni}_{0.4}\text{O}_2$. The potential safety concerns on carbon materials (especially hard carbon) with possible thermal runaway are noticed because their voltage plateau related with most capacity is too close to the sodium plating voltage in the anode side. If layered titanium oxides directly serve as negative electrode materials by utilizing $\text{Ti}^{4+}/\text{Ti}^{3+}$, the safe potential plateau of 0.7~0.8 V is obtained, greatly improving the potential safety problem in hard carbon. It is well proved by the relative research work about P2 and P3 $\text{Na}_{0.6}\text{Cr}_{0.6}\text{Ti}_{0.4}\text{O}_2$ and $\text{O}3\text{-NaTi}_{0.5}\text{Ni}_{0.5}\text{O}_2$.

In the present research work, we introduce titanium element in the sodium metal oxides mainly with layered structures. These materials with different structures were investigated through Inductively Coupled Plasma (ICP), X-ray diffraction (XRD), scanning electron microscopy (SEM), transmission electron microscopy (TEM) or scanning transmission electron microscopy (STEM), selected area electron diffraction (SAED), Energy Dispersive X-ray Detector (EDX) and Fast Fourier Transform (FFT) measurement. The electrochemical performance is characterized through galvanostatic charge-discharge, cyclic voltammetry (CV) tests. Titanium could play a quite important role, that is: Ti can stabilize the original structure in the cathode side during extraction and insertion process; Ti serves as a redox center in the anode side supplying a stable $\text{Ti}^{4+}/\text{Ti}^{3+}$ redox couples.

1.4.2 Targets of this research

The targets of this study on novel titanium-based oxide electrode materials for SIBs are as follows:

To smooth the charge-discharge profile, associated with the depression of multi-phase transition in the original structure through Ti substitution and improve the electrochemical performance of cathode materials

To investigate the anode performance in layered Ti-containing oxide using $\text{Ti}^{4+}/\text{Ti}^{3+}$ redox couples

To compare the different sodium migration in layered P2 and P3 structure by the combination of experiment and calculation

To comprehensively utilize the dual role of titanium (the structural stabilizer in cathode side and the redox center in anode side) and develop a very interesting titanium-based symmetric sodium cell, showing good cycling performance and rate capability.

1.4.3 Outline of this thesis

There are six chapters in this dissertation.

Chapter 1 is a comprehensive review of sodium-ion battery. It mainly includes a brief introduction about sodium-ion batteries, several important classes of positive and negative electrode materials. The research motivation and targets are also been discussed.

In chapter 2, layered O3-type $\text{NaTi}_{0.5}\text{Ni}_{0.5}\text{O}_2$ with minor impurity has been developed as a new cathode of SIBs. This materials utilize the reversible redox couple of $\text{Ni}^{2+}/\text{Ni}^{4+}$, showing a capacity of about 100 mAh g^{-1} at a 0.2C rate with the voltage range of 2-4 V. The inactive titanium element in this potential window can well stabilize the layered structure, and significantly smooth the charge-discharge profile. Therefore, the good capacity retention of 75% after 300 cycles is observed in the half cell of $\text{NaTi}_{0.5}\text{Ni}_{0.5}\text{O}_2/\text{Na}$, and suitable rate capability could contribute to

the open layered framework.

In chapter 3, titanium-based $\text{Na}_{0.61}\text{Ti}_{0.48}\text{Mn}_{0.52}\text{O}_2$ with tunnel structure is explored for a novel cathode of SIBs. By using $\text{Mn}^{3+}/\text{Mn}^{4+}$ reversible redox couple, the half cell of $\text{Na}_{0.61}\text{Ti}_{0.48}\text{Mn}_{0.52}\text{O}_2/\text{Na}$ can deliver a capacity of 86 mAh g^{-1} . Titanium existence in this tunnel structure greatly smooth the charge-discharge profile and depress the potential phase transition during extraction and insertion process. Owing to the high structural stability, the good capacity retention of 86% after 100 cycles can be achieved in the half cell. The acceptable rate capability is considered to result from the large tunnel framework.

In chapter 4, P-type $\text{Na}_{0.6}\text{Cr}_{0.6}\text{Ti}_{0.4}\text{O}_2$ is introduced for a safe negative electrode for the first time. By adjusting the dissimilar heat temperature, the materials can form two kinds of layered structure: P2 and P3. The sodium ions all occupy the same of prismatic site, but the sodium sites are quite different. The two sites of Na^{I} and Na^{II} and the only one site of Na site will produce the separated sodium migration. Experimentally, P2 shows a more evident plateau of 0.73 V, lower than that of P3, and a reversible capacity of 110 mAh g^{-1} , higher than that of P3 by utilizing the redox couple of $\text{Ti}^{4+}/\text{Ti}^{3+}$. Surprisingly, P2 phase exhibits a much more superior rate capability than that of P3, which evidenced by the large gap of the capability (67 mAh g^{-1} for P2 and 38 mAh g^{-1} for P3 at a 10C rate, respectively). Also P2 phase has much longer cycle of 77.5% capacity retention life after 1000 cycles. First principles calculation is employed to study the detailed sodium diffusion behavior in the two P-type structures. Beyond single vacancy, the migration barrier of Na ions in P2 phase is significantly reduced, corresponding to a facile Na diffusion. Consequently, the P2 phase demonstrates a higher Na-ion mobility relative to the P3 phase, which is perfectly match the experimental data.

Chapter 5 focuses on the construction of a symmetric sodium cell based on titanium-base oxide. O3-type $\text{Na}_{0.8}\text{Ni}_{0.4}\text{Ti}_{0.6}\text{O}_2$ without impurities is investigated not only for cathode materials but also for anode materials. This material contains two electrochemically active transition metals with redox couples of $\text{Ni}^{4+}/\text{Ni}^{2+}$ and $\text{Ti}^{4+}/\text{Ti}^{3+}$ respectively, which has been characterized by charge-discharge test with two

different voltage range of 2-4 V and 0.01-2.5 V. The superiority of good cathode and anode properties could be employed to implement a symmetric sodium cells. This $\text{Na}_{0.8}\text{Ni}_{0.4}\text{Ti}_{0.6}\text{O}_2$ -based symmetric cell exhibits a high voltage of 2.8 V, a reversible discharge capacity of 85 mAh g^{-1} , 75% capacity retention after 150 cycles and good rate capability. This full symmetric cell will greatly contribute to the development of room-temperature sodium-ion batteries towards safety, low cost, long life, and will stimulate further research on symmetric cells using the same active materials as both cathode and anode.

Chapter 6 is the general conclusion and avenues for future work of this research.

Chapter 2 Layered O3-type $\text{NaTi}_{0.5}\text{Ni}_{0.5}\text{O}_2$ as positive electrode materials for sodium-ion batteries

2.1 Introduction

During the past decades, lithium-ion batteries (LIBs) have achieved the remarkable developments for high power density application such as mobile electronic equipment, hybrid electrical vehicles (HEVs) and electrical vehicles (EV).

³⁵⁻³⁷ However, alternative energy storage devices using abundant and environmentally friendly materials are highly desirable in the emerging large-scale energy storage application.³⁶ The limited availability on Li reserves and more concerns about the cost of LIBs are obviously unable to meet this need. Recently, Sodium-ion battery (SIB) shows its superiority in the large-scale energy storage applications due to the high abundance and low cost of sodium.¹⁸

Many cathode materials, such as $\text{Na}_3\text{V}_2(\text{PO}_4)_3$, $\text{Na}_4\text{Fe}(\text{CN})_6$, NaCoO_2 , NaNiO_2 , $\text{Na}_2\text{FePO}_4\text{F}$, $\text{Na}_{0.44}\text{MnO}_2$, and NaMnO_2 for SIBs have been developed recently.^{34, 38-43} Among them, the layered transition-metal oxides (NaMeO_2 , Me = 3d transition metal) have aroused the universal concern because of their reversible extraction/insertion and potential high capacity. However, most of these materials presented complicated charge-discharge curves and underwent irreversible structure transformation during cycling.³⁹ In order to improve the electrochemical performance and structure stability of these electrode materials, solid-solution between NaFeO_2 , NaNiO_2 and NaMnO_2 are studied by Komaba and Delmas et al.⁴⁴⁻⁴⁶ They have investigated the structure and electrochemical performance of O3-type $\text{NaNi}_{0.5}\text{Mn}_{0.5}\text{O}_2$, O3-type $\text{NaFe}_{0.5}\text{Mn}_{0.5}\text{O}_2$ and P2-type $\text{Na}_{0.67}\text{Fe}_{0.5}\text{Mn}_{0.5}\text{O}_2$ electrode materials as cathodes for SIBs in detail.^{45, 46} On the basis of the previous research results, the nickel redox from divalent to tetravalent and iron redox from trivalent to tetravalent can be reversible in a reasonable voltage range while tetravalent manganese remains inactive. More importantly, restricting Mn in the tetravalent state could offer the high structural stability of the relative materials. As a potential analogue to $\text{NaNi}_{0.5}\text{Mn}_{0.5}\text{O}_2$ electrode material, another promising candidate electrode materials $\text{NaNi}_{0.5}\text{Ti}_{0.5}\text{O}_2$ are

designed as cathode materials in sodium-ion batteries.

2.2 Experimental and Characterization

2.2.1 Preparation of O3-NaTi_{0.5}Ni_{0.5}O₂

We prepare this O3-NaTi_{0.5}Ni_{0.5}O₂ material by a simple solid-state method. Proportional amounts of Ni(Ac)₂·4H₂O, TiO₂ and Na₂CO₃ were mixed and ball milled for 24 h for preparing O3-NaTi_{0.5}Ni_{0.5}O₂. The mixture was dried at 100 °C for 12h, pressed into pellets and then calcined at 900 °C for 24 h. The heated pellets were quenched to room temperature and stored in an argon-filled glovebox until use. The pellets were grinded with mortar and pestle in the glovebox to avoid damage by moisture.

2.2.2 Characterization

Powder X-ray diffraction was performed using Cu Ka radiation on a Bruker D8 Advance Diffractometer and the morphology of as-prepared materials was also observed using scanning electron microscopy (SEM, TOPCON DS-720 instrument).

2.2.3 Electrochemical test

The cathode electrodes were prepared by mixing active material, teflonized Acetylene Black (AB) and polytetrafluoroethylene (PTFE) in a weight ratio of 80:15:5. The cathode electrodes were pressed onto the aluminium screen and dried at 110 °C for 5 h. The CR2032 coin-type cells consisting of a cathode and sodium metal anode separated by a glass fiber were assembled in a glove box filled with dried argon gas. The electrolyte was 1 M NaPF₆ in ethylene carbonate/diethyl carbonate (EC/DEC, 1:1 (v/v)). The galvanostatic charge/discharge tests were performed using a Hokuto Denko HJ1001SD8 battery tester at different rates (1C corresponding to 100 mA g⁻¹) at 25 °C after a rest for 12 h.

2.3 Results and Discussion

2.3.1 Structural characterization

The crystal structures of the samples were characterized by XRD (Bruker D8 Advance diffractometer) equipped with a Cu K α radiation and shown in Figure 1 (black lines). It is clear that all Bragg diffraction lines of the sample can be well indexed on the basis of rhombohedral symmetry structure with a space group $R\bar{3}m$ except for the diffraction lines at $2\theta = 37.3^\circ$, 43.3° and 62.9° positions, associating with the impurity of NiO phase (indicated by blue short arrows in Figure 2.1a). We have tried many times for synthesizing the pure rhombohedral symmetry structure of O3- $\text{NaNi}_{0.5}\text{Ti}_{0.5}\text{O}_2$ material by adjusting different synthesis temperatures, methods and raw materials. However, the impurity phase of NiO always occurs.

In order to calculate the lattice parameters of $\text{NaNi}_{0.5}\text{Ti}_{0.5}\text{O}_2$ material, the obtained structure was also refined by the Rietveld method based on O3- NaFeO_2 structure model using the RIETAN-FP program. Owing to the inactive NiO impurity in cathode side, the impurity phase was excluded during refinement process in Figure 2.1b. As indicated in Figure 2.1b, the calculated patterns from the refined model were well consistent with experimental data yielding $R_{\text{wp}} = 7.781\%$, demonstrating that the O3-type structural model (isostructural as O3- NaFeO_2) is the appropriate structural model for $\text{NaNi}_{0.5}\text{Ti}_{0.5}\text{O}_2$. The detailed refined structural parameters are summarized in Table 2.1. As shown in Table 2.1, the lattice structure of $\text{NaNi}_{0.5}\text{Ti}_{0.5}\text{O}_2$ are calculated as $a_{\text{hex}} = 3.0007 (7) \text{ \AA}$ and $c_{\text{hex}} = 16.193 (2) \text{ \AA}$ in a hexagonal setting.

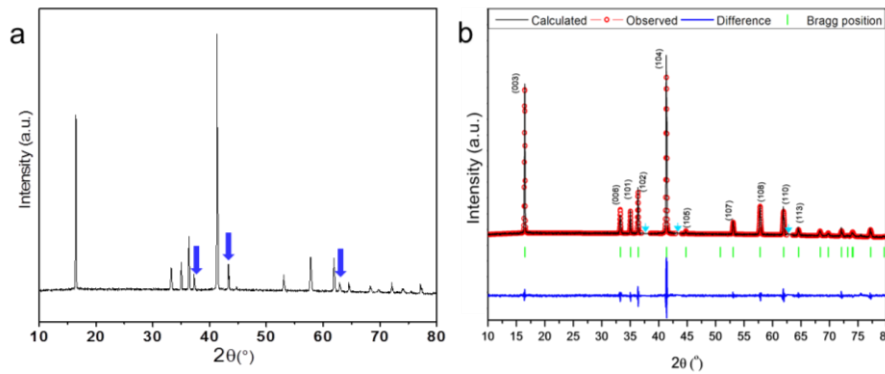


Figure 2.1 (a) XRD pattern of O3- $\text{NaNi}_{0.5}\text{Ti}_{0.5}\text{O}_2$ material with NiO impurity (indicated by blue short arrows). (b) XRD pattern and Rietveld refinement profile excluding NiO impurity: the

observed intensities is shown in red circles; the calculated pattern in a red solid line; the difference in a blue curve; the position of Bragg reflections in green short vertical bars corresponding to rhombohedral $\text{NaTi}_{0.5}\text{Ni}_{0.5}\text{O}_2$ phase; blue arrows indicate the position of NiO phase.

Table 2.1 Lattice parameters of the pristine O3- $\text{NaTi}_{0.5}\text{Ni}_{0.5}\text{O}_2$ sample after Rietveld refinement.

Phase	$\alpha\text{-NaFeO}_2$	
Symmetry	Rhombohedral	
Space Group	R3m	
Cell parameters	a (Å)	3.0007(7)
	b (Å)	3.0007(7)
	c (Å)	16.194(2)
	α (°)	90.000
	β (°)	90.000
	γ (°)	120.000
	Volume (Å ³)	126.27(5)
Agreement factors	R _{wp} (%)	7.781
	R _p (%)	9.376

A schematic illustration of the structure model of O3- $\text{NaTi}_{0.5}\text{Ni}_{0.5}\text{O}_2$ is presented in Figure 2.2. In this model, nickel and titanium ions are accommodated at the octahedral sites of MeO_2 layer (3a sites, Me = Ni and Ti), while sodium ions are located at the octahedral sites of NaO_2 layer (3b sites). Note that there is no cation intermixing between sodium and nickel ions because their large mismatch on ions diameter ($r_{\text{Ni}^{2+}} = 0.69 \text{ \AA}$; $r_{\text{Na}^+} = 1.02 \text{ \AA}$).

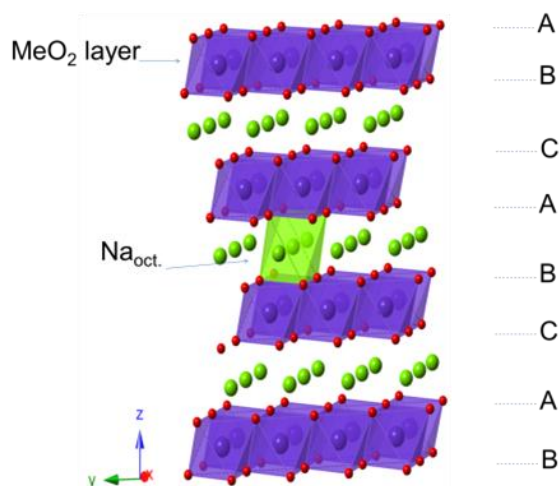


Figure 2.2 Schematic illustration of the crystal structure for O3- $\text{NaTi}_{0.5}\text{Ni}_{0.5}\text{O}_2$ consisting of Me

(metal) octahedron (blue) and Na octahedron (green).

The SEM images of as-prepared O3-NaTi_{0.5}Ni_{0.5}O₂, collected at different magnifications, are shown in Fig. 2.3. The primary particle of the O3-NaTi_{0.5}Ni_{0.5}O₂ show obvious sheet-like morphology and their sizes are ranged from 2 μm to 6 μm.

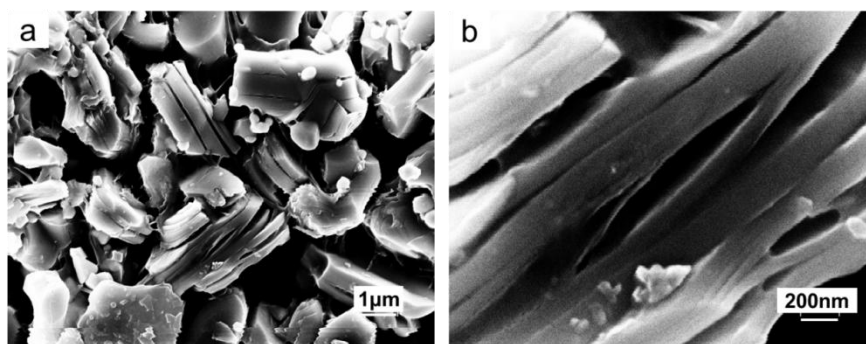


Figure 2.3 SEM images of as-synthesized O3-NaTi_{0.5}Ni_{0.5}O₂ with different magnifications, showing apparent sheet-like morphology.

2.3.2 Electrochemical performance and analysis

Fristly, the electrochemical performance of O3-NaTi_{0.5}Ni_{0.5}O₂/Na cells are tested at a 0.2C rate (1C rate corresponds to 100 mAh g⁻¹) in the voltage window of 2.0-4.7 V. The charge-discharge curves of the first cycle for the O3-NaTi_{0.5}Ni_{0.5}O₂/Na cell are presented in Figure 2.4a. The charge capacity is about 170 mAh g⁻¹, while discharge capacity is about 121 mAh g⁻¹ in the first extraction and insertion process. It is demonstrated that not all of the extracted sodium ions can be inserted back into the interlayers of layered structure, therefore the initial coulombic efficiency is only 70.6% in this voltage range. Accordingly, the initial dQ/dV curve is also shown in Figure 2.3b, and an irreversible oxidation peak above 4.0 V appears without the corresponding reduction peak. The cycle life of O3-NaTi_{0.5}Ni_{0.5}O₂/Na cell after 50 times Na-ion insertion/extraction processes between 4.7 V and 2.0 V is 52.8%, shown in Figure 2.4c. Therefore, the cut-off voltage is optimized to make a reversible electrochemical process.

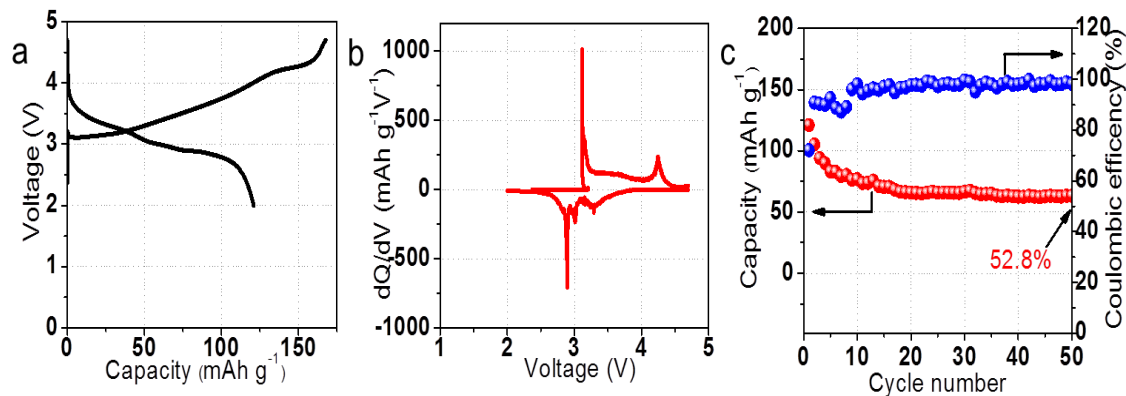


Figure 2.4 (a) Initial charge and discharge curves of the O3-NaNi_{0.5}Ti_{0.5}O₂/Na cell at a rate of 0.2 C (1C corresponds to 100 mA g⁻¹) in the voltage ranges of 2.0-4.7 V versus sodium metal. (b) The corresponding dQ/dV curves. (c) The cycling performance and the corresponding coulombic efficiency over 50 cycles.

When the cut-off voltage of 4.7 V is decreased to 4.0 V, both the initial coulombic efficiency and cycle performance are greatly improved, although the initial discharged capacity is decreased to 102 mAh g⁻¹ from 121 mAh g⁻¹. Figure 2.5 shows the initial three charge-discharge and CV curves of Na/O3-NaNi_{0.5}Ti_{0.5}O₂ half cells. It is evident that the charge-discharge curves of this cell is extremely smooth in Figure 2.5a, indicative of solid solution behaviors. The initial three discharge capacities are the same of 102 mAh g⁻¹ with the average discharge voltage of 3.1 V, and the initial coulombic efficiencies are 87%, 95% and 92%, respectively. More importantly, the initial charge-discharge curves in Figure 2.5a are well overlapped together, indicating the potential of good cycle stability. This is also evidenced by the coincided initial CV curves in Figure 2.5b. Oxidation peaks at ~3.5 V and reduction peaks at ~2.9 V were observed, suggesting reversible sodium ions extraction and insertion. This redox couple in Figure 2.5b is most probably contributed to the redox reaction between divalent, trivalent and tetravalent nickel ions.

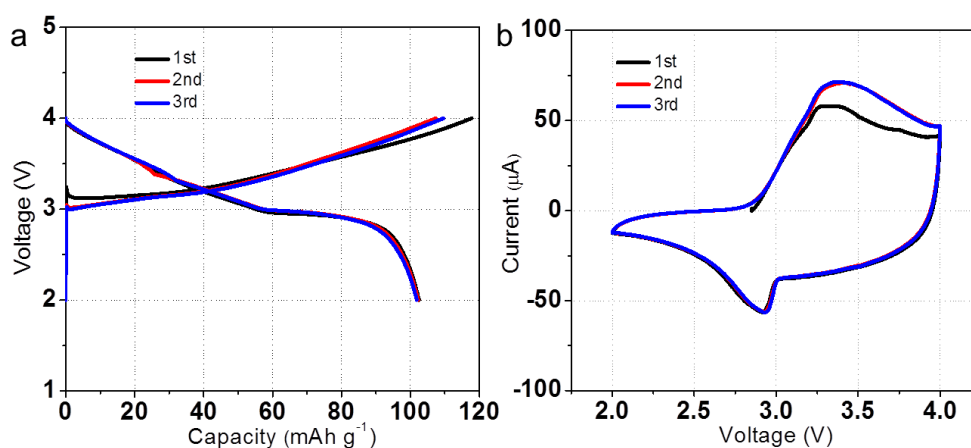


Figure 2.5 (a) The initial charge-discharge profiles at a 0.2 C rate in the voltage ranges of 2.0-4.0 V. (b) The initial CV curves at a scan rate of 0.5 mV s⁻¹.

The cycle stability and rate capability of O3-NaTi_{0.5}Ni_{0.5}O₂ positive materials are shown in Figure 2.6. Figure 2.6a shows the cycling performance and corresponding coulombic efficiency at a 0.2C rate, and the cycle life after 100 times electrochemical sodium ion insertion/extraction processes at a rate of 0.2 C is 93%, and the average coulombic efficiency is close to 96%. With the fast charge-discharge rate of 1C, a good capacity retention of 75% is obtained after after 300 times electrochemical sodium ion, and the average coulombic efficiency during the whole cycles is close to 100%. The good cycle performance of O3-NaTi_{0.5}Ni_{0.5}O₂/Na cells are most attributed to the structure stability of O3-NaTi_{0.5}Ni_{0.5}O₂ electrode material during sodium ions insertion/extraction processes. It should be noted that no any electrolyte optimization in the cell test of the O3-NaTi_{0.5}Ni_{0.5}O₂ materials is carried out, although some researchers reported that some electrolyte additives (such as fluoroethylene carbonate et al.)⁴⁷ can well improve the reversibility of electrochemical sodium ions insertion and extraction processes. Therefore, O3-NaTi_{0.5}Ni_{0.5}O₂ electrode material is expected to be a promising cathode candidate for the good cycling performance in the practical application of SIBs. Rate capabilities of the NaTi_{0.5}Ni_{0.5}O₂/Na cells at different rates of 0.2 C, 0.5 C, 1 C, 2 C, 5 C and 10 C are examined and shown in

Figure 2.6b. The cell delivers large reversible capacity of 90.5 mAh g^{-1} with small polarization even at 1 C rate, which equals to 89% of that at 0.2 C rate. When the charge/discharge rate is 10 C (1000 mA g^{-1}), the discharge capacity of $\text{NaNi}_{0.5}\text{Ti}_{0.5}\text{O}_2$ electrode material can still deliver 27 mAh g^{-1} , which maybe contributed to the faster sodium ions diffusivity in the O3-type phase.

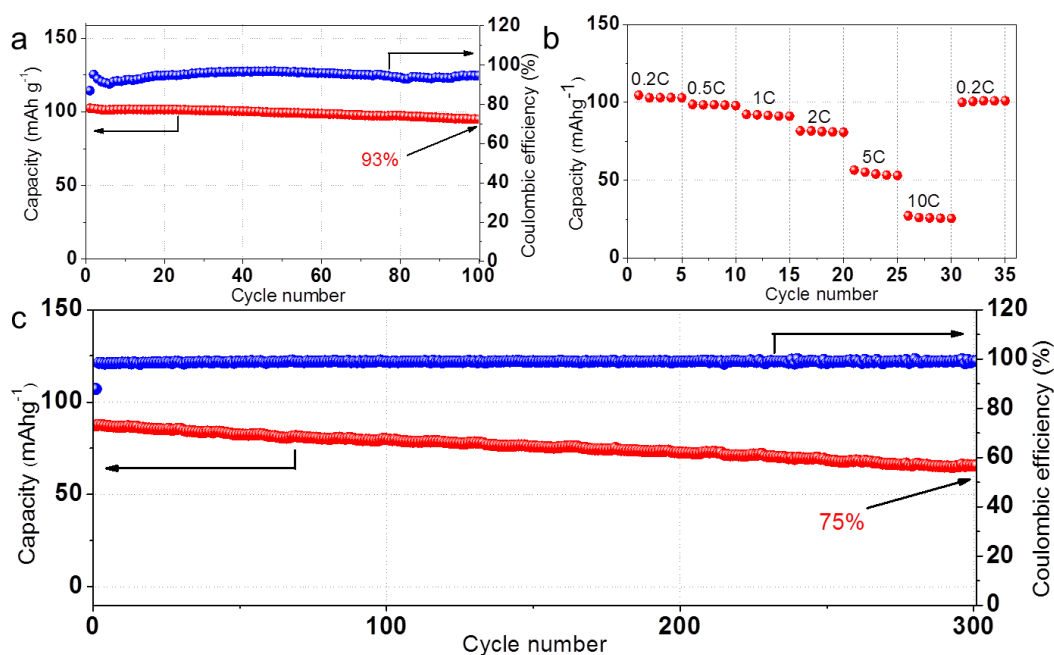


Figure 2.6 (a) Cycling performance and corresponding coulombic efficiency of the O3- $\text{NaNi}_{0.5}\text{Ti}_{0.5}\text{O}_2/\text{Na}$ cells at a 0.2 C rate. (b) Rate performance of the O3- $\text{NaNi}_{0.5}\text{Ti}_{0.5}\text{O}_2/\text{Na}$ cell at different rates of 0.2 C, 0.5 C, 1 C, 2 C, 5 C and 10 C. (c) Cycling performance and corresponding coulombic efficiency of the O3- $\text{NaNi}_{0.5}\text{Ti}_{0.5}\text{O}_2/\text{Na}$ cells at a 1C rate.

2.4 Conclusions

In summary, layered O3-type $\text{NaNi}_{0.5}\text{Ti}_{0.5}\text{O}_2$ is synthesised by a solid-state reaction, and the electrochemical performance of this material as a positive electrode in SIBs are explored for the first time. It exhibits electrochemical activity operating at an average potential of 3.1 V (versus Na^+/Na) and delivers a reversible capacity of about 100 mAh g^{-1} at the current density of 20 mA g^{-1} . In addition, this material shows excellent cycle stability and rate capability. The cycle life after 100 times

electrochemical cycling can be 93.2%, and more than 60 % of discharge capacity can be gotten even at 5 C rate.

Chapter 3 Tunnel $\text{Na}_{0.61}\text{Ti}_{0.48}\text{Mn}_{0.52}\text{O}_2$ as positive electrode materials for sodium-ion batteries

3.1 Introduction

The new energy storage devices are extensively necessary to displace Li-ion batteries (LIBs) when the renewable energy sources is integrated into the electrical power grid. Sodium-ion batteries (SIBs) can offer advantages over its lithium counterpart because the abundance sodium in Earth's crust can significantly reduce the cell cost, and sodium is the second lightest and smallest alkalis element, has the similar physical and chemical properties with lithium. Recently, Sodium-ion batteries have attracted more attentions for renewable energy and the electrical grid in the large-scale energy storage applications,^{5, 48-51} because they could potentially be much less expensive and more environmentally benign.⁵

Many volumes of electrode materials have been studied for SIBs. For the positive electrode materials, polyanionic compounds,⁵² Prussian blue analogues⁵¹ and oxides (especiall layered oxides)^{8, 27, 39, 53-56} are several important materials, which attracted much attention. Among the numerous positive electrode materials, $\text{Na}_{0.44}\text{MnO}_2$ with a tunnel structure is particularly attractive because the unique large tunnel structure is suitable for sodium reversible extraction and insertion.^{57, 58}

Sodium titanium-containing layered oxides are extensively studied since titanium is relatively cheap and nontoxic. O3-type $\text{NaTi}_{0.5}\text{Ni}_{0.5}\text{O}_2$ shows a suitable capacity of about 100 mAh g^{-1} with long service life and superior rate capability, referring to Chapter 2.⁵⁹ In the $\text{Na}_{2/3}\text{Ni}_{1/3}\text{Mn}_{2/3-x}\text{Ti}_x\text{O}_2$ system, titanium-substituted samples demonstrate improved capacity retention, and the optimized composition of $\text{Na}_{2/3}\text{Ni}_{1/3}\text{Mn}_{1/2}\text{Ti}_{1/6}\text{O}_2$ delivers 127 mAh g^{-1} of reversible capacity with 3.7 V average discharge voltage.⁶⁰ Besides, P2-type $\text{Na}_{0.66}\text{Li}_{0.22}\text{Ti}_{0.78}\text{O}_2$ as anode for SIBs especially presents zero-strain character in the cycling process. Its reversible capacity reaches to 120 mAh g^{-1} , as well as performing good capacity retention and rate capability.³¹ It can be concluded that layered materials as electrode for SIBs show

good electrochemical properties especially superior cycle stability. However, few researches about tunnel titanium-containing materials as electrode for SIBs are carried out.

Herein, a tunnel $\text{Na}_{0.61}\text{Ti}_{0.48}\text{Mn}_{0.52}\text{O}_2$ with titanium substitution nearly by half to half, is synthesized by a simple solid-state reaction, and its electrochemical properties as positive electrode of SIBs at room temperature is reported for the first time. The half cell of $\text{Na}_{0.61}\text{Ti}_{0.48}\text{Mn}_{0.52}\text{O}_2$ and sodium metal shows a reversible capacity of 86 mAh g^{-1} with the average voltage of 2.9 V, and it can reach 31 mAh g^{-1} at discharge rate of 5C after charging it by 0.2C rate, associated with good rate capability. After 100 times sodium extraction-insertion processes, capacity retention of 81% is achieved. This material is thus expected to be suitable for a promising cathode of SIBs for large scale application.

3.2 Experimental and Characterization

3.2.1 Preparation of tunnel $\text{Na}_{0.61}\text{Ti}_{0.48}\text{Mn}_{0.52}\text{O}_2$

Tunnel $\text{Na}_{0.61}\text{Ti}_{0.48}\text{Mn}_{0.52}\text{O}_2$ samples were synthesized by a simple solid-state reaction. A proportionable mixture of reagent grade Na_2CO_3 , Mn_2O_3 and TiO_2 was ball-milled under wet conditions with ethyl alcohol additive for 20 h at 200 rpm. The mixtures were dried for 12 h at 100 °C, and the obtained powder was pressed into pellets. Finally, the pellets were heated at 900 °C for 20 h in Ar atmosphere. After calcination, the samples were stored into glove box until use.

3.2.2 Characterization

Powder X-ray diffraction was performed using Cu Ka radiation on a Bruker D8 Advance Diffractometer and the morphology of as-prepared materials was also observed using scanning electron microscopy (SEM, TOPCON DS-720 instrument) and transmission electron microscope (TEM, EM-002B instrument). The half cell charged to a certain voltage was disassembled in a glove box, and the active materials electrode was taken out, cleaned by diethyl carbonate (DEC) and dried at 60 °C for 4

h. The electrodes were then sealed using Mylar film for X-ray diffraction. The ex-situ XRD patterns are also collected on a Bruker D8 Advance Diffractometer.

3.2.3 Electrochemical test

The cathode electrodes were prepared by mixing active material, teflonized Acetylene Black (AB) and polytetrafluoroethylene (PTFE) in a weight ratio of 70:25:5. The cathode electrodes were pressed onto the aluminium screen and dried at 110 °C for 5 h. The CR2032 coin-type cells consisting of a cathode and sodium metal anode separated by a glass fiber sheet were assembled in a glove box filled with dried argon gas. The electrolyte was 1M NaPF₆ in ethylene carbonate/diethyl carbonate (EC/DEC, 1:1 in volume ratio). The galvanostatic charge/discharge tests were performed using a Hokuto Denko HJ1001SD8 battery tester at different rates (1C corresponding to 100 mA g⁻¹) at 25 °C after a rest for 12 h.

3.3 Results and discussion

3.3.1 Structural characterization

The crystallographic structures of tunnel Na_{0.61}Ti_{0.48}Mn_{0.52}O₂ are characterized by powder X-ray diffraction (XRD) method, and the XRD patterns is shown in Figure 1a. It can be seen that all peaks of this material can be well indexed to orthorhombic structure of Na₄Mn₄Ti₅O₁₈ with the space group of Pbam, which are consistent with the values from the standard card (ICSD#01-076-0785), and no impurities are detectable in the XRD patterns. XRD refinement is conducted to give out the accurate structural information. The lattice parameters are refined to be a=9.2629(4), b=26.5631(11) Å, c=2.8915(2) Å and V=711.46(6) Å³ with convergence factors R-factors (5.18%) and χ^2 (1.749) value using GSAS+EXPGUI suite.^{61, 62} The detailed refined parameters are listed in Table 2.1. According to the Inductively Coupled Plasma (ICP) results, the mole ratio of Na:Ti:Mn is 0.38:0.30:0.32, and the chemical composition is confirmed to be Na_{0.61}Ti_{0.48}Mn_{0.52}O₂. The sodium composition is more than 0.44, which is agreeable with A. Manthiram and J.

Akimoto's results.⁶³⁻⁶⁶ Figure 3.1b presents the structure schematic of this materials, isostructural of $\text{Na}_4\text{Mn}_4\text{Ti}_5\text{O}_{18}$. The unit cell is made up of MeO_5 square pyramids and MeO_6 octahedra ($\text{Me} = \text{Ti}, \text{Mn}$), which are arranged to form two types of tunnels: large S-shaped tunnels and smaller pentagon tunnels. There are three Na sites in this structure: the Na site in the small tunnels is fully occupied, while the Na (2) and Na (3) sites in the large S-shaped tunnels are only partially occupied.

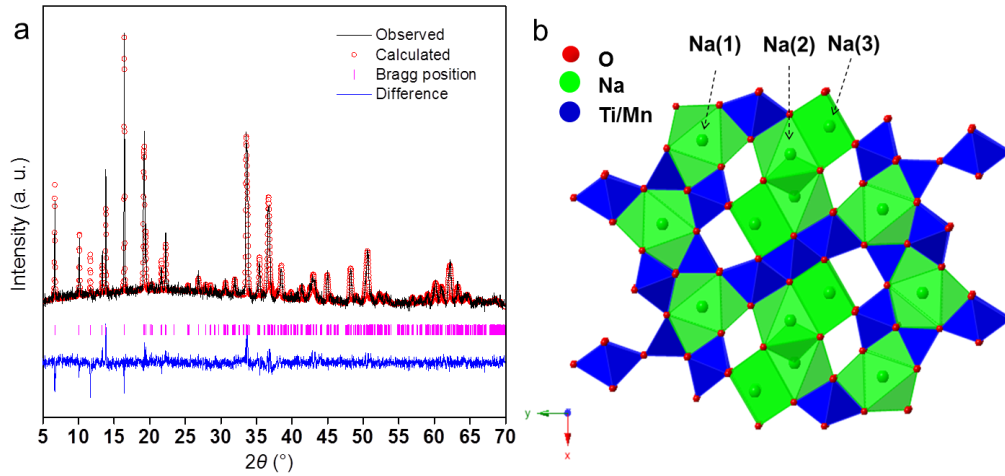


Figure 3.1 (a) XRD pattern of tunnel $\text{Na}_{0.61}\text{Ti}_{0.48}\text{Mn}_{0.52}\text{O}_2$ sample and Rietveld refinement profile. (b) The schematic shows the crystal structure of $\text{Na}_{0.61}\text{Ti}_{0.48}\text{Mn}_{0.52}\text{O}_2$ isostructural with $\text{Na}_4\text{Mn}_4\text{Ti}_5\text{O}_{18}$ consisting of Ti (Mn) octahedron (blue) and Na octahedron (green).

Table 3.1 Lattice parameters of tunnel $\text{Na}_{0.61}\text{Ti}_{0.48}\text{Mn}_{0.52}\text{O}_2$ sample after Rietveld refinement.

Phase	$\text{Na}_4\text{Mn}_4\text{Ti}_5\text{O}_{18}$	
Space Group	Pbam	
Cell parameters	a (Å)	9.2629(4)
	b (Å)	26.5631(11)
	c (Å)	2.8915(2)
	α (°)	90.000
	β (°)	90.000
	γ (°)	90.000
	Volume (Å ³)	711.46(6)
Agreement factors	R_{wp} (%)	5.18
	R_p (%)	3.94
	χ^2	1.749

The morphology of $\text{Na}_{0.61}\text{Ti}_{0.48}\text{Mn}_{0.52}\text{O}_2$ is characterized by scanning electron microscopy (SEM). It is obvious that the material is composed by the secondary

particles of spheres, and the diameter of particles is about 400 nm (Figure 3.2a and b). The detailed crystal structure of the tunnel $\text{Na}_{0.61}\text{Ti}_{0.48}\text{Mn}_{0.52}\text{O}_2$ is further investigated by high resolution transmission electron microscopy (HRTEM). HRTEM characterization suggests the different interlayer spacing of 8.8 nm, 5.4 nm and 6.7 nm respond to (110), (140) and (040) fringes, respectively (Figure 3.2c, d and e), and the Fast Fourier Transform (FFT) corresponding to different fringes is also displayed in the insets. In order to clearly confirm the elements of this material, the energy dispersive spectrometer (EDS) is conducted in the rectangle area of Figure 3.2e. The obvious spectrum peaks further ensure the existence of sodium, titanium, manganese and oxygen elements in the tunnel crystal (Figure 3.2f).

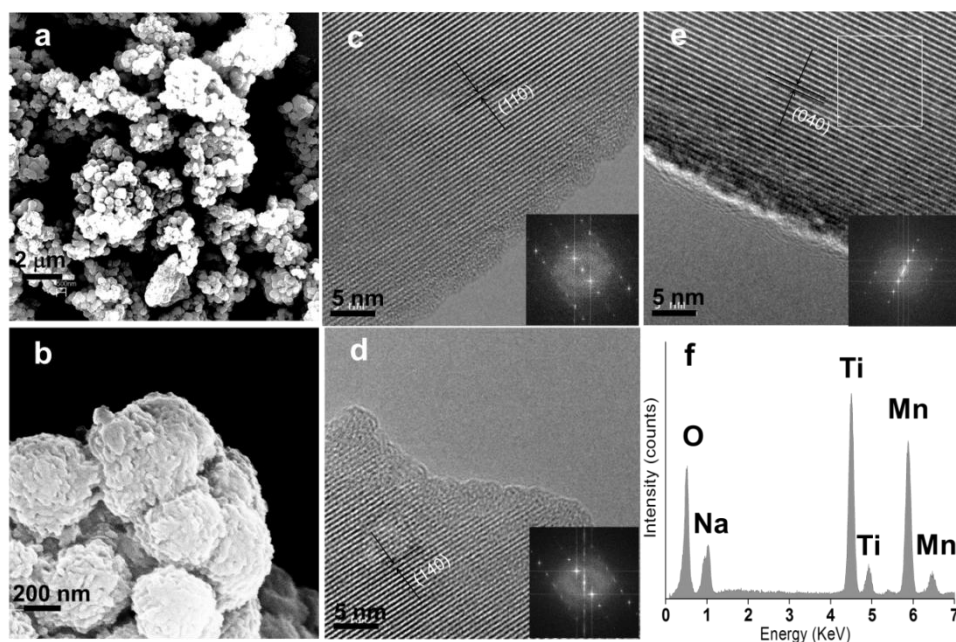


Figure 3.2 (a) and (b) SEM images of tunnel $\text{Na}_{0.61}\text{Ti}_{0.48}\text{Mn}_{0.52}\text{O}_2$ sample with different magnification. (c), (d) and (e) TEM images corresponding to different crystal planes and corresponding FFT (insets); the rectangle area in Figure 3.2e shows the analysis area of EDX maps. (f) The relative EDX analysis results.

3.3.2 Electrochemical performance and analysis

The sodium extraction/insertion behavior is studied by galvanostatic

charge-discharge test with the different cut-off voltages in Figure 3.3. The first galvanostatic charge-discharge profile for $\text{Na}_{0.61}\text{Ti}_{0.48}\text{Mn}_{0.52}\text{O}_2/\text{Na}$ cell at 0.2C rate (20 mA g^{-1}) in the 1.5-4.7 V range is shown in Figure 3.3a. The first discharge capacity can reach 95 mAh g^{-1} . Accordingly, the initial dQ/dV curve is also shown in Figure 3.3b, and two irreversible oxidation peaks above 4.0 V appear without the corresponding reduction peak. The cycle life of the $\text{Na}_{0.61}\text{Ti}_{0.48}\text{Mn}_{0.52}\text{O}_2/\text{Na}$ cell after 30 times Na-ion insertion/extraction processes between 4.7 V and 1.5 V is only 55.8%, shown in Figure 3.3c. Therefore, the cut-off voltage is optimized to get a reversible redox process during cycling process.

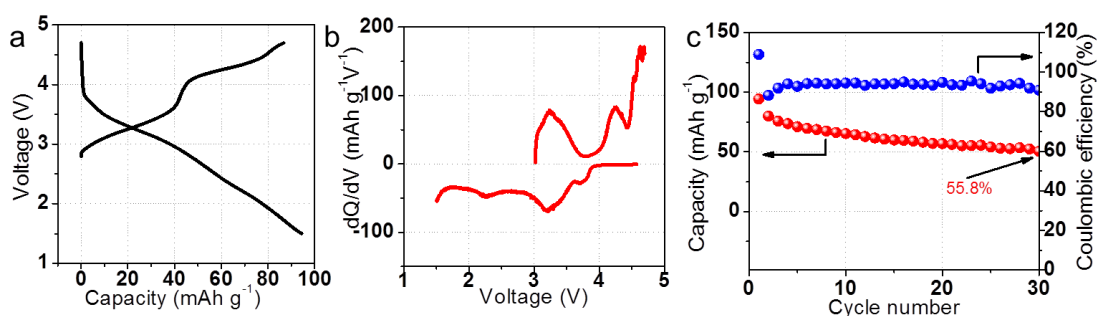


Figure 3.3 (a) First charge-discharge profile at a 0.2C rate in the cut-off voltage of 1.5-4.7 V versus Na^+/Na . (b) The corresponding dQ/dV curve. (c) The cycling performance and corresponding coulombic efficiency.

In order to improve the cycle performance, the half cell of $\text{Na}_{0.61}\text{Ti}_{0.48}\text{Mn}_{0.52}\text{O}_2/\text{Na}$ is tested in the voltage of 1.5-4 V in Figure 3.4a. The first charge/discharge capacity are 46/86 mAh g^{-1} at 0.2C rate, respectively. The following charge/discharge capacities are 88/85 mAh g^{-1} and 86/84 mAh g^{-1} in the 2nd and 3rd cycle, respectively. It is observed that the charge/discharge capacities are nearly equal in the 2nd and 3rd cycle, indicating the high coulombic efficiency and good cycle stability of the tunnel $\text{Na}_{0.61}\text{Ti}_{0.48}\text{Mn}_{0.52}\text{O}_2$. The differential specific capacity plots of the 1st, 2nd and 3rd cycle are shown in Figure 3.4b. Two couples of redox peaks at 3.4/3.3 V and 2.4/2.3 V were observed. The small voltage gap

suggested that this material shows little polarization in the sodium extraction and insertion process. Meanwhile, the overlapped dQ/dV curves reveal a good reversibility in the tunnel $\text{Na}_{0.61}\text{Ti}_{0.48}\text{Mn}_{0.52}\text{O}_2$.

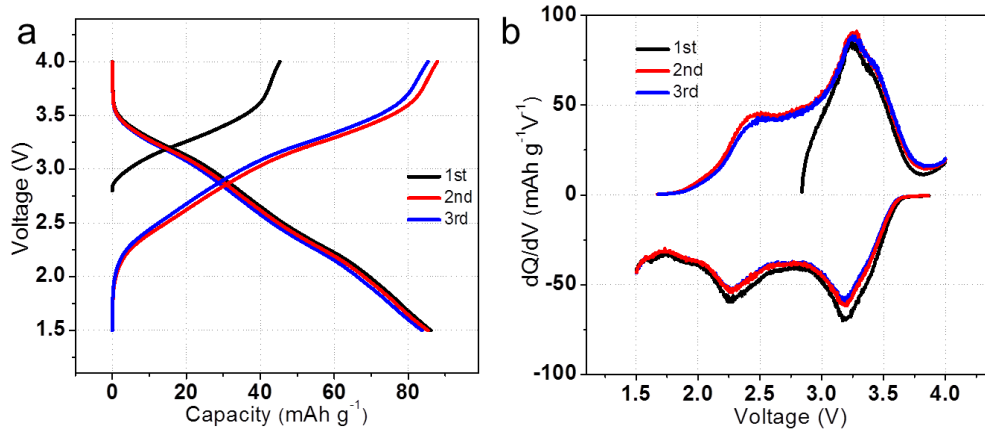


Figure 3.4 (a) Initial charge-discharge profiles at a 0.2C rate in the cut-off voltage of 1.5-4 V. (b) The corresponding dQ/dV curves.

Rate capabilities of the $\text{Na}_{0.61}\text{Ti}_{0.48}\text{Mn}_{0.52}\text{O}_2/\text{Na}$ cells with different discharge rates of 0.2C, 0.5C, 1C, 2C and 5C after charging at 0.2C rate are examined and shown in Figure 3.5a. The cell delivers large reversible capacity of 56 mAh g^{-1} (65% of that at 0.2C rate) with small polarization even at a discharge rate of 1C. When the discharge rate is 5C (500 mA g^{-1}) after charging at 0.2C rate, the discharge capacity of $\text{Na}_{0.61}\text{Ti}_{0.48}\text{Mn}_{0.52}\text{O}_2$ electrode material can still deliver 31 mAh g^{-1} , which maybe contributed to the fast sodium ions diffusivity in the novel tunnel structure. The cycle stability and corresponding coulombic efficiency are also evaluated in Figure 3.5b, and the capacity still maintains 70 mAh g^{-1} after 100 cycles, and the corresponding capacity retention is 81%, and the coulombic efficiency is close to 100% except for the first cycle, showing good cycle stability. The good cycle performance of $\text{Na}_{0.61}\text{Ti}_{0.48}\text{Mn}_{0.52}\text{O}_2/\text{Na}$ cells are most attributed to the structure stability of tunnel $\text{Na}_{0.61}\text{Ti}_{0.48}\text{Mn}_{0.52}\text{O}_2$ electrode material during sodium ions insertion/extraction processes. It is noted that there is no any carbon coating and fining particle treatment before electrochemical testing of the tunnel $\text{Na}_{0.61}\text{Ti}_{0.48}\text{Mn}_{0.52}\text{O}_2$ material,

although some researchers reported that these methods can well improve the capacity and reversibility.⁴⁸ Therefore, tunnel $\text{Na}_{0.61}\text{Ti}_{0.48}\text{Mn}_{0.52}\text{O}_2$ electrode material is expected to be used in practical SIBs for their good reversible structure change after sodium ions extraction/insertion processes.

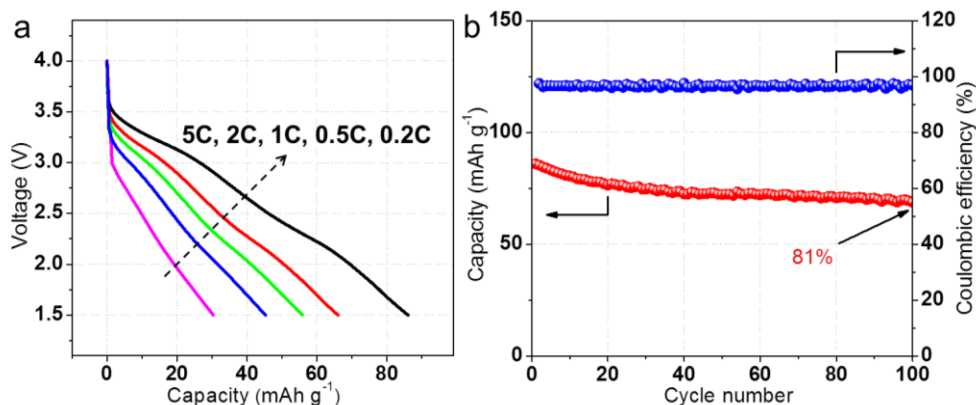


Figure 3.5 (a) Discharge profiles at different rates of 0.2C, 0.5C, 1C, 2C and 5C rate after charging at 0.2C rate. (b) Cycle performance and coulombic efficiency at a 0.2C rate.

In order to analyze the structural evolution during the sodium extraction from the tunnel $\text{Na}_{0.61}\text{Ti}_{0.48}\text{Mn}_{0.52}\text{O}_2$ material, the ex-situ XRD measurements in the different charge stage of the first cycle were carried out in Figure 3.6. The main peaks from the (130) (140) (200) and (160) lattice planes of the pristine tunnel structure are marked with red line. It is obvious that the original structure could stay unchanged before charged to 4.0 V, and new unknown peaks from other phases were detectable in the charge stage of 4.3 V and 4.7 V, which are marked with blue diamond. It is considered that phase transformation occurs when the tunnel materials are charged to the high voltage of 4.3 V or 4.7 V, which could contribute to the bad cycle performance of the half cell with the voltage range of 1.5-4.7 V.

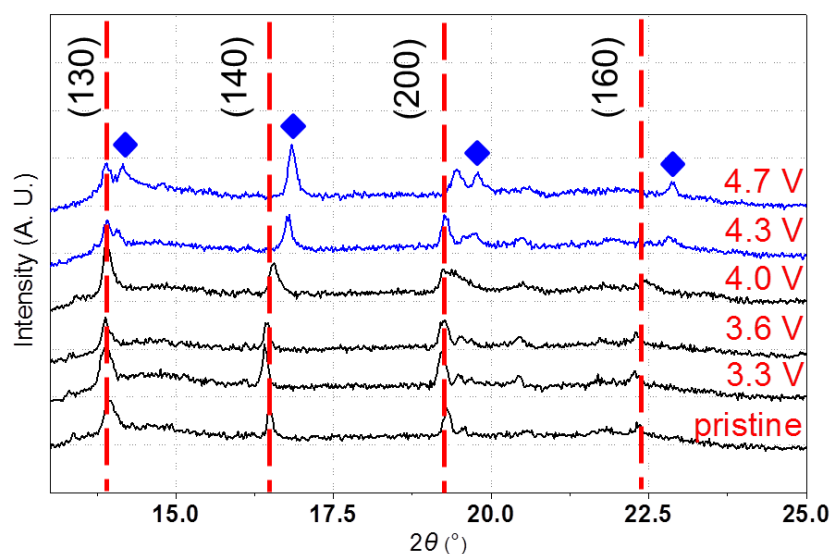


Figure 3.6 Ex-situ XRD patterns for tunnel $\text{Na}_{0.61}\text{Ti}_{0.48}\text{Mn}_{0.52}\text{O}_2$ electrode with the voltage range of 1.5-4.7 V in the initial charge process. The peak position and corresponding lattice plane is marked in the inset. On the right, the corresponding voltages for ex-situ XRD measurement are indicated.

3.4 Conclusions

In the summary, a novel $\text{Na}_{0.61}\text{Ti}_{0.48}\text{Mn}_{0.52}\text{O}_2$ material with tunnel structure is synthesized and its sodium extraction/insertion behavior is investigated in detail for the first time. The tunnel $\text{Na}_{0.61}\text{Ti}_{0.48}\text{Mn}_{0.52}\text{O}_2$ material presents a reversible discharge capacity (86 mAh g^{-1}), good capacity retention (81% for 100 cycles) and a suitable rate capability (31 mAh g^{-1} at a high discharge rate of 5C). Further works on the reaction mechanism and electrochemical performance improvement through carbon coating are in the way.

Chapter 4 Layered P2- $\text{Na}_{0.62}\text{Cr}_{0.63}\text{Ti}_{0.37}\text{O}_2$ and P3- $\text{Na}_{0.62}\text{Cr}_{0.63}\text{Ti}_{0.37}\text{O}_2$ as negative electrode materials for sodium-ion batteries

4.1 Introduction

To smoothly integrate the renewable energy to the smart grid, an inexpensive and efficient energy storage device is urgently necessary for large scale application.² The increasing cost and limited availability of lithium suggest that an alternative to lithium-ion batteries should be developed to meet this need for large scale energy storage.^{5, 6, 13} Rechargeable sodium-ion batteries (SIBs) have similar chemical storage mechanism with their lithium-ion counterparts, and are expected to be low-cost and chemically sustainable due to almost infinite supply of sodium. Meanwhile, the feasible replacement of Cu with Al current collectors (no alloying reaction between Na and Al) will further save substantial cost and weigh for next generation batteries.

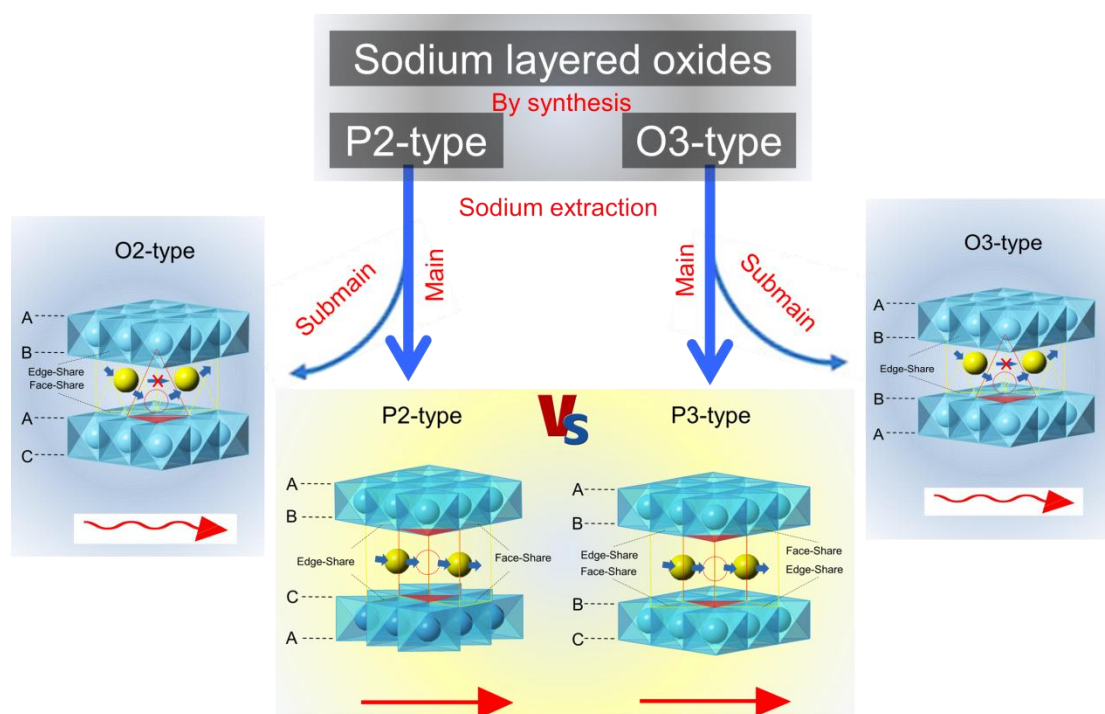


Figure 4.1 Classification of layered sodium oxides (Na_xMeO_2), electrochemical phase-transition induced by sodium extraction and Na ions migration paths in different layered structures. Note that P2-phase more easily maintain its original structure, while O3-phase always transforms to P3-phase during sodiation process. The yellow and blue balls

represent the sodium and transition-metal atoms, respectively. The red circles and shadow parts indicate the intermediate site during sodium diffusion and the interspace between the two sites, respectively. The red lines below show the direct Na migration for P2- and P3-phases, and the indirect migration for O2- and O3-phases.

Owing to large specific capacity and reversible insertion/extraction, layered sodium oxide Na_xMeO_2 (Me = 3d transition metal) has been the hot study on sodium-ion batteries for decades. Layered Na_xMeO_2 polytypes obtained by chemical solid-state synthesis mainly show two different structures of P2 and O3 (**Figure 4.1**),¹⁹ and some of them have been extensively studied for electrode materials of SIBs. Owing to the direct Na-ion diffusion and more open framework, the original structure of P2 phases is more easily persevered during the sodium extraction process,^{21, 67, 68} although partial P2-O2 phase transition is found in the literature.^{69, 70} In contrast, O3 phases always transform to P3 phases achieved by the gliding of MeO_2 slabs (1/3, 2/3, 0) due to the intermediate tetrahedral sites between two octahedral sites (**Figure 4.1**).^{71 12} As two main electrochemical products, P2 and P3 phases have the same sodium accommodation of prismatic sites. So far, the connection and distinction between two layered structures of P2 and P3 has been rarely established. As shown in the bottom of **Fig. 1**, the local of environment of Na ions at prismatic sites and diffusion pathway in the P2 and P3 phases are different, which immediately determine their respective electrochemical kinetics. No research on the Na-ion conduction of P3 phase as electrode materials has been done until now, partly because P3 phase easily resulted from electrochemistry is directly synthesized by solid-state reaction on rare occasion.^{46, 72} Another point is that the phase transition and relative electrochemical properties are very dependent on the sodium content,^{56, 73} so a couple of P2 and P3 phases with nearly the same composition are quite essential to generalize this study. Some fundamental issues still need to be clarified up to now. For instance, which is better choice of P2 and P3 phases for high-performance electrode materials between? How can we understand their structure-properties relationship more clearly?

In this work, we present layered $\text{P2-Na}_{0.62}\text{Cr}_{0.63}\text{Ti}_{0.37}\text{O}_2$ and

P3- $\text{Na}_{0.63}\text{Cr}_{0.63}\text{Ti}_{0.37}\text{O}_2$ with nearly the same composition and high structural stability, enabling the systematic study of crystal-structure and electrochemical-property relationship. Electrochemical tests manifest that P2 phase shows more evident plateau of 0.73 V, lower than that of P3 phase, and a reversible capacity of 110 mAh g^{-1} , higher than that of P3. With a high rate of 10C, P2 phase still delivers a large capacity of 66 mAh g^{-1} , which is 56% of that at 0.2C rate. After 1000 cycles at 5C rate, the capacity retention is 77.5%. These superior rate capability and cycling performances far surpass those of P3 phase and even other sodium negative electrode materials.^{18, 74-76} P2- $\text{Na}_{0.62}\text{Ti}_{0.37}\text{Cr}_{0.63}\text{O}_2$ with an acceptable discharge capacity, a safe potential, outstanding rate capability and cycling performance is a promising candidate for long-life and high-rate sodium-ion batteries.

The crystal structures and their sodium storage mechanism related with titanium valence change in layered P2 and P3 structures are firstly confirmed by atomic-scale characterizations based on the spherical aberration-corrected electron microscopy. Most important, the first-principles calculation combined with galvanostatic intermittent titration technique (GITT) is well utilized to identify the smoother Na diffusion in P2 phase compared with that of P3. P2 phase shows a lower sodium diffusion barrier than that of P3 in the case of sodium multi-vacancy, and it is essentially revealed that Na diffusion kinetics is determined by the structural difference (P2 vs. P3) and independent of transition metal ions. It will expand a deeper understanding of the crystal structure-electrochemical performance relationship, and also provide new avenues for designing advanced electrode materials of sodium-ion batteries.

4.2 Experimental and Characterization

4.2.1 Material preparation.

P2- and P3-NTCO samples are synthesized by traditional solid-state reaction. All solid chemical compounds were purchased from Wako Pure Chemicals Industries Ltd.. The raw materials of Na_2CO_3 , Cr_2O_3 and TiO_2 (anatase form) with

stoichiometric proportion are well ground in an agate mortar at a rotate rate of 200 r/min for 20 h. Owing to the sodium volatility in high temperature, an excess 5 wt.% of Na_2CO_3 is added. The mixture is dried for 12 h at 100 °C. The obtained powders were pressed into pellets, and then the pellets were conducted with heat treatment in the Ar flow. P3-NTCO is synthesized under the heat treatment temperature of 900 °C and duration time of 20 h. P2-NTCO can be obtained when heat temperature and heat duration is set to 1000 °C and 20 h, respectively. P2 and P3 mixed composite can be also obtained at 950 °C and 20 h. The heated pellets were quenched to room temperature and stored in an argon-filled glove box until use. The molar ratios of metal ions in the layered P2 and P3 samples was chemically analyzed by Inductively Coupled Plasma Mass Spectrometry (ICP-MS) and the Na/Ti/Cr ratios were determined to be 0.62:0.37:0.62 and 0.63:0.37:0.63, respectively, well matching our designed materials.

4.2.2 Characterizations.

The XRD measurement were performed using Cu Ka radiation on a Bruker D8 Advance Diffractometer. A JEOL-2100F STEM equipped with a double aberration-corrector for both probe-forming and imaging lenses is used to perform HAADF and ABF imaging, which was operated at 200 KV. The convergence angle was 25 mrad and the angular range of collected electrons for HAADF imaging is about 60-250 mrad.

4.2.3 Electrochemistry.

The electrochemical tests were carried out using the CR2032 coin-type cells, consisting of a cathode and sodium metal anode. The cathode electrodes were prepared with a weight ratio of 75% of active material, 20% of teflonized acetylene black, and 5% of polytetrafluoroethylene. Pellets for half cells were pressed in the form of aluminium screens approximately 3 mg in mass and 7 mm in diameter (the loading mass is around 1.95 mg cm^{-2}), then dried under vacuum at about 110 °C for 5 h before cells assembly. The cells were assembled in a glove box filled with dried argon gas. The electrolyte was $1 \text{ mol dm}^{-3} \text{ NaClO}_4$ dissolved in propylene carbonate

(Tomiya Pure Chemical Industries) with 2 vol% fluorinated ethylene carbonate as an electrolyte additive. The double layers of a glass fiber (connected with cathode electrode) and a Celgard 2400 (connected with sodium metal anode) serve as the separator of sodium half cells. The layered P2 and P3 compounds/Na half cells were cycled in the voltage range of 0.15–2.5 V for anode performance. 1C corresponds to 100 mA g⁻¹ in the cell tests.

The chemical diffusion coefficient of Na⁺ (D_{Na^+}) is calculated according to Eq. (1) and its simplified form Eq. (2) derived by Weppner and Huggins as follows:^{77, 78}

$$(1) D_{Na^+} = \frac{4}{\pi} \left(\frac{m_B V_M}{M_B S} \right)^2 \left(\frac{E_s}{(dE_\tau/d\sqrt{\tau})} \right)^2 (\tau \ll L^2) \quad (2) D_{Na^+} = \frac{4}{\pi} \left(\frac{m_B V_M}{M_B S} \right)^2 \left(\frac{E_s}{\Delta E_\tau} \right)^2$$

Where V_M is the molar volume of the compound, and M_B and m_B are the molecular weight and the mass of the active materials, respectively. S is the interface area between the active material and electrolyte. L is radius of the active particle.

4.2.4 First-principles calculation.

Spin-polarized calculations were performed using the Vienna Ab initio Simulation Package (VASP)^{79, 80} within the projector augmented-wave approach.⁸¹ Generalized gradient approximation (GGA) in the parameterization of Perdew, Burke, and Ernzerhof (PBE)⁸² pseudopotential was used to describe the exchange–correlation potential. Minimum energy pathways and saddle points of Na⁺ migration were calculated with the nudged elastic band (NEB) method.⁸³ This approach duplicates a series of images between the starting point and the end point of diffusing ion to simulate the intermediate states, with the positions of the starting point and the end point fixed. The supercell comprises 3 × 3 × 1 conventional unit cells, corresponding to 18 and 27 formula units for P2 and P3 phases, respectively. For the large supercell adopted in NEB calculations, only the Γ point is adopted for k-point sampling to reduce the computational cost. The plane-wave cutoff was set to 520 eV. Geometry optimizations were performed by using a conjugate gradient minimization until all the forces acting on ions were less than 0.01 eV/Å per atom.

4.3 Results and discussion

4.3.1 Structural characterization

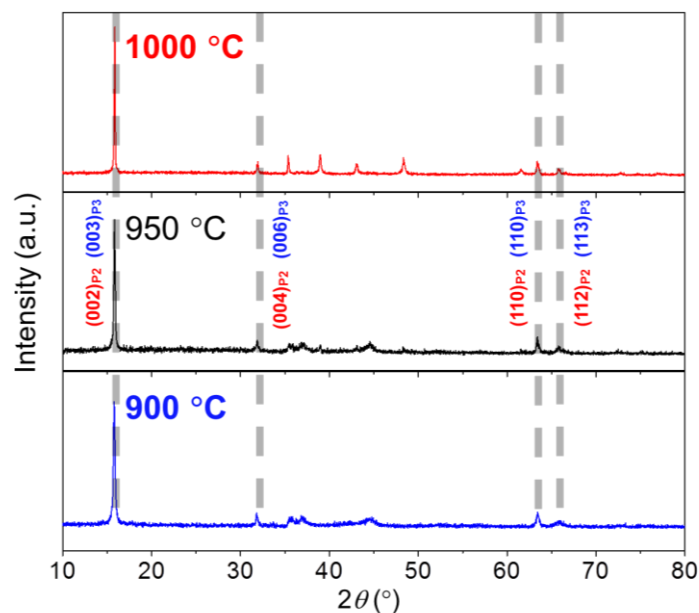


Figure 4.2 XRD patterns of $\text{Na}_{0.6}\text{Ti}_{0.4}\text{Cr}_{0.6}\text{O}_2$ materials at different heat temperatures, and the dotted lines indicate an overlapping of the $(00l)$ reflections for both layered P-type phases.

The crystal structures of samples annealed at different temperatures (900, 950, and 1000 °C) for 20 h were recorded by X-ray diffraction (XRD) in **Figure 4.2**. These materials show the different crystal structures: P3 structure synthesized at 900 °C, P2 structure at 1000 °C and the mixture of P2 and P3 at 950 °C. An overlapping of the $(00l)$ reflections can be observed for these layered P-type phases in **Figure 4.2**. It has been demonstrated that P3-P2 phase transition could be achieved under high-temperature condition rather than electrochemical reaction because of the large energy to break/reform Me-O bonds for this transformation.¹² The P2 and P3 phases display almost the same composition ($\text{P2-Na}_{0.62}\text{Ti}_{0.37}\text{Cr}_{0.63}\text{O}_2$ and $\text{P3-Na}_{0.62}\text{Ti}_{0.37}\text{Cr}_{0.63}\text{O}_2$, hereafter denoted as P2-NTCO and P3-NTCO), respectively. Note that the simultaneous synthesis of layered P2 and P3 phases with same

stoichiometry is the key to make a fair comparison, which is quite rare to the best of our knowledge.

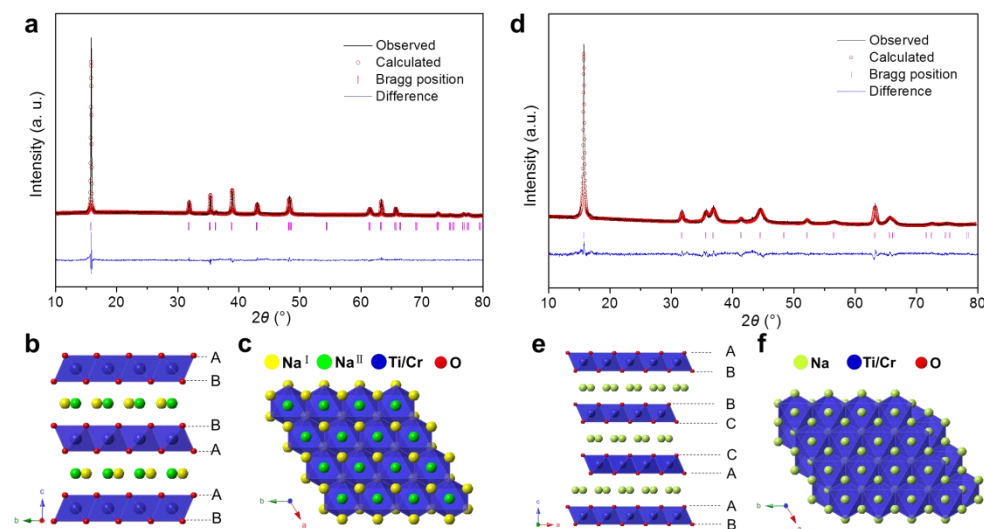


Figure 4.3 Structure of P-type NTCO materials. (a) XRD and Rietveld plots of P2-NTCO compounds with experimental data in black dots, calculated curves in red and difference curve in blue, and standard Bragg reflections in pink short vertical bars. (b) P2-type crystal structure viewed along a-axis showing the two different Na ions sites by green and yellow colors. (c) P2-type crystal structure viewed along c-axis showing that every Na^I (edge-sharing) site is surrounded by the three Na^{II} (face-sharing) site, while every Na^{II} site is surrounded by the three Na^I sites. (d) XRD and Rietveld plots for refined P3-NTCO with experimental data in black dots, calculated curves in red and difference curve in blue, and standard Bragg reflections in pink short vertical bars. (e) P3-type crystal structure viewed along a-axis showing the only one Na ions site by green-yellow color. (f) P3-type crystal structure viewed along c-axis showing that every Na site is edge-sharing in one side, and face-sharing in the other side. Note that part of sodium prisms are open to show short distances between sodium sites which cannot be occupied simultaneously.

Figure 4.3a shows Rietveld plots of P2-NTCO, and all the diffraction lines can be well indexed to a hexagonal lattice with space group P63/mmc. The lattice parameters are refined to be $a=b=2.9410(1)$ Å, $c=11.2639(3)$ Å and $V=84.375(4)$ Å³ with convergence factor R_{wp} -factors (9.55%) and χ^2 (2.210) value using GSAS+EXPGUI suite^{61, 62} (Detailed crystallographic data on refined P2-NTCO are

listed in **Tables 4.1**). The crystal structures of P2-NTCO are displayed in **Figure 4.3** (**b** and **c**), which is characterized by the ABBA oxygen stacking including two MeO_6 octahedra per unit cell (**Figure 4.3b**), and offer two different sites for Na cations either sharing faces with two MeO_6 octahedra of adjacent slabs or sharing edges with six MeO_6 octahedra (**Figure 4.3c**). XRD and Rietveld plots of P3-NTCO is shown in **Figure 4.3d**, and it indicates that all the diffraction lines can be assigned to the P3-type structure with space group $R\bar{3}m$. Rietveld refinement of XRD pattern successfully gave out reasonably low R_{wp} -factors (8.75%) and χ^2 (1.623) value based on P3 models. P3 phase was fitted for lattice parameters of $a=b=2.9466(2)$ Å, $c=16.8758(11)$ Å and $V=127.652(19)$ Å³. The calculated XRD patterns of P3 are in good agreement with the experimental data, and the detailed refinement results are also shown in **Table 4.1**. **Figure 4.3e** and **f** also show the crystal structure of P3-NTCO with ABBCCA oxygen stacking and three MeO_2 sheets per unit cell (**Figure 4.3e**) have prisms sharing one face with one MeO_6 octahedron and three edges with MeO_6 octahedra of the next layer, resulting in only one sodium site (**Figure 4.3f**).

Table 4.1 Lattice parameters of P2 and P3-type $\text{Na}_{0.6}\text{Ti}_{0.4}\text{Cr}_{0.6}\text{O}_2$ samples after Rietveld refinement.

Phase	P2-type $\text{Na}_{0.6}\text{Ti}_{0.4}\text{Cr}_{0.6}\text{O}_2$		P3-type $\text{Na}_{0.6}\text{Ti}_{0.4}\text{Cr}_{0.6}\text{O}_2$	
Space Group	P63/mmc		$R\bar{3}m$	
Cell parameters	a (Å)	2.9410(1)	a (Å)	2.9433(2)
	b (Å)	2.9410(1)	b (Å)	2.9433(2)
	c (Å)	11.2639(3)	c (Å)	16.9517(9)
	α (°)	90.000	α (°)	90.000
	β (°)	90.000	β (°)	90.000
	γ (°)	120.000	γ (°)	120.000
	Volume (Å ³)	84.375(4)	Volume (Å ³)	127.180(15)
Agreement factors	R_{wp} (%)	9.55	R_{wp} (%)	8.69
	R_p (%)	7.47	R_p (%)	6.75
	χ^2	2.210	χ^2	2.305

To further determine atomic crystal structures of P2- and P3-NTCO materials, advanced spherical aberration-corrected electron microscopy experiments were performed at atomic scale in **Figure 4.4**. **Figure 4.4 (a and b)** indicates the experimental and simulated SAED patterns of P2 phase, respectively. The bright spots of P2 phase projected along [010] direction in **Figure 4.4a** corresponds a typical diffraction pattern for P2-structure lattice, which perfectly matches the simulated stacking sequences along b-axis crystallographic direction in **Figure 4.4b**. The local structure of P2-NTCO materials were analyzed with atomic resolution by high-angle annular dark field (HAADF) and annular bright field (ABF)-STEM. The bright-dot contrast in HAADF-STEM images (**Figure 4.4c**) and the dark-dot contrast in ABF-STEM images (**Figure 4.4d**) reveal the transition-metal (Ti and Cr) atom column positions. The corresponding FFT in **Figure 4.4c** is consistent with the SAED pattern. The relative weak dark-dot localized between interlayers in ABF-STEM images (**Figure 4.4d**) corresponds to the sodium and oxygen atom columns. **Figure 4.4 (e and f)** indicates the experimental and simulated SAED patterns of P3 phase. The bright spots projected along [010] direction in **Figure 4.4e** can be assigned to characteristic reflections originating from P3-structure lattices, consistent with the simulated results in **Fig. 3F**. HAADF and ABF-STEM images are also shown in **Figure 4.4 (g and h)**. The corresponding FFT is inserted in **Figure 4.4g**.

To directly compare the crystal structure of P2- and P3-NTCO, their enlarge ABF- and HAADF-STEM images are shown in **Figure 4.4 (i, j, k and l)**. As shown in **Figure 4.4j**, the enlarged HAADF-STEM image from **Figure 4.4d** shows the detailed atomic arrangements and exhibits stacking sequences of ABBA, characterizing the layered P2-phase. The atomic model of layered P2-phase is inserted for convenient visualization. ABF-STEM observation of octahedral MeO_2 ($\text{Me} = \text{Ti}$ and Cr) are highly consistent with the structural model, as highlighted by blue shade (**Figure 4.4j**). The alkali metal atoms are clamped by MeO_2 layers. Specially, every two layers of MeO_2 are structurally mirror symmetric. The enlarged ABF-STEM image in **Figure 4.4l** extracted from **Figure 4.4g** exhibits the detailed atomic arrangements with regard to stacking sequence of ABBCCA of layered P3 phase, and the atomic

model of layered P3 structures is also inserted for easy comparison.

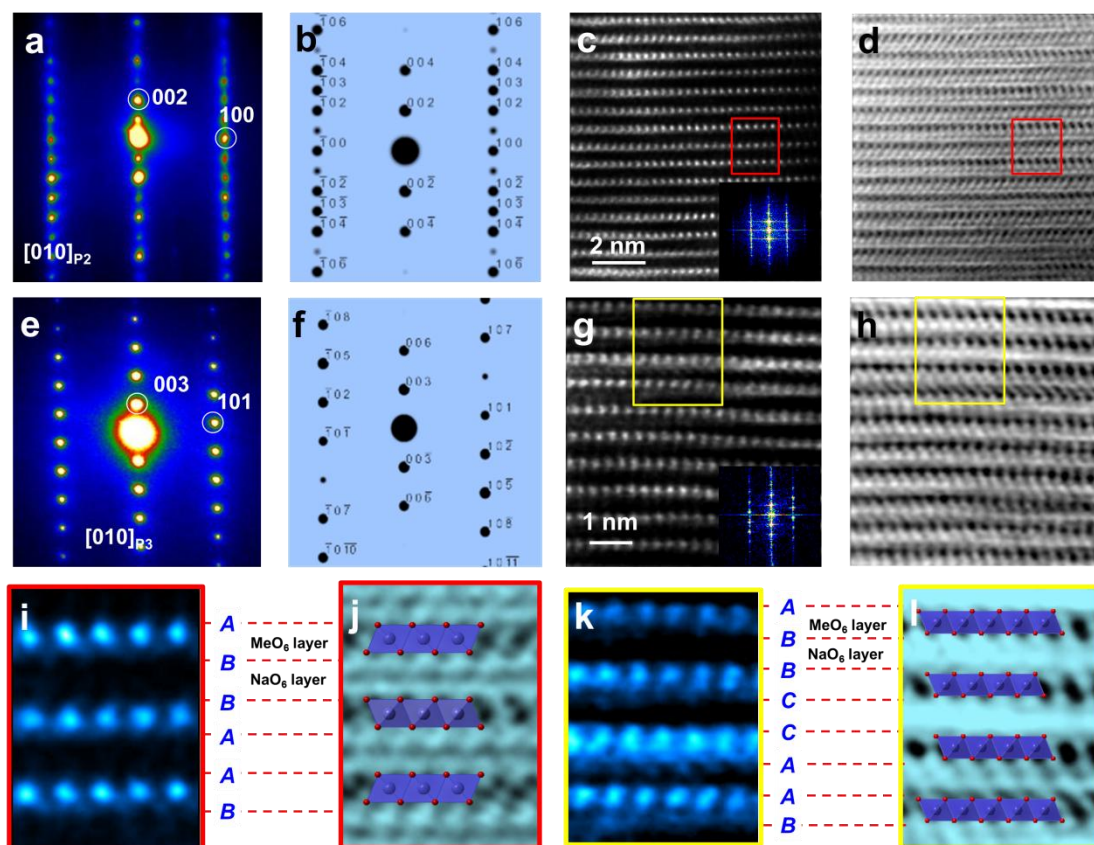


Figure 4.4 STEM imaging of P-type NTCO materials. (a) experimental SAED patterns of P2-NTCO viewed along [010] zone axis. (b) simulated SAED patterns of P2-NTCO viewed along [010] direction. (c) HADDF-STEM image of P2-NTCO. (d) ABF-STEM image of P2-NTCO. (e) experimental SAED patterns of P3-NTCO viewed along [010] zone axis. (f) simulated SAED patterns of P3-NTCO viewed along [010] direction. (g) HADDF-STEM image of P3-NTCO. (h) ABF-STEM image of P2-NTCO. (i) and (j) enlarged ABF-STEM image extracted from (C) and (D), showing the ABBAAB stacking of P2. (k) and (l) enlarged ABF-STEM image extracted from (G) and (H), showing the ABBAAB stacking of P2.

4.3.2 Electrochemical performance and analysis

Electrochemical properties of P2- and P3-NTCO negative electrode materials are characterized by galvanostatic discharge-charge test in the half cells with the voltage range of 0.15-2.5 V at a 0.25C rate vs. Na^+/Na , shown in **Figure 4.5**.

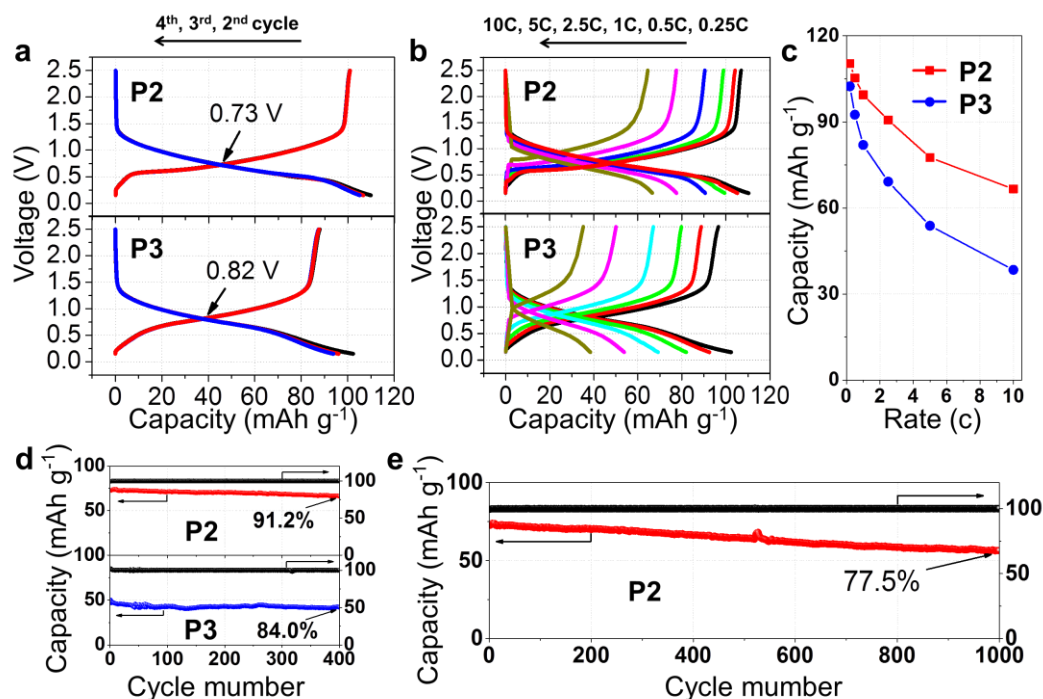


Fig. 4.5 The electrochemical performance of P2- and P3-NTCO compounds. (a) The typical charge-discharge profiles between 0.15 and 2.5 V region at a 0.2C rate (1C rate corresponding to 100 mA g⁻¹). (b) The rate capability at different rates of 0.2C, 0.5C, 1C, 2C, 5C, and 10C. (c) The plots of reversible capacity versus C rates. (d) The cycling performance with Coulombic efficiency of 400 cycles at a 5C rate. (e) The cycling performance with Coulombic efficiency of 1000 cycles only for P2-NTCO at a 5C rate.

A reversible discharge capacity of 110 mAh g⁻¹ was obtained for P2-NTCO in the subsequent cycles at a discharge-charge rate of 0.25 C, and 102 mAh g⁻¹ for P3-NTCO (**Figure 4.5a**). The average potentials are also marked in **Figure 4.5a**, and 0.73 V is obtained for P2-NTCO, which is lower than that of P3-NTCO (0.82 V). The typical dQ/dV curves of P2 and P3 phases were compared in **Figure 4.6** (c and d), and a couple of sharper redox peaks are associated with the evident plateau-like features in the discharge-charge curves of P2, while P3 phase shows a slope-like features in dQ/dV curves. It indicates that full cells using P2-NTCO as anode will provide the higher average voltage, larger energy density and better plateau characteristic than those of P3 assemble full cells in the case of the same cathode. The discharge-charge profiles of P2- and P3-NTCO in Na half cells with different rates of

0.25C, 0.5C, 1C, 2.5C, 5C and 10C are examined and shown in **Figure 4.5b**, and their comparison plots is shown in **Figure 4.5c**. At the same C rate, all the layered P2 phase show higher discharge capacity than that of P3 phase. For instance, the layered P2- and P3-NTCO phases deliver a discharge capacity of 99 mAh g⁻¹ and 82 mAh g⁻¹ at a 1C rate, respectively. The discharge capacity gap between P2- and P3-NTCo is more remarkable with the rate increase, the discharge capacities are 78 mAh g⁻¹ for P2-NTCO, 54 mAh g⁻¹ for P3-NTCO at 5C rate, and 67 mAh g⁻¹ for P2-NTCO and 38 mAh g⁻¹ for P3-NTCO at a 10C rate, respectively.

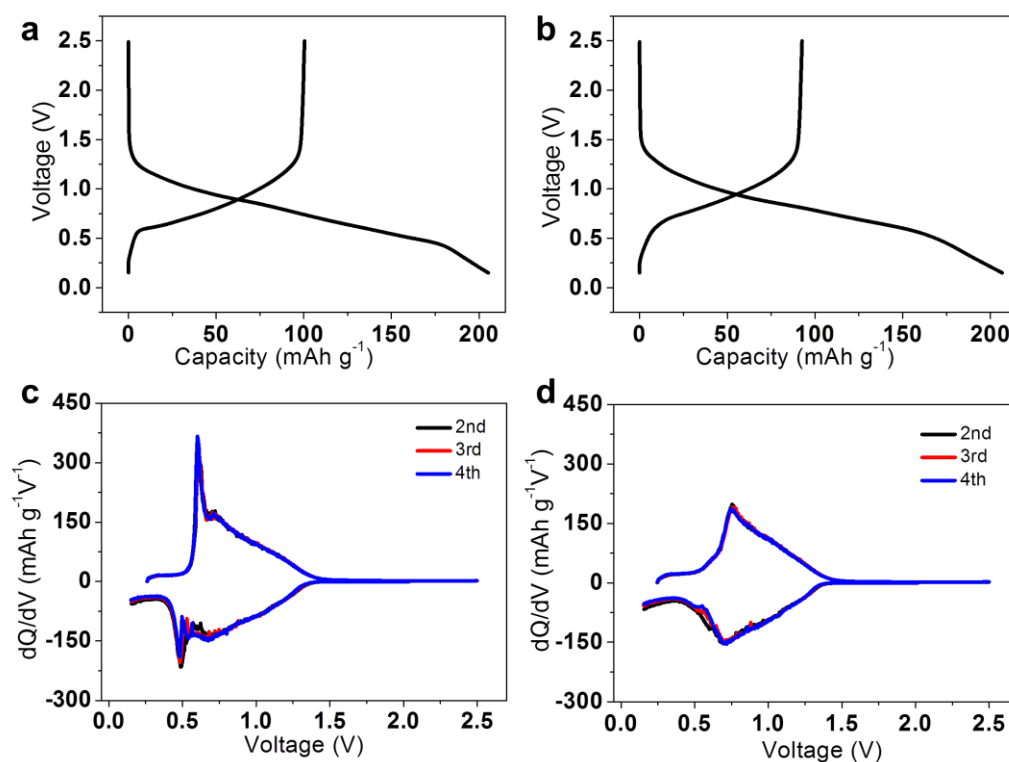


Figure 4.6 (a) The first discharge-charge profile of P2-NTCO. (b) The first discharge-charge profile of P3-NTCO. (c) The typical dQ/dV curves of P2-NTCO. (d) The typical dQ/dV curves of P3-NTCO.

The cycle stability and the coulombic efficiency are evaluated at a 5C rate in **Figure 4.5d**. The capacity of P2-NTCO after 400 cycles with a 5C rate still maintains 66 mAh g⁻¹, and the corresponding capacity retention is 91.2%, and the average coulombic efficiency is close to 100% showing good electrochemical

reversibility. However, the capacity retention of P3-NTCO after 400 cycles with a 5C rate is only 84.0%. Long-term cycling performance is further studied for P2-NTCO at higher rate of 5C (**Figure 4.5e**). Capacity retention of 77.5% were measured even after 1000 cycles, and the capacity decay rates only amounted to approximately 0.0225% per cycle. The good cycle performance of P2-NTCO is most attributed to the faster sodium migration and better structure stability of layered $\text{Na}_{0.62}\text{Ti}_{0.37}\text{Cr}_{0.63}\text{O}_2$ electrode material during sodium ions insertion/extraction processes than those of P3. Therefore, the appealing electrochemical performance of P2-NTCO, which features excellent long-term cycle stability and Coulombic efficiency, can prompt the use of SIBs for large-scale energy-storage devices.

4.3.3 Sodium storage mechanism

To further understand the structural and valence evolution of P2- and P3-NTCO during Na insertion, the ex-situ XRD and EELS experiments are performed. **Figure 4.7** shows the ex-situ XRD patterns of P2-NTCO and P3-NTCO, well matching the standard reflection of P2 and P3 structures respectively, and there is no evident appearance of always occurred P2-O2 or P3-O3 phase transition upon Na insertion. The well maintained P-type framework during electrochemical process will well contribute to the following Na-ion diffusion study.

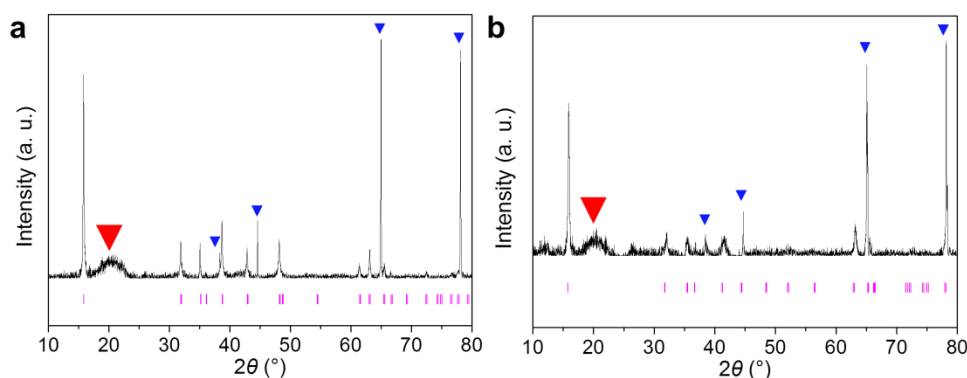


Figure 4.7 (a) The ex-situ XRD of fully sodiated (discharge to 0.15 V) P2-NTCO. The standard Bragg reflections of P2 phase are shown in pink short vertical bars. (b) The ex-situ XRD of fully sodiated (discharge 0.15 V) P3-NTCO. The standard Bragg reflections of P3 phase are

shown in pink short vertical bars. The red inverted triangles indicate the broaden reflections resulted from the sealed Kapton film of ex-situ XRD test, and the blue inverted triangles correspond to the reflections resulted from Al substrate.

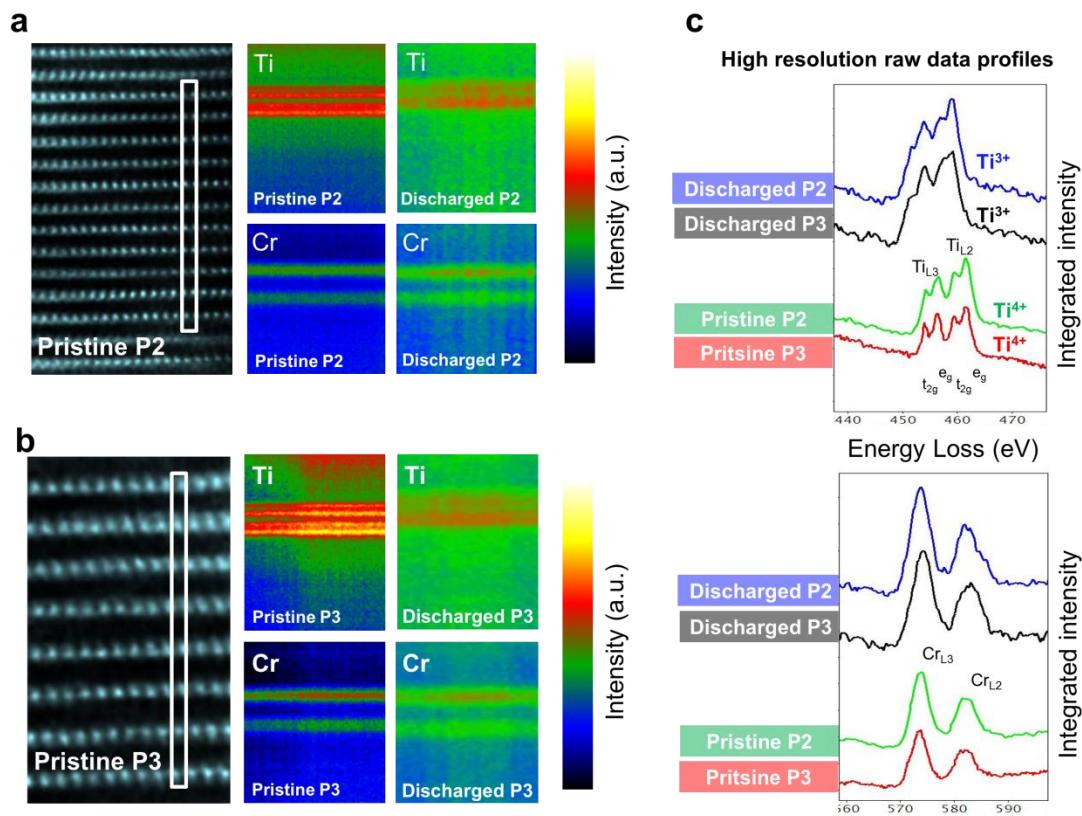


Figure 4.8 The EELS analysis showing the remarkable valence change of titanium in P2- and P3-NTCO compounds. (a) EELS mapping of the pristine P2-NTCO, and the white rectangle of STEM image indicates the analysis area. Atomic resolution STEM-EELS line scanning of Ti and Cr along the c-axis before and after discharge is observed in the colourful images. (b) EELS mapping of the pristine P3-NTCO, and the white rectangle of STEM image indicates the analysis area. Atomic resolution STEM-EELS line scanning of Ti and Cr along the c-axis before and after discharge is observed in the colourful images. (c) the high-resolution EELS profiles of P2- and P3-NTCO compounds.

Figure 4.8 shows atomic resolution STEM-EELS line scanning was performed vertical throughout the c-axis, providing an energy resolution of 0.5 eV. Ti $L_{2,3}$ and Cr $L_{2,3}$ edges were acquired simultaneously and a suitable energy dispersion of 0.3 eV per pixel was selected. In this way, the pristine and discharged P2- and P3-NTCO

particles (**Figure 4.8a** and **b**) were investigated respectively. **Figure 4.8c** shows the high-resolution EELS profiles, in order to quantitatively understand the elemental information and valence state of the NTCO system. Remarkably, in process of discharging P2 and P3 samples, the critical excitation energy for Ti-L₃ shift to 459.1 eV from the original 461.4 eV, while Ti-L₂ shift to 453.9 eV from 456.2 eV. For the ELNES of Ti L_{2,3}, the major difference in the electron structure of the pristine and discharged Ti element (in P2 or P3 phases) is the degree of occupancy of the t_{2g} level. Ti³⁺ has one t_{2g} electron and Ti⁴⁺ has none, which is very noticeably reflected in the position of the fine Ti L_{2,3} edges. Thus the shift of Ti L_{2,3} could be assigned to the formation of Ti³⁺ during discharging process. However, the peak position and energy shift exhibit seldom change regarding the Cr L_{2,3} edges, as well as the ratio of integrated L3 and L2 peaks, verifying the invariant Cr³⁺ during charge-discharge process. From a conventional atomic physical point of view, transition metal atoms (Ti/Cr) combined with electronegative atoms (oxygen) or trapped inside an electronegative environment always exhibit a shift in energy, in addition it means that there is slight over-oxidation of the Ti/Cr atoms. For this negative electrode, only the Ti L_{2,3} edge changes significantly, corresponding to the Ti⁴⁺ – Ti³⁺ reduction during Na insertion.

4.3.4 First principles calculation

The phase stability of both P2 and P3 phases during electrochemical measurements, as evidenced by above XRD results, allows us to assess the difference of Na-ion transport between P2 and P3 phases employing density functional theory (DFT) based first-principles calculations. The EELS data have shown that only Ti redox works during the charge/discharge process, while Cr ions are electrochemically inactive. Accordingly, the P2-Na_{0.62}Ti_{0.37}Cr_{0.63}O₂ and P3-Na_{0.63}Ti_{0.37}Cr_{0.63}O₂ used in our work can be considered as Cr-doped Na_{0.6}TiO₂. For convenience, we firstly study the P2- and P3-Na_xTiO₂. As mentioned earlier, there are two crystallographically distinguishable trigonal prismatic Na sites in P2-Na_xTiO₂, denoted by Na^I and Na^{II}

sites (**Figure 4.3b** and c). The $\text{Na}^{\text{I}}\text{O}_6$ prism is face-sharing with TiO_6 octahedra, while

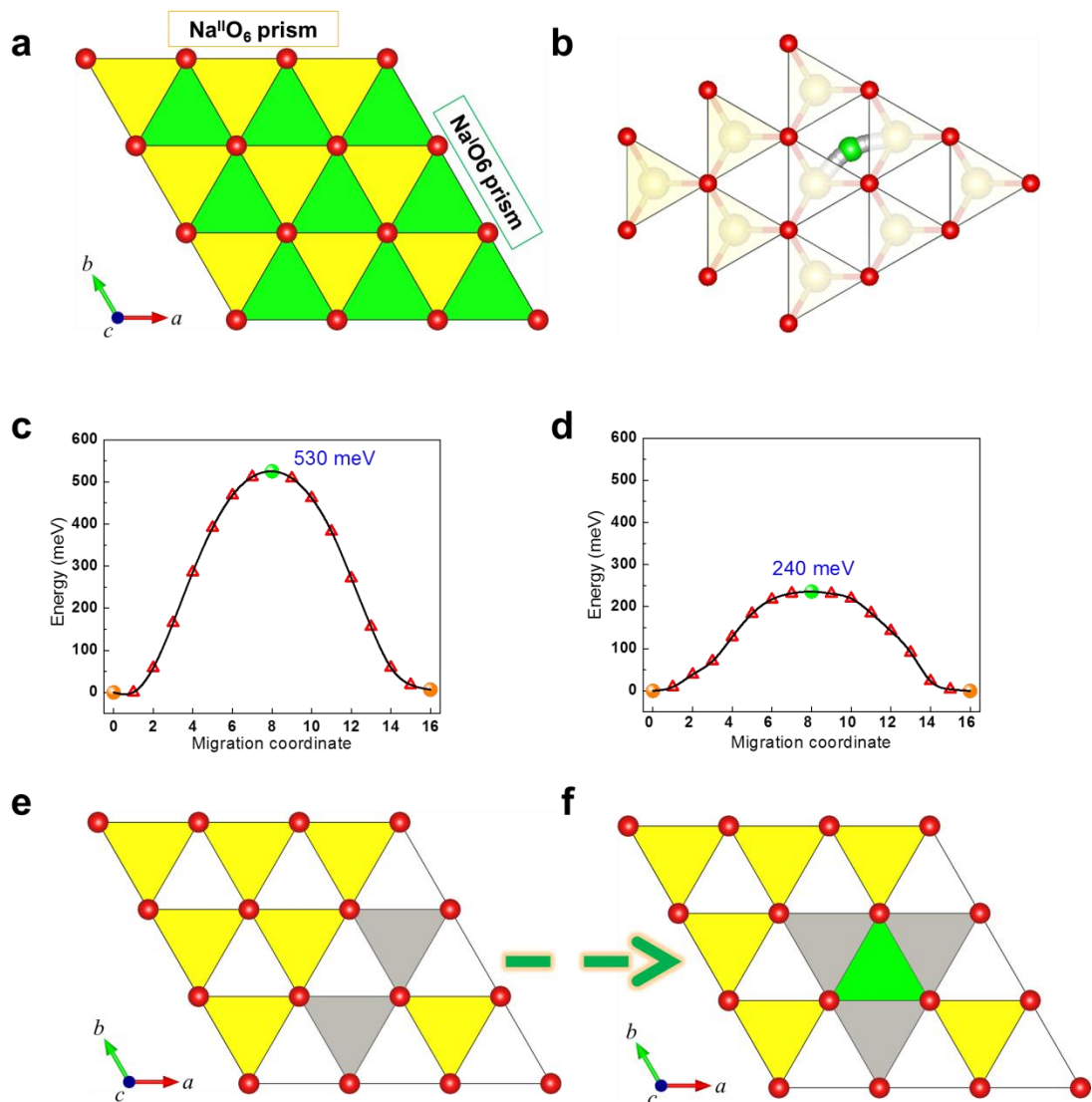


Figure 4.9 (a) 2D view of the Na layer for both P2 and P3 phases. The $\text{Na}^{\text{I}}\text{O}_6$ and $\text{Na}^{\text{II}}\text{O}_6$ prisms are represented by green and yellow colors, respectively. (b) the schematic of sodium diffusion path under single vacancy approximation. (c) the calculated energy barriers and trajectories of Na-ion diffusion under single vacancy approximation of P2 structure. (d) the calculated energy barriers and trajectories of Na-ion diffusion under single vacancy approximation of P3 structure. (e) Na layer configurations with two adjacent Na^{II} site vacancies before relaxation. (f) Na layer configurations with two adjacent Na^{II} site vacancies after relaxation, showing that all Na ions are “fixed” in the case of divacancy.

the $\text{Na}^{\text{II}}\text{O}_6$ prism is edge-sharing with TiO_6 octahedra. By contrast, all Na sites in P3 phase are crystallographically equivalent, edge-sharing with TiO_6 octahedra at one

side and face-sharing with TiO_6 octahedron at another side (**Figure 4.3e** and **f**). Here we divide the Na sites of P3 phase into Na^{I} and Na^{II} , analogous to the P2 phase. It should be noted that this is an artificial classification, for convenient comparison between P2 and P3 phases in the following calculations. Computational results show that for stoichiometric P2- NaTiO_2 , all Na ions occupy the Na^{II} sites, as the edge-sharing environment is more energetically favorable (246 meV/f.u.) relative to the face-sharing environment. For stoichiometric P3- NaTiO_2 , the ground state is that either Na^{I} or Na^{II} sites are fully occupied by Na ions, as P3- $\text{Na}^{\text{I}}\text{TiO}_2$ and P3- $\text{Na}^{\text{II}}\text{TiO}_2$ are equivalent. In this work the P3- $\text{Na}^{\text{II}}\text{TiO}_2$ was used for a direct comparison with the P2 phase.

From the 2D visualization of Na layer in **Figure 4.9a**, we may see that a Na^{I} site is nearest neighbor to three Na^{II} sites, and vice versa. Therefore, the Na diffusion in the Na layer inevitably involves repeating $\text{Na}^{\text{I}} \rightarrow \text{Na}^{\text{II}} \rightarrow \text{Na}^{\text{I}}$ migrations. Under the single vacancy approximation, calculation results show that the activation energy of Na diffusion is much higher in P2 phase than that in P3 phase (**Figure 4.9c** and **d**). From **Figure 4.9b**, we can see that the transient state is reached when Na ion occupy the Na^{I} site, and thus above results are easy to understand: in P2 phase, the face-sharing Na^{I} site suffers more electrostatic repulsion from the Ti ions, leading to a high energy barrier during the Na ion diffusion process; for comparison, the Na^{I} site is equivalent to Na^{II} site in P3 phase, resulting in a lower Na ion diffusion barrier.

Under single vacancy approximation, the calculations seem to contradict the experiments, which suggest a better Na-ion diffusion kinetics in P2 phase than that in P3 phase. Nevertheless for the P-type Na_xMeO_2 ($\text{Me} = 3d$ transition metal), the Na content x is less than 1.0 ($0.6 < x < 1.0$ in our case), and therefore Na vacancy clusters are always expected in practical electrode materials. Next we try to study the Na diffusion behavior in the presence of more vacancies. The divacancy model is constructed by removing two adjacent Na ions from Na^{II} site, as shown in **Figure 4.9e**. After relaxation, the Na ion nearest to the divacancy migrate from the Na^{II} site to the Na^{I} site between the two vacancies (**Figure 4.9f**). This spontaneous migration is

consistent with previous report, indicating that the Na ion starts to occupy the Na^I site when more than one Na vacancy is formed. Besides, we find no stable configuration other than that shown in **Figure 4.9b**, suggesting that all Na ions are fixed in the case of divacancy and more vacancies are necessary for Na-ion diffusion.

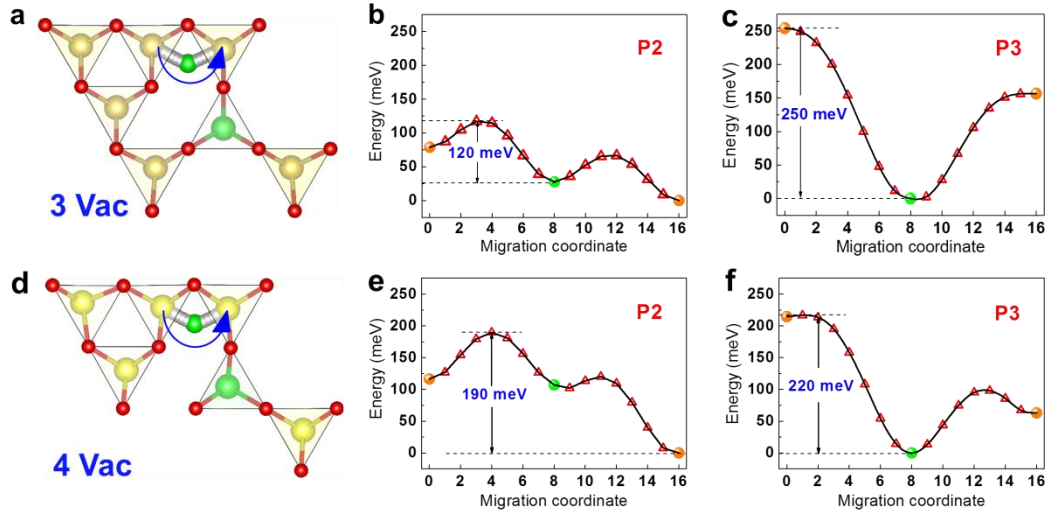


Figure 4.10 Calculated energy barriers and trajectories of Na-ion diffusion in P2- and P3-NaTiO₂. (a) Schematic of Na-ion diffusion path in layered P-type structures in the case of three Na vacancies. The Na^IO₆ and Na^{II}O₆ prisms are represented by green and yellow colors, respectively. (b) Na-ion diffusion barrier of P2-type phase under condition of three Na vacancies. (c) Na-ion diffusion barrier of P3-type phase under condition of three Na vacancies. (d) Schematic of Na-ion diffusion path in layered P-type structures in the case of four Na vacancies. (e) Na-ion diffusion barrier of P2-type phase under condition of three Na vacancies. (f) Na-ion diffusion barrier of P3-type phase under condition of three Na vacancies.

On the basis of above “rigid” divacancy model, we create more Na vacancies to study the Na ion diffusion process with the presence of Na^I ion. For the three vacancies condition (**Figure 4.10a**), the energy barrier of Na-ion migration from one Na^{II} site to another in P2 phase is calculated to be 120 meV (**Figure 4.10b**), not only far below the single vacancy case, but also lower than that of three vacancies condition in P3 phase (**Figure 4.10c**). In the case of four vacancies (**Figure 4.10d**), the Na-ion migration barrier is calculated to be 190 and 220 meV for P2 and P3 phase, respectively (**Figure 4.10e** and **f**). After introducing Cr element in Ti site, the

results are consistent (**Figure 4.11**), suggesting that the Na diffusion kinetics is determined by the structural difference (P2 vs. P3) and independent of transition metal ions.

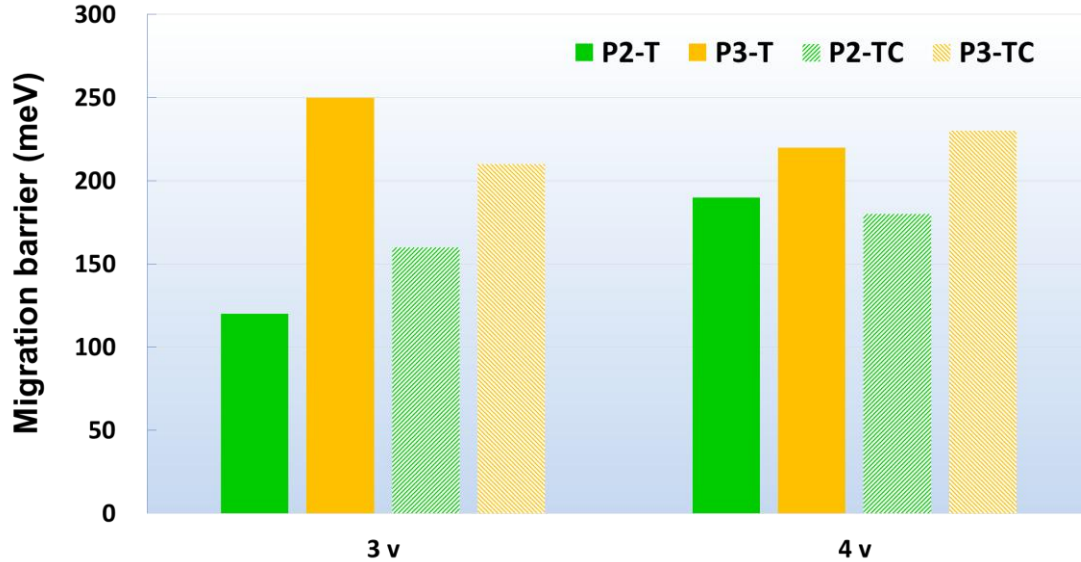








Figure 4.11 Calculated energy barrier of Na ion diffusion process, in the case of three vacancies (3v) and four vacancies (4v), in NaTiO_2 (solid bars) and $\text{NaTi}_{0.44}\text{Cr}_{0.56}\text{O}_2$ (shaded bars) with layered P2 (green) and P3 (orange) structures.

Analyzing above calculation results, we may see that the energy barrier of Na-ion diffusion is largely determined by the energy differences between the Na^{I} and Na^{II} sites. The site energy difference can approximatively be attributed to the intralayer Na interaction and transition metal (Ti or Cr) repulsion. We qualitatively show the effects of the two main factors on the Na^{I} site energy (relative to the Na^{II} site) in **Table 4.2**. Under the single vacancy approximation, the intralayer Na ion interaction (in both P2 and P3 phases) cause an increase in the energy of Na^{I} site (relative to that of Na^{II} site), which is denoted by an up arrow. The transition metal repulsion, however, differ in the two phases: for the P2 phase, as we have mentioned earlier, the Na^{I} ion suffers much higher electrostatic repulsion from the transition metal ions, which greatly increases the Na^{I} site energy; while in the P3 phase, the Na^{I} ion gains no more energy from the transition metal repulsion compared with the Na^{II} ion, and therefore the relative

energy of Na^I site is solely determined by the intralayer Na ion interactions, leading to a much lower energy barrier.

Table 4.2 Factors influencing the energy of the Na^I site relative to that of the Na^{II} site. Two major factors, i.e., the intralayer Na interaction and the transition metal repulsion, are considered. The up/down arrow indicates an increase/decrease in the relative Na^I site energy. The consequent Na^I site energy is a combination of the two factors and quantitatively represented by the blue arrow.

Factors influence Na ^I site energy		Single Na vacancy	More Na vacancy
P2	Intra-layer Na interaction		
	Transition metal repulsion		
P3	Intra-layer Na interaction		
	Transition metal repulsion	—	—

In the case of more Na vacancies, the essential difference from the single vacancy approximation lies in the occupation of Na^I site. The occupied Na^I site reduces the site energy of its adjacent Na^I site, making the Na^I site more energetically favorable than the Na^{II} site. Therefore, the intralayer Na ion interaction of more Na vacancy cases is represented by a down arrow in Table 1. As the transition metal repulsion has no contribution to the relative energy of Na^I site in P3 phase, we can see from **Figure 4.10 (c and f)** that the Na ion reaches an energy minimum at the Na^I site. For the P2 phase, however, the transition metal repulsion tend to increase the relative energy of Na^I site, thereby counterbalancing the intralayer Na-ion interaction to some extent, resulting in a low activation energy barrier for Na-ion diffusion. In aggregate, the mobility of Na ions in P2 phase are greatly promoted by the presence of multi-vacancies, rationalizing the excellent electrochemical performance of P2-NTCO electrode.

In addition to the first-principles calculation, GITT (galvanostatic intermittent titration technique) was also experimentally performed to compare the Na-ions

mobility in P2 and P3-NTCO materials. **Figure 4.12** shows the variation of a chemical diffusion coefficient of Na-ions (D_{Na}) in P2-NTCO and P3-NTCO respectively determined from the GITT profiles. Both the Na-ion diffusion coefficients present a downward trend during discharge process or a rising trend during charge process. This variation of sodium ion diffusion during the whole cycling process may be due to the increase or decrease of the vacancies in the crystal structure. The D_{Na} in P2-NTCO exhibits $1 \times 10^{-12} - 2 \times 10^{-13} \text{ cm}^2 \text{ S}^{-1}$, which is remarkably higher than the corresponding Na diffusivity in P3-NTCO ($2 \times 10^{-13} - 9 \times 10^{-14} \text{ cm}^2 \text{ S}^{-1}$). Both the calculation results and GITT measurement demonstrated that Na-ion diffusion in P2 phase is faster than that of P3 phase.

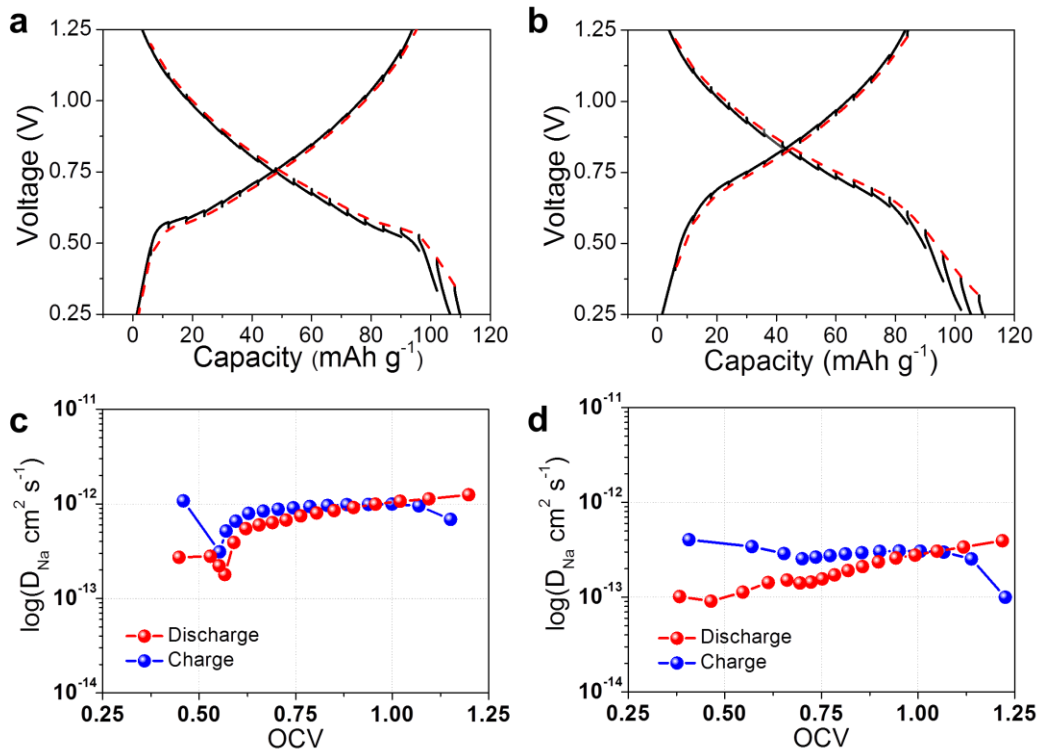


Figure 4.12 (a) GITT potential profiles of layered P2-NTCO in the second discharge-charge process at the current density of 6 mA g^{-1} with the time interval of 3h. (b) GITT potential profiles of layered P3-NTCO in the second discharge-charge process at the current density of 6 mA g^{-1} with the time interval of 3h. (c) diffusion coefficients of Na^+ in layered P2-NTCO at different discharge-charge states. (d) diffusion coefficients of Na^+ in layered P3-NTCO at different discharge-charge states.

4.4 Conclusions

In summary, the polytype P2- $\text{Na}_{0.62}\text{Ti}_{0.37}\text{Cr}_{0.63}\text{O}_2$ and P3- $\text{Na}_{0.63}\text{Ti}_{0.37}\text{Cr}_{0.63}\text{O}_2$ with nearly the same composition and different layered structures were successfully synthesized, their sodium storage performance were investigated and compared in detail, and the bridge between crystal structures, migration paths and electrochemical properties was well set up for the first time. The excellent rate capability (66 mAh g^{-1} at a 10C rate) and cycling performance (77.5% capacity retention after 1000 cycles) as well as a safe sodium insertion/extraction potential of 0.73 V in P2- $\text{Na}_{0.62}\text{Ti}_{0.37}\text{Cr}_{0.63}\text{O}_2$ suggest that it is a promising anode candidate of sodium-ion batteries for large scale energy storage. The first-principles calculation combined with GITT test was conducted to investigate the essential distinction between P2 and P3 phase. The DFT calculations clearly reveal the sodium diffusion barrier in P2 phase is greatly reduced under the condition of multi-vacancies, even lower than that of P3 phase, which is consistent with the experimental results of GITT test. In essence, Na diffusion kinetics is determined by the structural difference (P2 vs. P3) and almost independent of transition metal ions. The relationship of crystal structure-migration path-electrochemical performance is well established in layered P-type structures for the first time, and this work combined experimental and calculated method also provide new avenues for designing advanced electrode materials of sodium-ion batteries.

Chapter 5 Layered $\text{Na}_{0.8}\text{Ni}_{0.4}\text{Ti}_{0.6}\text{O}_2$ as bipolar electrode materials for sodium-ion batteries

5.1 Introduction

Due to the increasing concerns about fossil fuels depletion, renewable energy such as wind and solar power has been widely developed in the modern electrical grid.^{1, 84} However, renewable energy is intermittent, and it needs to be balanced and integrated into the grid smoothly and safely. To smooth out its variation over time, low-cost electrical energy storage (EES) becomes extremely necessary. Electrochemical batteries can efficiently store and release electricity in chemicals, showing the most promising in stationary applications for EES. Although lithium ion batteries (LIBs) have been considered for electrical grid storage, their limited availability and increasing cost with worldwide commercialization cannot satisfy the substantial demand.^{3, 4, 85-88} Nevertheless, sodium possessing the similar physical and chemical properties with lithium has almost infinite supply, and has attracted great attentions to develop room-temperature sodium-ion batteries (SIBs).^{6, 34, 51, 89-94}

Great efforts have been made in the design of SIBs with high efficiency. Layered oxide compounds ($\text{Na}_{2/3}\text{Ni}_{1/3}\text{Ti}_{2/3}\text{O}_2$, $\text{Na}_{2/3}\text{Fe}_{1/2}\text{Mn}_{1/2}\text{O}_2$, $\text{Na}_{0.85}\text{Li}_{0.17}\text{Ni}_{0.21}\text{Mn}_{0.64}\text{O}_2$)^{67, 90, 95} polyanion compounds ($\text{Na}_3\text{V}_2(\text{PO}_4)_3$, $\text{Na}_{1.5}\text{VPO}_{4.8}\text{F}_{0.7}$, $\text{Na}_7\text{V}_4(\text{P}_2\text{O}_7)_4\text{PO}_4$)^{23, 96-98}, Prussian blue^{51, 99, 100} and carbon compounds (graphite, hard carbon)^{30, 101} have been extensively investigated, and computational techniques have also been applied recently to a variety of sodium-based compounds. Most of the full sodium cells are non-symmetric, consisting of layered NaMeO_2 (where the transition metal Me is the element of V, Cr, Mn, Fe, Co and Ni) cathode and carbon/sodium metal anode as sodium ions “stocking chair” reaction components. However, potential safety concerns on carbon materials (especially hard carbon) with possible thermal runaway are noticed because their voltage plateau related with most capacity is too close to the sodium plating voltage. This kind of SIBs system cannot support the requirement of long life and safety of large-scale energy storage devices, therefore development of new sodium storage system is necessary.^{31, 102}

Recently, the full symmetric vanadium or titanium-based SIBs in terms of two $\text{Me}^{4+}/\text{Me}^{3+}$ and $\text{Me}^{3+}/\text{Me}^{2+}$ redox couples in $\text{Na}_3\text{Me}_2(\text{PO}_4)_3$ (here, Me only represents Ti or V) with NASICON structure have been proposed.¹⁰³⁻¹⁰⁵ These symmetric SIBs are very attractive and promising from a commercial standpoint, cathode and anode with the same active materials can enable cells overcharging to some extent, buffer the large volume expansion (cathode expanding accompanied by anode shrinking, and vice versa), greatly reduce the manufacturing costs and simplify the fabrication process.^{106, 107} Although, their cycle instability (only few cycles can be conducted) and low energy density (low average potential of 1.7 V) of current developed symmetric SIBs are insufficient for long-term operation in EES, preventing the further application of symmetric cells. Hence, developing bipolar materials with good cycle performance to build safe, inexpensive and long-life full symmetric SIBs is a great challenge.

In the past studies, NaNiO_2 and NaTiO_2 layered oxide can serve as cathode and anode materials of SIBs through the redox of nickel and titanium, respectively. However, complex phase transformation with evident step-like character in NaNiO_2 material exists during their desodiation and sodiation,^{7, 108} and also the layered O3-type Na_xTiO_2 is not stable for the Ti^{3+} chemical environment.^{8, 31} Our recent studies have clearly confirmed that solid-solution of NaMeO_2 and NaTiO_2 layered oxides can well improve the comprehensive electrochemical performance, especially on the cycle capability.^{59, 109} Considering the similar ionic radius of nickel and titanium, we designed and synthesized the solid-solution material of O3-type $\text{Na}_{0.8}\text{Ni}_{0.4}\text{Ti}_{0.6}\text{O}_2$ without impurities, and the ‘golden pair’ of nickel and titanium not only greatly stabilize each other in the sodium electrochemical processes, but also exhibit the unique double redox couples of $\text{Ni}^{4+}/\text{Ni}^{2+}$ (3.5 V) and $\text{Ti}^{4+}/\text{Ti}^{3+}$ (0.7 V). These advantages of this bipolar material are used to implement a novel symmetric SIB. This cell exhibits a reversible discharge capacity of 85 mAh g^{-1} with the average voltage of 2.8 V. It also presents a superior long life exceeding 150 cycles with capacity retention of 75%.

5.2 Experimental and Characterization

5.2.1 Preparation of O3-type $\text{Na}_{0.8}\text{Ni}_{0.4}\text{Ti}_{0.6}\text{O}_2$

O3-type $\text{Na}_{0.8}\text{Ni}_{0.4}\text{Ti}_{0.6}\text{O}_2$ raw materials are synthesized by solid-state reaction. All solid chemical compounds were purchased from Wako Pure Chemicals Industries Ltd.. The precursors of Na_2CO_3 , NiO and TiO_2 (anatase form) are well ground in an agate mortar at a rotate rate of 200 r/min for 20 h. Owing to the sodium volatility in high temperature, an excess 5 wt.% of Na_2CO_3 is added. The mixture is dried for 12 h at 100 °C. The obtained powders were pressed into pellets, and then the pellets were heated at 900 °C for 15 h in the Ar flow. The heated pellets were quenched to room temperature and stored in an argon-filled glove box until use.

5.2.2 Characterization

The HR-SXRD patterns were collected in a transmission mode at the beam line 11-BM-B of the Advanced Photon Source, Argonne National Laboratory, USA. A monochromatic X-ray beam with an energy of 30 keV (wavelength of 0.413742 Å) was used. The ex-situ XRD patterns were performed using Cu $\text{K}\alpha$ radiation on a Bruker D8 Advance Diffractometer. The detailed structural information of as-prepared materials was also observed using scanning electron microscopy (SEM, TOPCON DS-720 instrument) and Cs-corrected transmission electron microscope (TEM, JEOL, JEM-2010 and JEM-2100F). The charged cathodes scratched from the electrodes of sodium half cells were subjected to XPS on a VG Theta Probe. Thermal stability was examined by differential scanning calorimetry (DSC) on EXSTAR 7000 X-DSC in a temperature range of 50-400 °C at a heating rate of 10 °C min^{-1} . Before DSC measurements, the cells were firstly charged to 4.0 V or discharged at 0.01 V at a current of 20 mA g^{-1} . After that, the cells were disassembled in an Ar filled glove box, the charged or discharged samples were collected and sealed in Al-pan for DSC measurements.

5.2.3 Electrochemical test

The electrochemical tests of $\text{Na}_{0.8}\text{Ni}_{0.4}\text{Ti}_{0.6}\text{O}_2/\text{Na}$ half cells were carried out using the CR2032 coin-type cells, consisting of a cathode and sodium metal anode separated by a glass fiber sheet. The cathode electrodes were prepared with a weight ratio of 70% of active material, 25% of teflonized acetylene black, and 5% of polytetrafluoroethylene. Pellets for half cells were pressed in the form of aluminium screens approximately 3 mg in mass and 7 mm in diameter (the loading mass is around 1.95 mg cm^{-2}), then dried under vacuum at about $110 \text{ }^\circ\text{C}$ for 5 h before cells assembly. The cells were assembled in a glove box filled with dried argon gas. The electrolyte was 1 mol dm^{-3} NaClO_4 dissolved in propylene carbonate (Tomiya Pure Chemical Industries) with 2 vol% fluorinated ethylene carbonate as an electrolyte additive. The $\text{Na}_{0.8}\text{Ni}_{0.4}\text{Ti}_{0.6}\text{O}_2/\text{Na}$ half cells were cycled in the voltage range of 2-4 V for cathode performance and 0.01-2.5 V for anode performance. Prior to full cells fabrication, the pre-sodiation of $\text{Na}_{0.8}\text{Ni}_{0.4}\text{Ti}_{0.6}\text{O}_2$ anode and pre-desodiation of $\text{Na}_{0.8}\text{Ni}_{0.4}\text{Ti}_{0.6}\text{O}_2$ cathode were performed to carry out the first cycle activation. The cell balance was achieved by setting the electrode mass ratio of cathode/anode to 1.4 (the anode loading mass is around 1.95 mg cm^{-2}). The full cell is then anode limited and is reassembled and cycled in the voltage of 0.6-3.8 V. 1C corresponds to 100 mA g^{-1} for all the cell tests.

5.3 Results and discussion

5.3.1 Structural characterization

Figure 5.1a shows the schematic of proposed sodium-ion batteries, and the brown, yellow and green parts represent anode, electrolyte and cathode, respectively. In the traditional SIBs, the cathode is different from the anode to generate a certain voltage gap and supply an applicable energy density. Herein, we use the “unique” electrode of O3-type $\text{Na}_{0.8}\text{Ni}_{0.4}\text{Ti}_{0.6}\text{O}_2$ simultaneously as cathode and anode. This novel design ensures the safety, is more tolerant of overcharge, reduces the comprehensive cost and makes cell recycling more convenient.^{106, 107} Figure 5.1b is a schematic of energy vs. density of states plot, showing the relative position of the

Fermi energy level of $\text{Ni}^{4+}/\text{Ni}^{2+}$ ($\text{Ni}^{4+}/\text{Ni}^{3+}$ and $\text{Ni}^{3+}/\text{Ni}^{2+}$) and $\text{Ti}^{4+}/\text{Ti}^{3+}$ redox couples for O3-type $\text{Na}_{0.8}\text{Ni}_{0.4}\text{Ti}_{0.6}\text{O}_2$. To illustrate these redox couple, the CV curve with a wide voltage range of 0-4 V in the half cell of $\text{Na}_{0.8}\text{Ni}_{0.4}\text{Ti}_{0.6}\text{O}_2/\text{Na}$ is carried out in the right of Figure 5.1c. It is clear that two distinct redox peaks of around 3.6/3.5 V and 0.95/0.7 V are observed, surprisingly there is a large potential difference between the two redox couples. Bivalence of nickel and tetravalence of titanium are further validated from their potentials vs. Na, which is also used to fabricate series of materials with different compositions.^{110, 111} The results indicate that two elements (Ni and Ti) of the same materials can be simultaneously oxidized and reduced in an electrochemical process, and stimulate us to develop a novel symmetric SIB. The background of Figure 5.1c depicts that our novel symmetric cells after charge to 3.8 V vs. Na^+/Na successfully light 2 LED lamps.

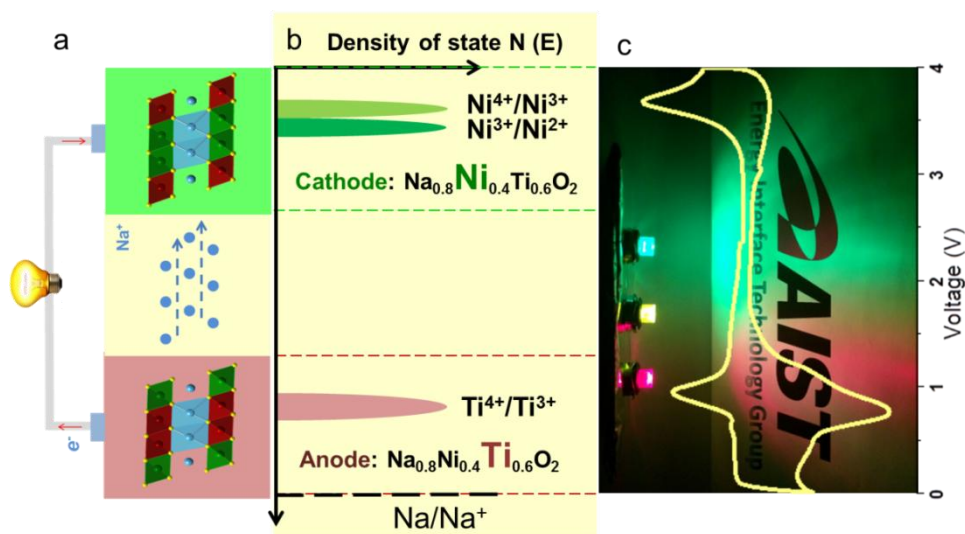


Figure 5.1 (a) A diagram of the proposed symmetric cell based on O3-type $\text{Na}_{0.8}\text{Ni}_{0.4}\text{Ti}_{0.6}\text{O}_2$. (b) schematic of energy vs. density of states plot, showing the relative positions of the Fermi energy level of $\text{Ni}^{4+}/\text{Ni}^{2+}$ ($\text{Ni}^{4+}/\text{Ni}^{3+}$ and $\text{Ni}^{3+}/\text{Ni}^{2+}$) and $\text{Ti}^{4+}/\text{Ti}^{3+}$ redox couples for O3-type $\text{Na}_{0.8}\text{Ni}_{0.4}\text{Ti}_{0.6}\text{O}_2$. (c) The CV curve of $\text{Na}_{0.8}\text{Ni}_{0.4}\text{Ti}_{0.6}\text{O}_2/\text{Na}$ half cell in the whole voltage range of 0-4 V vs. Na^+/Na , and the background shows the lighted LED bulbs driven up by the designed bipolar $\text{Na}_{0.8}\text{Ni}_{0.4}\text{Ti}_{0.6}\text{O}_2$ -based symmetric cells.

The crystal structures of the bipolar material were characterized by

high-resolution synchrotron X-ray diffraction (HR-SXRD), displaying O3-type structure with high crystallinity. The composition of $\text{Na}_{0.83}\text{Ni}_{0.40}\text{Ti}_{0.60}\text{O}_2$ is confirmed by Inductively Coupled Plasma Mass Spectrometry (ICP-MS), which is closely matching the designed product. All the diffraction peaks of the bipolar material can be well indexed to rhombohedral symmetry structure with $R\bar{3}m$ space group (Figure 5.2a). The Rietveld refinement using the RIETAN-FP program gives the lattice parameters of $a=b=2.96785(2)$ Å and $c=16.27990(9)$ Å. The other refined structural parameters are summarized in Table 5.1. The calculated patterns (circles in Figure 5.2a) were in good agreement with experimental data (red lines in Figure 5.2a), indicative of a pure O3-type structure, isostructural with $\alpha\text{-NaFeO}_2$. The scanning electron microscopy (SEM) image in the inset of Figure 5.2a, reveals that layered $\text{Na}_{0.8}\text{Ni}_{0.4}\text{Ti}_{0.6}\text{O}_2$ samples consist of interconnected primary particles with a size of about 100-500 nm. A schematic illustration of the structure model of O3-type $\text{Na}_{0.8}\text{Ni}_{0.4}\text{Ti}_{0.6}\text{O}_2$ is presented in Figure 5.2b. In this model, nickel and titanium ions are accommodated in the octahedral sites of MeO_2 layer (3a sites, Me = Ni and Ti), while sodium ions are located in the octahedral sites of NaO_2 layer (3b sites).

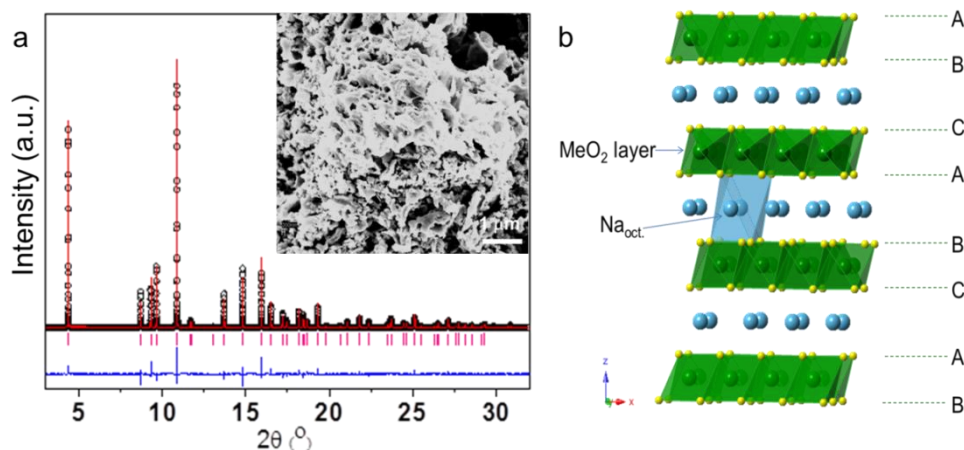


Figure 5.2 (a) HR-SXRD pattern and Rietveld refinement of layered $\text{Na}_{0.8}\text{Ni}_{0.4}\text{Ti}_{0.6}\text{O}_2$ material. A red line represents the observed intensities; The calculated pattern is shown with black circles; The difference between the observed and calculated intensities is presented by a blue curve; Pink short vertical bars indicate the position of standard Bragg reflections. The inset shows SEM image of $\text{Na}_{0.8}\text{Ni}_{0.4}\text{Ti}_{0.6}\text{O}_2$ samples. (b) Schematic illustration of the crystal structure for O3-type

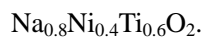


Table 5.1 Lattice parameters of O3-type $\text{Na}_{0.8}\text{Ni}_{0.4}\text{Ti}_{0.6}\text{O}_2$ sample after Rietveld refinement.

Phase	O3	
Space Group	Rhombohedral	
Cell parameters	a (Å)	2.96785 (2)
	b (Å)	2.96785 (2)
	c (Å)	16.27990(9)
	α (°)	90.000
	β (°)	90.000
	γ (°)	120.000
	Volume (Å ³)	124.184(1)
Agreement factors	R _{wp} (%)	14.844
	R _p (%)	10.359
	S	0.8375

The detailed crystal structure is further investigated by Selected Area Electron Diffraction (SAED) techniques. The bright spots in Figure 5.3a and 5.3b are indexed to the corresponding reflections originating from O3-type layered structure. Atomic-resolution investigation on the local structure of layered $\text{Na}_{0.8}\text{Ni}_{0.4}\text{Ti}_{0.6}\text{O}_2$ samples was also conducted by High-angle Annular Dark Field (HAADF) and Annular Bright Field (ABF) Scanning Transmission Electron Microscopy (STEM) techniques (Figure 5.2c and 5.2d). The bright-dot contrast in the HAADF-STEM images (Figure 5.2c) and the dark-dot contrast in ABF-STEM images (Figure 5.2d) reveal the sodium and transition metal (Ni and Ti) atom positions, and sodium is fully overlapped by transition metal projected along [001] direction, which is consistent with O3-type layered structure. High Resolution Transmission Electron Microscope (HR-TEM) characterization further suggests the interlayer spacing about 0.555 nm of (003) fringes in O3-type $\text{Na}_{0.8}\text{Ni}_{0.4}\text{Ti}_{0.6}\text{O}_2$ (Figure 5.3e).

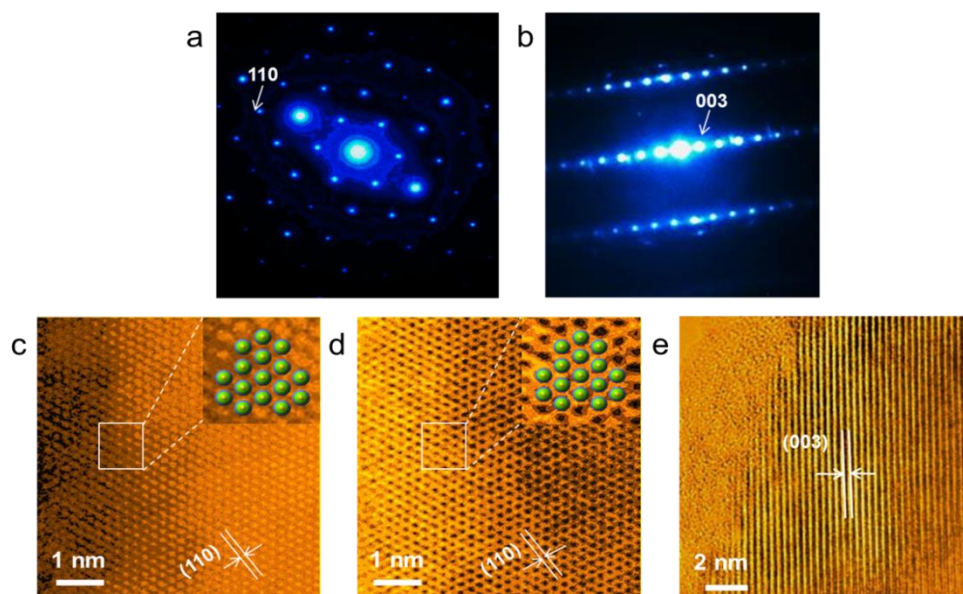


Figure 5.3 (a) and (b) SAED patterns. (c) HADDF and (d) ABF-STEM images of $\text{Na}_{0.8}\text{Ni}_{0.4}\text{Ti}_{0.6}\text{O}_2$ samples projected along [001] direction. The insets of (d) and (e) in top-right corners shows sodium (blue balls) and transition metal (green balls) occupancies. (e) HRTEM image of $\text{Na}_{0.8}\text{Ni}_{0.4}\text{Ti}_{0.6}\text{O}_2$ samples.

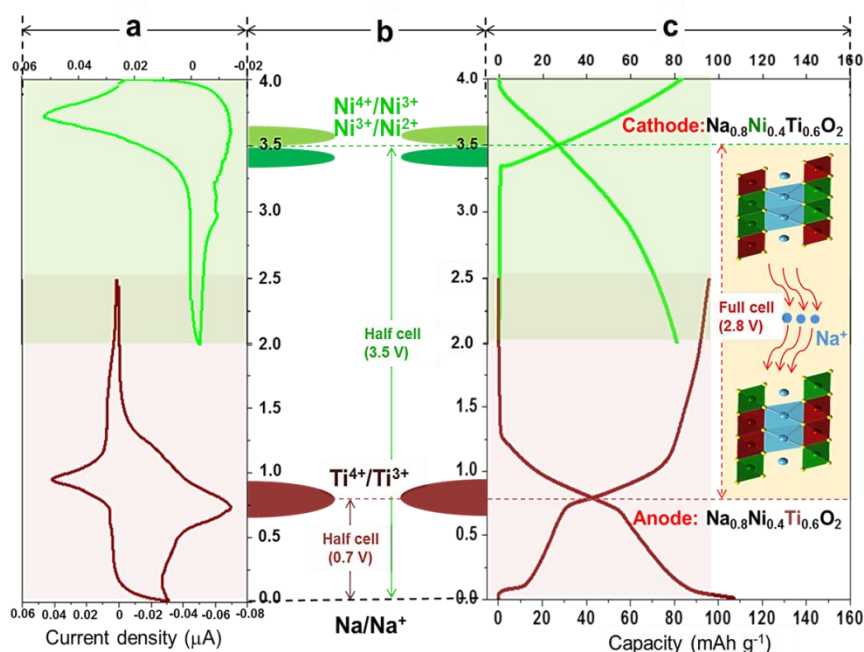


Figure 5.4 The electrochemical performance of the O3-type $\text{Na}_{0.8}\text{Ni}_{0.4}\text{Ti}_{0.6}\text{O}_2$ in the half cell vs. Na^+/Na . (a) The CV curves of O3-type $\text{Na}_{0.8}\text{Ni}_{0.4}\text{Ti}_{0.6}\text{O}_2$ in the voltage range of 2-4 V for $\text{Ni}^{4+}/\text{Ni}^{3+}$ (green) and 0.01-2.5 V for $\text{Ti}^{4+}/\text{Ti}^{3+}$ (brown) vs. Na^+/Na . (b) Schematic of potential of

the $\text{Ni}^{4+}/\text{Ni}^{3+}$, $\text{Ni}^{3+}/\text{Ni}^{2+}$ and $\text{Ti}^{4+}/\text{Ti}^{3+}$ redox couples vs. Na/Na^+ in layered $\text{Na}_{0.8}\text{Ni}_{0.4}\text{Ti}_{0.6}\text{O}_2$ materials. The insets display the average potentials of the $\text{Na}_{0.8}\text{Ni}_{0.4}\text{Ti}_{0.6}\text{O}_2/\text{Na}$ half cells as cathode and anode, respectively. (c) The typical charge-discharge or discharge-charge profiles of the $\text{Na}_{0.8}\text{Ni}_{0.4}\text{Ti}_{0.6}\text{O}_2/\text{Na}$ half cells in the voltage range of 2-4 V (green) and 0.01-2.5 V (brown) vs. Na^+/Na . The inset (yellow parts) shows the predicted average voltage of 2.8 V in the bipolar $\text{Na}_{0.8}\text{Ni}_{0.4}\text{Ti}_{0.6}\text{O}_2$ -based symmetric cells.

5.3.2 Electrochemical performance and analysis

Electrochemical properties of O3-type $\text{Na}_{0.8}\text{Ni}_{0.4}\text{Ti}_{0.6}\text{O}_2$ as bipolar material are characterized by cyclic voltammetry (CV) and galvanostatic charge-discharge or discharge-charge test in the half cells vs. Na^+/Na , shown in Figure 5.4. The CV curve in the green part of Figure 5.4a reflects an oxidation peak at 3.7 V and a weak reduction hump at 3.5 V, attributable to the redox couples of $\text{Ni}^{4+}/\text{Ni}^{2+}$ and possible phase change. Upon charging to 4 V with the initial charge capacity of 107 mAh g^{-1} in Figure 5.5a (exceeding the theoretical capacity based on $\text{Ni}^{3+}/\text{Ni}^{2+}$ redox couples), the desodiated $\text{Na}_{0.8-x}\text{Ni}_{0.4}\text{Ti}_{0.6}\text{O}_2$ samples was conducted with X-ray Photoelectron Spectroscopy (XPS) experiment in Figure 5.5b. A clear shoulder peak corresponding to Ni^{4+} (857.4 eV) was detected, which validates the proposed $\text{Ni}^{4+}/\text{Ni}^{2+}$ redox mechanism. It is known that the tetravalent nickel is unstable in the cells' disassembly process or the XPS test procedure, and is easier to change and transfer, so a small number of tetravalent nickel ions are observed in our ex-situ XPS result. Accordingly, the green part of Figure 5.4c shows the voltage profile for the typical (second) charge-discharge cycle from 2 to 4 V vs. Na^+/Na at a 0.2 C rate, demonstrating that the electrode delivers a capacity of 83 mAh g^{-1} . The charge-discharge curve displays a reversible, distinct plateau of 3.5 V, well agreeable with the CV curves. The cycle stability is further investigated with $\text{Na}_{0.8}\text{Ni}_{0.4}\text{Ti}_{0.6}\text{O}_2$ half cells in Figure 5.6a. It delivers a large reversible capacity of 63 mAh g^{-1} at a rate of 1C, corresponding to 76% of discharge capacity at a 0.2C rate with small polarization. Also, $\text{Na}_{0.8}\text{Ni}_{0.4}\text{Ti}_{0.6}\text{O}_2$ shows good cycle performance, and the

capacity still maintains 47 mAh g^{-1} after 250 cycles, the corresponding capacity retention is 75%, and the Coulombic efficiency is close to 100% except for the first cycle. Compared with layered NaNiO_2 with single transition metal, the multi-step character of charge and discharge profiles is clearly suppressed and even disappeared in the titanium-substituted $\text{Na}_{0.8}\text{Ni}_{0.4}\text{Ti}_{0.6}\text{O}_2$, replaced by the smooth charge-discharge profiles. The detailed structural change with sodium extraction and insertion will be investigated in the subsequent section.

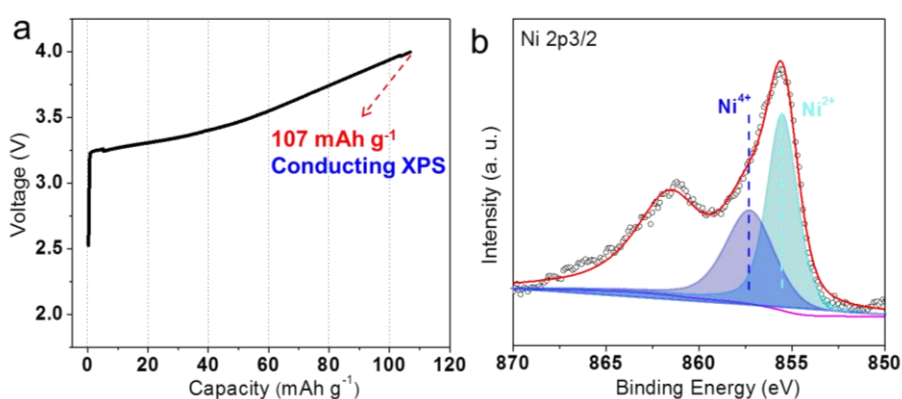


Figure 5.5 (a) The initial charge profile of $\text{Na}_{0.8}\text{Ni}_{0.4}\text{Ti}_{0.6}\text{O}_2/\text{Na}$ half cells. (b) The XPS spectra of Ni-2p peaks of the desodiated $\text{Na}_{0.8-x}\text{Ni}_{0.4}\text{Ti}_{0.6}\text{O}_2$ after initial charge process.

The CV curve in the brown part of Figure 5.4a shows the distinct redox peak about 0.7 V, which is attributed to the redox of $\text{Ti}^{4+}/\text{Ti}^{3+}$. Accordingly, the typical (second) discharge-charge profile is displayed in the brown part of Figure 5.4c, and the observed reversible capacity is 107 mAh g^{-1} , along with an obvious step around 0.7 V, which is also validated by the CV curve. The cycle stability and Coulombic efficiency are also evaluated in Figure 5.6b. The reversible capacity at a 1C rate can still maintains 62 mAh g^{-1} , and corresponds to about 58% discharge capacity of 0.2C rate. Also the capacity retention after 250 cycles is 86% and Coulombic efficiency except for initial cycles can reach nearly 100% in all the charge-discharge processes (Figure S4). In contrary to layered O3-type NaTiO_2 , nickel-substituted $\text{Na}_{0.8}\text{Ni}_{0.4}\text{Ti}_{0.6}\text{O}_2$ shows excellent structural stability with cycling, which is expected that nickel substitution greatly improve the titanium ions stability in the transition

metal layers. The structure stability will further be proved by the subsequent ex-situ XRD structural evolution analysis in the discharge-charge process.

Figure 5.4b shows the schematic of electric potential for the $\text{Ni}^{4+}/\text{Ni}^{2+}$ and $\text{Ti}^{4+}/\text{Ti}^{3+}$ redox couples in O3-type $\text{Na}_{0.8}\text{Ni}_{0.4}\text{Ti}_{0.6}\text{O}_2$, corresponding to the average voltage of $\text{Na}_{0.8}\text{Ni}_{0.4}\text{Ti}_{0.6}\text{O}_2/\text{Na}$ half cells. On the basis of their voltage difference, the average potential of this symmetric cell using the bipolar active materials $\text{Na}_{0.8}\text{Ni}_{0.4}\text{Ti}_{0.6}\text{O}_2$ is predicted, shown in the inset of Figure 5.4c.

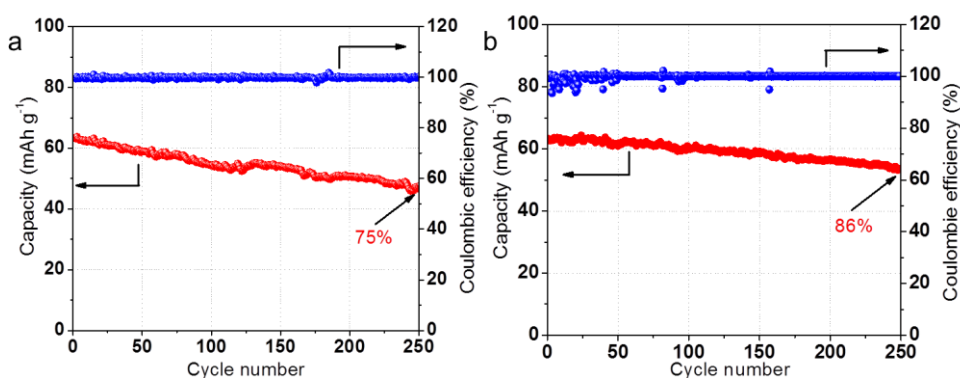


Figure 5.6 (a) Cycle performance and relative coulombic efficiency of $\text{Na}_{0.8}\text{Ni}_{0.4}\text{Ti}_{0.6}\text{O}_2/\text{Na}$ half cell with the voltage range of 2-4 V for 250 cycles at a 1C rate. (b) Cycle performance and relative coulombic efficiency of $\text{Na}_{0.8}\text{Ni}_{0.4}\text{Ti}_{0.6}\text{O}_2/\text{Na}$ half cell with the voltage range of 0.01-2.5 V for 250 cycles at a 1C rate.

In order to depress the polarization and irreversibility effect of $\text{Na}_{0.8}\text{Ni}_{0.4}\text{Ti}_{0.6}\text{O}_2$ in the first charge process (cathode side) and discharge process (anode side), the pre-desodiated and pre-sodiated $\text{Na}_{0.8}\text{Ni}_{0.4}\text{Ti}_{0.6}\text{O}_2$ are used as positive and negative electrode materials in the sodium full cells. Full batteries containing desodiated and sodiated $\text{Na}_{0.8}\text{Ni}_{0.4}\text{Ti}_{0.6}\text{O}_2$ were characterized using CV and galvanostatic cycling. Figure 5.7a illustrates the CV curve of the full cell with the optimized voltage range of 0.6-3.8 V. An oxidation peak with average voltage of 3.0 V and a reduction peak with average voltage of 2.8 V were observed, which is consistent with the predicted value in the inset of Figure 5.4c. A reversible discharge capacity of 85 mAh g^{-1} was obtained in the first cycle (inset of Figure 5.7b) and subsequent cycles (Figure 5.7b) at a charge-discharge rate of 0.2 C. As shown in Figure 5.7b, the charge-discharge

profile displays symmetrical characteristic, and it is clearly seen that no obvious polarization is observed in this well-configured symmetric full cells. The rate capability is also evaluated with different charge-discharge rates of 0.2C, 0.5C and 1C in Figure 5.7c. The reversible capacity can be 67 mAh g⁻¹ at a 0.5C rate, and even with the rate of 1C, the discharge capacity remains 53 mAh g⁻¹, approximately 62% of the reversible capacity at a 0.2C rate. With a rate of 1C, the symmetric battery offers 75% of capacity retention for extensive cycling of 150 times sodium extraction and insertion, and the corresponding Coulombic efficiency is exceeding 97% except for the initial cycle (Figure 5.7d).

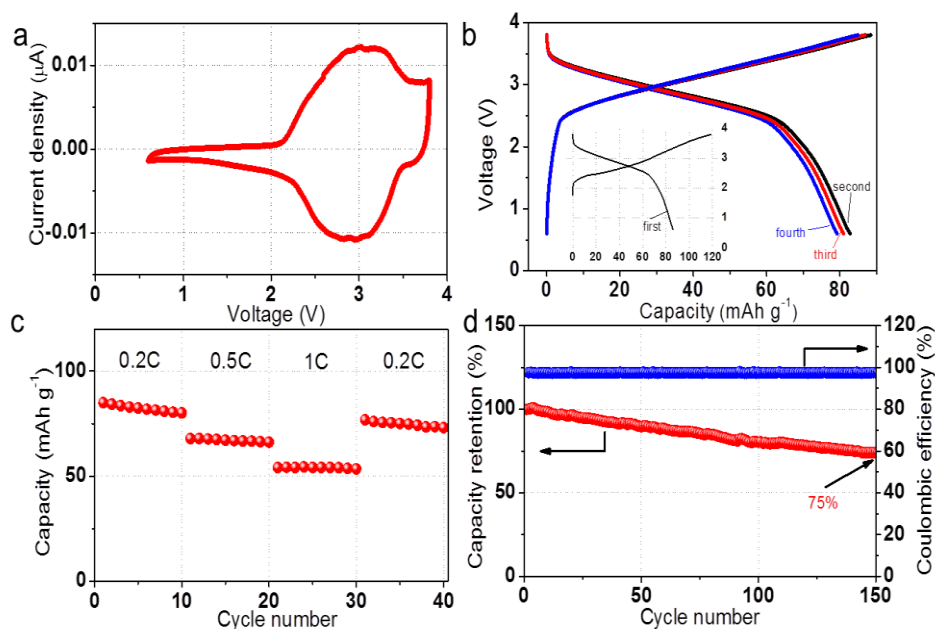


Figure 5.7 The electrochemical performance of bipolar Na_{0.8}Ni_{0.4}Ti_{0.6}O₂-based symmetric cells. (a) The CV curve in the voltage range of 0.6-3.8 V. (b) The typical charge-discharge profiles in the voltage range of 0.6-3.8 V; inset is the initial charge-discharge profile. (c) The rate capability at different rates of 0.2C, 0.5C and 1C. (d) The cycling performance with Coulombic efficiency at a 1C rate.

5.3.3 Sodium storage mechanism

To understand the reaction mechanism of O3-type Na_{0.8}Ni_{0.4}Ti_{0.6}O₂ during sodium insertion and extraction processes, we performed the ex-situ XRD and STEM

experiments in the $\text{Na}_{0.8}\text{Ni}_{0.4}\text{Ti}_{0.6}\text{O}_2/\text{Na}$ half cell. Figure 5.8a shows the initial charge-discharge profile, in which the green points are denoted for ex-situ XRD and STEM test. It is evident that the initial phase is O3-type rhombohedral (Figure 5.8b, point 1), and the patterns of O3 layered structure broaden, weaken with desodiation and a new phase appears (Figure 5.8b). This phase is assigned to P3-type monoclinic,^{46, 112, 113} having an interlayer distance larger than that of O3-type layer structure, continues to strengthen and become the dominant after the full desodiation (Figure 5.8b).^{46, 112, 113} It is also validated by the intensity ratio of $(104)_{\text{hex}}$ and $(105)_{\text{hex}}$ diffraction (the intensity of the $(104)_{\text{hex}}$ diffraction line is stronger for O3 phase, while that of the $(105)_{\text{hex}}$ line is stronger for P3 layered structure) in Figure 5.8b.¹¹⁴ In order to distinguish P3 phase from O3 phase, the expanded view of ex-situ XRD patterns is shown in Figure 5.8d. In the P3 phase, Na is in trigonal prismatic coordination, which is simply caused by the $\text{MeO}_2^{\delta-}$ layers with less negative charge so that the trigonal prismatic environment is favored over the octahedral one.^{102, 113} On discharge, the P3-type monoclinic phase remains at the partial sodiation and mostly transforms back into the original O3-type layer structure (Figure 5.8d). And the O3 structure dominates with a weak peaks belonging to P3 structure (Figure 5.8d), and the schematic of the O3-P3 phase transition was shown in Figure 5.9. SAED and HAADF and ABF-STEM tests projected along $[1\bar{1}0]$ direction were also conducted in the desodiated materials after charge to 4V (Figure 5.8a). Figure 5.8c is the corresponding SAED patterns and STEM image, and bright spots are indexed to the corresponding reflection of P3 layered structure. Owing to the phase transition from O3 to P3 and structural distortion, it is difficult to detect the atom occupancies in P3 layered structure and the increased interlayer spacing of 0.566 nm corresponding to (003) fringes is observed in Figure 5.8c.

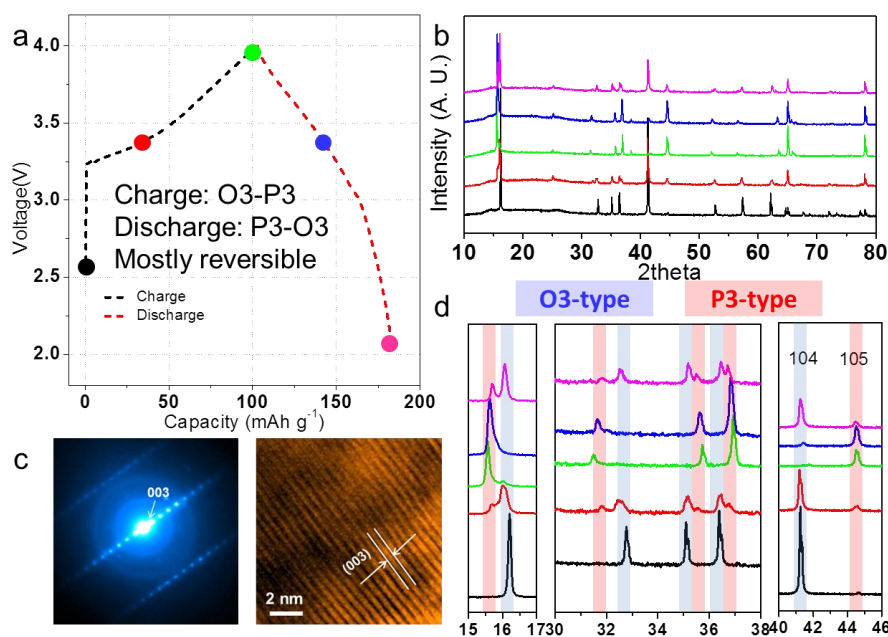


Figure 5.8 Structural evolution using $\text{Na}_{0.8}\text{Ni}_{0.4}\text{Ti}_{0.6}\text{O}_2$ as cathode (a) The first charge-discharge profile of the $\text{Na}_{0.8}\text{Ni}_{0.4}\text{Ti}_{0.6}\text{O}_2/\text{Na}$ half cell in a low potential area, and the green points correspond to the different charge-discharge states conducted by ex-situ XRD experiment. (b) The ex-situ XRD patterns of $\text{Na}_{0.8}\text{Ni}_{0.4}\text{Ti}_{0.6}\text{O}_2$ at the different charge-discharge states shown in a. (c) The SAED patterns and TEM image of the fully charged $\text{Na}_{0.8}\text{Ni}_{0.4}\text{Ti}_{0.6}\text{O}_2$ samples projected along $[1\bar{1}0]$ direction. (d) The expanded view in the regions of $15\text{-}17^\circ$ and $30\text{-}38^\circ$ for the ex-situ XRD patterns shown in b.

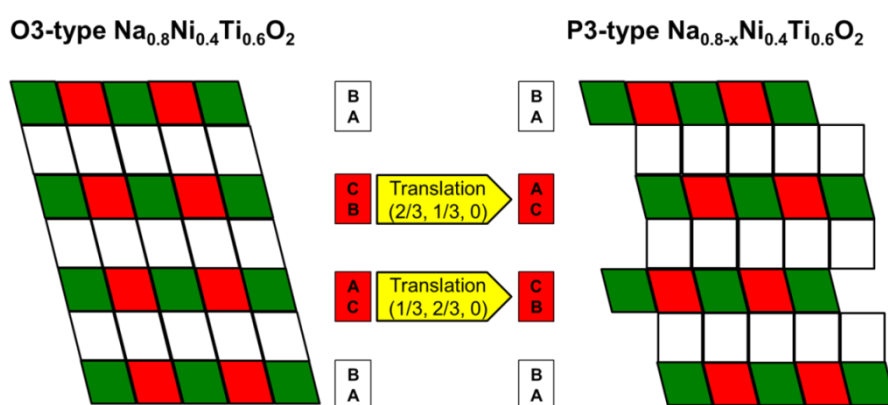


Figure 5.9 Schematic of the phase transition from O3-type $\text{Na}_{0.8}\text{Ni}_{0.4}\text{Ti}_{0.6}\text{O}_2$ to P3-type $\text{Na}_{0.8-x}\text{Ni}_{0.4}\text{Ti}_{0.6}\text{O}_2$ in the half cell of $\text{Na}_{0.8}\text{Ni}_{0.4}\text{Ti}_{0.6}\text{O}_2/\text{Na}$ with the voltage range of 2-4 V.

Figure 5.10a displays the first discharge-charge profile in the $\text{Na}_{0.8}\text{Ni}_{0.4}\text{Ti}_{0.6}\text{O}_2/\text{Na}$ half cell, in which the colored points are denoted for ex-situ XRD and STEM test. All peaks are unchanged, shift weakly with sodium insertion and extraction (Figure 5.10b), demonstrating the high structural stability during cycling. No other distinct new phase is generated during the first cycle, suggesting that this structure is flexible enough to accommodate the structural changes accompanying the extraction and insertion of the large sodium ions in a low potential area. Otherwise, the sample at discharge of 0.01 V displays the typical bright spots corresponding to the corresponding reflection originating from O3 layered structure in the SAED patterns (Figure 5.11a). HAADF and ABF-STEM images of Figure 5.11b and c suggest that the typical sodium and transition metal occupancies completely overlap with typical O3 structure (the enlarged views are shown in Figure 5.11d and e), which further verified the structural stability in sodium extraction and insertion process.

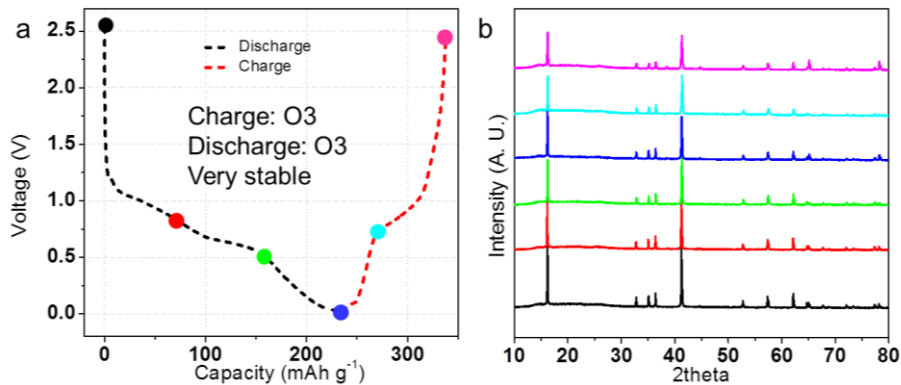


Figure 5.10 (a) The first discharge-charge profile of the $\text{Na}_{0.8}\text{Ni}_{0.4}\text{Ti}_{0.6}\text{O}_2/\text{Na}$ half cell, and the different colorful points correspond to the different discharge-charge states conducted by ex-situ XRD experiment. (b) The ex-situ XRD patterns of $\text{Na}_{0.8}\text{Ni}_{0.4}\text{Ti}_{0.6}\text{O}_2$ at the different discharge-charge states shown in a.

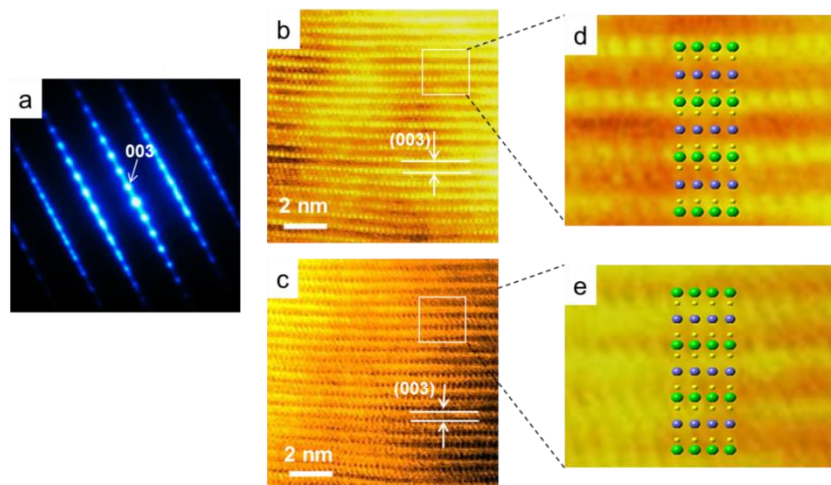


Figure 5.11 (a) The SAED patterns (b) HAADF-STEM image and (c) ABF-STEM image of the fully discharged $\text{Na}_{0.8}\text{Ni}_{0.4}\text{Ti}_{0.6}\text{O}_2$ samples projected along [100] direction. (d) and (e) The enlarged area corresponding to the white rectangle in (b) and (c), showing the typical sodium (blue) and transition metal (green) occupancies in O3 layered structure.

Differential scanning calorimetry (DSC) with this bi-polar material at different conditions is conducted to investigate the thermal stability, shown in Figure 5.12. The pristine $\text{Na}_{0.8}\text{Ni}_{0.4}\text{Ti}_{0.6}\text{O}_2$ shows no obvious exothermic peaks, indicating good thermal stability. And the exothermic temperatures of deeply desodiated materials (charging to 4 V as cathode) and sodiated materials (discharging to 0.01 V as anode), which are 364 °C and 345 °C respectively, appear higher than that of another layered sodium oxide.¹⁰² The high thermal stability at deeply desodiated and sodiated conditions probably contributes to the presence of stable TiNi layers in the crystal framework of this bi-polar material.

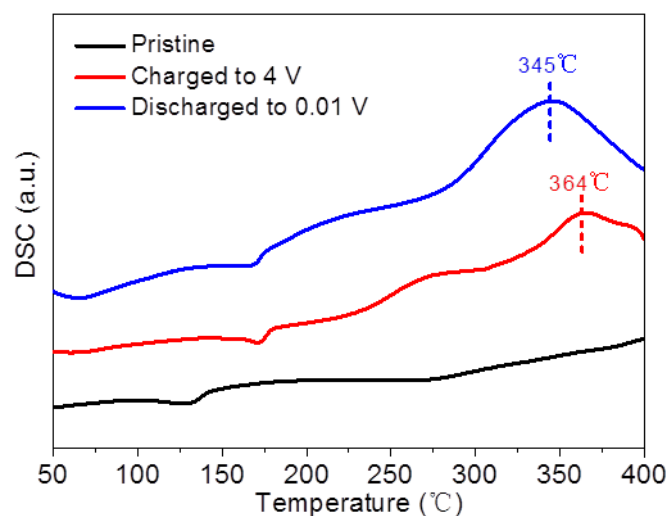


Figure 5.12 Differential scanning calorimetry (DSC) spectra of the pristine Na_{0.8}Ni_{0.4}Ti_{0.6}O₂, desodiated Na_{0.8-x}Ni_{0.4}Ti_{0.6}O₂ (charging to 4 V) and sodiated Na_{0.8+y}Ni_{0.4}Ti_{0.6}O₂ (discharging to 0.01 V).

5.4 Conclusions

In summary, a novel, symmetric sodium-ion battery delivers a maximum 96 Wh kg⁻¹ based on the mass of cathode and anode materials at a 0.2C rate, as well as performing an exceeding 75% capacity retention over a hundred and fifty cycles at a 1C charge-discharge rate. These properties, together with the good rate capability, low active material cost and the recycling convenience make this unique battery system more attractive for grid-related applications. Further work on the symmetric batteries optimization by substituting nickel with other transition metal is currently under investigation.

Chapter 6 conclusion

The main goal of this research work was to investigate the electrochemical performance of sodium titanium-based oxide, especially for layered structures, in both cathode and anode sides. Four titanium-based oxide electrode materials have been synthesized by traditional solid-state reaction, and their electrochemical properties are investigated in detail. It is demonstrated that titanium-substitution in either layered sodium nickel oxide or tunnel sodium manganese oxide can greatly smooth the charge-discharge curves, associated with the depression of complex phase transitions in the cathode side; layered titanium-containing oxide as negative electrode materials exhibit superior structural stability, and less capacity decay in cycling process as well as performing good rate capability.

In chapter 2, O3-type $\text{NaNi}_{0.5}\text{Ti}_{0.5}\text{O}_2$ with little impurity is synthesized by a solid-state method, and characterized by refined XRD, SEM and galvanostatic charge-discharge and CV tests. This material shows a layered structure with O3 phase and a layered morphology with particles size of 2-5 μm . O3-type $\text{NaTi}_{0.5}\text{Ni}_{0.5}\text{O}_2$ with redox couple of $\text{Ni}^{2+}/\text{Ni}^{4+}$ is explored as a cathode material for sodium ion battery. It exhibits electrochemical activity operating at an average potential of 3.1 V (vs Na^+/Na) and delivers a reversible capacity of 121 mAhg^{-1} at the current density of 20 mAg^{-1} . In addition, this material shows excellent cycle stability and rate capability. The cycle stability after 100 times electrochemical cycling can be 93.2%, and more than 60 % of discharge capacity can be gotten even at 5 C rate. The above results indicate its superiority as a promising positive electrode candidate for sodium ion battery.

In chapter 3, a tunnel manganese-substituted $\text{Na}_{0.61}\text{Ti}_{0.48}\text{Mn}_{0.52}\text{O}_2$ material is synthesized by a solid-state reaction, and its physical and chemical properties are investigated by ICP, refined XRD, SEM, TEM, FFT, EDX and galvanostatic charge-discharge tests. This material shows tunnel structure and typical sphere-like morphology with particle size of 400 nm, and it is explored as cathode of sodium-ion batteries by utilizing the redox couple of $\text{Mn}^{3+}/\text{Mn}^{4+}$ for the first time. It can deliver

a reversible discharge capacity of 86 mAh g^{-1} with an average voltage of 2.9 V at 0.2C rate in a sodium half cell, exhibiting good rate capability and capacity retention in the cut-off voltage of $1.5\text{-}4 \text{ V}$. The ex-situ XRD measurements in the different charge stage of the first cycle are carried out, which suggested that the original structure could stay unchanged before charge to 4.0 V , which is consistent with the dQ/dV analysis. Meanwhile, the structural stability supplies evidence for the stabilizer role of titanium in the cathode side. These results indicate that tunnel $\text{Na}_{0.61}\text{Ti}_{0.48}\text{Mn}_{0.52}\text{O}_2$ has a great potential application in large scale energy storage.

In chapter 4, the polytype $\text{Na}_{0.6}\text{Ti}_{0.4}\text{Cr}_{0.6}\text{O}_2$ materials with different phases of P2 and P3 were synthesized by adjusting the synthetic temperature and duration of heat treatment. The different oxygen stacking and transition metal layers numbers of the minimum repeating cell unit in P2 and P3 phases are revealed through refined X-ray powder diffraction (XRD) and scanning transmission electron microscopy (STEM) tests. The different local prismatic environment of Na ions and diffusion pathway in the P2 and P3 phases induce the different Na-ion mobility. Electrochemical test suggest that these P2 phase shows more evident plateau of 0.72 V , lower than that of P3, and a reversible capacity of 110 mAh g^{-1} , higher than that of P3. With a high rate of 10C , P2 phase still delivers a large capacity of 66 mAh g^{-1} , which is 56% of that at 0.2C rate. After 1000 cycles at 5C rate, the capacity retention is 77.5% . It is obvious that P2-type $\text{Na}_{0.6}\text{Ti}_{0.4}\text{Cr}_{0.6}\text{O}_2$ materials show more improved rate capability and cycling stability than P3, and it is a promising candidate for long-life and high-rate sodium-ion batteries. The DFT calculation clearly reveals the sodium diffusion barrier is greatly reduced when increasing multi-vacancies in P2 phase. It is surprisingly found that P2 has the lower sodium diffusion barrier than that of P3 in the case of multi-vacancy, which is consistent with rate capability test. The relationship between crystal structure-electrochemical performance is well established in P-type $\text{Na}_{0.6}\text{Ti}_{0.4}\text{Cr}_{0.6}\text{O}_2$ system for the first time, and this work combined experimental and computational method also provide new avenues for designing advanced electrode materials of sodium-ion batteries.

In chapter 5, a pure O3-type $\text{Na}_{0.8}\text{Ni}_{0.4}\text{Ti}_{0.6}\text{O}_2$ is synthesized by a solid-state reaction, and its structural and electrochemical properties are investigated by SXRD and refinement, SEM, STEM, SAED and galvanostatic charge-discharge tests. This material shows a typical O3-type layered structure, interconnected morphology with particle size of 100-500 nm and contains two electrochemically active transition metals with redox couples of $\text{Ni}^{4+}/\text{Ni}^{2+}$ and $\text{Ti}^{4+}/\text{Ti}^{3+}$ respectively, which has been characterized by charge-discharge test with two different voltage range of 2-4 V and 0.01-2.5 V. O3-type $\text{Na}_{0.8}\text{Ni}_{0.4}\text{Ti}_{0.6}\text{O}_2$ displays good cycling performance with high capacity retention after 250 cycles at 1C rate in both cathode and anode sides, and the detailed structural evolution is investigated by ex-situ XRD and TEM experiment. O3-P3 phase transition is observed in the cathode side during charge process, and most of P3 can be changed back to O3 during discharge process, while the original structure remain unchanged in anode side during charge and discharge process. This superiority of cathode and anode properties could be employed to implement a symmetric sodium cells. This $\text{Na}_{0.8}\text{Ni}_{0.4}\text{Ti}_{0.6}\text{O}_2$ -based symmetric cell exhibits a high voltage of 2.8 V, a reversible discharge capacity of 85 mAh g^{-1} , 75% capacity retention after 150 cycles and good rate capability. This full symmetric cell will greatly contribute to the development of room-temperature sodium-ion batteries towards safety, low cost, long life, and will stimulate further research on symmetric cells using the same active materials as both cathode and anode.

In general, fundamental and systematic research about sodium titanium-based oxides applied in sodium-ion batteries will expand a deeper understanding of the structure-electrochemical properties' relationship, and also provide new avenues for designing advanced electrode materials of sodium-ion batteries. These results about titanium-based materials in the cathode, anode, and even bipolar electrode will contribute to the development of room-temperature SIBs technology towards low cost and long life for large scale application.

List of publication

JOURNAL PAPERS

First author:

[1] Shaohua Guo, Haijun Yu, Pan Liu, Xizheng Liu, De Li, Mingwei Chen, Masayoshi Ishida and Haoshen Zhou, "Surface coating of lithium–manganese-rich layered oxides with delaminated MnO₂ nanosheets as cathode materials for Li-ion batteries", *J. Mater. Chem. A*, 2014, 2, 4422-4428

[2] Shaohua Guo, Haijun Yu, Zelang Jian, Pan Liu, Yanbei Zhu, Xianwei Guo, Mingwei Chen, Masayoshi Ishida, and Haoshen Zhou, "A High-Capacity, Low-Cost Layered Sodium Manganese Oxide Material as Cathode for Sodium-Ion Batteries", *ChemSusChem*, 2014, 7, 2115-2121

[3] Shaohua Guo, Haijun Yu, Dequan Liu, Wei Tian, Xizheng Liu, Nobuko Hanada, Masayoshi Ishida and Haoshen Zhou, "A novel tunnel Na_{0.61}Ti_{0.48}Mn_{0.52}O₂ cathode material for sodium-ion batteries", *Chem. Commun.*, 2014, 50, 7998-8001

[4] Shaohua Guo, Haijun Yu, Pan Liu, Yang Ren, Tao Zhang, Mingwei Chen, Masayoshi Ishida and Haoshen Zhou, "High-performance symmetric sodium-ion batteries using a new, bipolar O3-type material, Na_{0.8}Ni_{0.4}Ti_{0.6}O₂", *Energy Environ. Sci.*, 2015, 8, 1237-1244

[5] Shaohua Guo, Pan Liu, Haijun Yu, Yanbei Zhu, Mingwei Chen, Masayoshi Ishida, Haoshen Zhou, "A Layered P2- and O3-Type Composite as a High-Energy Cathode for Rechargeable Sodium-Ion Batteries", *Angew. Chem. Int. Ed.*, 2015, 54, 5894-5899

[6] Haijun Yu[‡], Shaohua Guo[‡], Yanbei Zhu, Masayoshi Ishida and Haoshen Zhou, "Novel titanium-based O3-type NaTi_{0.5}Ni_{0.5}O₂ as a cathode material for sodium ion batteries", *Chem. Commun.*, 2014, 50, 457-459

Co-authored

[1] Haijun Yu, Yumin Qian, Minoru Otani, Daiming Tang, Shaohua Guo, Yanbei Zhu and Haoshen Zhou, "Study of the lithium/nickel ions exchange in the layered $\text{LiNi}_{0.42}\text{Mn}_{0.42}\text{Co}_{0.16}\text{O}_2$ cathode material for lithium ion batteries: experimental and first-principles calculations", *Energy Environ. Sci.*, 2014, 7, 1068-1078

[2] Haijun Yu, Yang Ren, Dongdong Xiao, Shaohua Guo, Yanbei Zhu, Yumin Qian, Lin Gu, and Haoshen Zhou, "An Ultrastable Anode for Long-Life Room-Temperature Sodium-Ion Batteries", *Angew. Chem. Int. Ed.*, 2014, 53, 8963-8969

PRESENTATIONS

[1] Shaohua Guo, Haijun Yu, Xizheng Liu, Masayoshi Ishida and Haoshen Zhou, "Li-rich layered oxide materials coated with delaminated MnO_2 nanosheets" The 54th Battery Symposium in Japan, 2A20, 2013 (oral)

[2] Shaohua Guo, Haijun Yu, Masayoshi Ishida and Haoshen Zhou, "A cycle-stable sodium Ti-based cathode for sodium-ion batteries" The 9th Energy Technology Symposium in Tsukuba, B-1, 2014 (oral)

[3] Shaohua Guo, Haijun Yu, Masayoshi, Ishida and Haoshen Zhou, "Role of Lattice Water in High-Capacity Layered $\text{NaMn}_3\text{O}_5 \cdot n\text{H}_2\text{O}$ Materials as Cathode of Sodium-Ion Batteries" 17th International Meeting on Lithium Batteries, 331, 2014 (poster)

Acknowledgement

First of foremost, I would like to express my sincere gratitude to my supervisors, Prof. Masayoshi Ishida (University of Tsukuba) and Prof. Haoshen Zhou (AIST and University of Tsukuba), for their continuous support and help during my whole doctoral research. The meticulous care and guidance from Prof. Ishida let me to live a happy life in our lab as well as everyday life. The patience, perspective, motivation and encouragements from Prof. Zhou take me to overcome a series of difficulties in scientific research, and set samples and goals for me to continue the research work in the future.

I also would like to Assistant Prof. Nobuko Hanada (University of Tsukuba), Assistant Prof. Tomonori Nakayama (University of Tsukuba) and Dr. Hirofumi Matsuda (AIST) for their very valuable suggestion and advice.

I would like to express my sincere thanks to all the professors and colleagues in Energy Interface Technology Group of AIST and Energy Conversion Lab. of University of Tsukuba. I will keep on record my special thanks to Dr. Haijun Yu in AIST group, who helped me to start my initial experiments and make progress in my research work. Thanks to Dr. Tao Zhang, Dr. De Li, Dr. Zelang Jian, Dr. Zhiping Song, Dr. Fujun Li, Dr. Xizheng Liu, Dr. Chaofeng Zhang, Dr. Jin Yi, Dr. Yang Sun, Dr. Kaiming Liao, Dr. Na Li, Mr. Kai Zhu and Mrs. Qi Li in the AIST group, Mrs. Thu, Mr. Ahn, Mr. Yosua and Mrs. Klaudia in the university group. Thanks to Prof. Mingwei Chen, Dr. Pan Liu and Dr. Yanbei Zhu for their kindly assistance in TEM or ICP measurement.

I would like to thank the financial support provided by the China Scholarship Council.

Lastly, I want to thank my family for the essential role they have played during my entire doctoral program. To my parents, Ziquan Guo and Xiu'e Xue—your love and affection supply enough power to me. To my older sister, Xiaohua Guo—I am indebted to your encouragement. To my wife, Lihua Zhao and my son, Haocheng Guo—your love is my mental strength forever.

REFERENCE

1. Z. Yang, J. Zhang, M. C. Kintner-Meyer, X. Lu, D. Choi, J. P. Lemmon and J. Liu, *Chem. Rev.*, 2011, **111**, 3577-3613.
2. J. Liu, J. G. Zhang, Z. Yang, J. P. Lemmon, C. Imhoff, G. L. Graff, L. Li, J. Hu, C. Wang and J. Xiao, *Advanced Functional Materials*, 2013, **23**, 929-946.
3. J.-M. Tarascon and M. Armand, *Nature*, 2001, **414**, 359-367.
4. J. B. Goodenough and Y. Kim, *Chemistry of Materials*, 2009, **22**, 587-603.
5. S. W. Kim, D. H. Seo, X. Ma, G. Ceder and K. Kang, *Advanced Energy Materials*, 2012, **2**, 710-721.
6. H. Pan, Y.-S. Hu and L. Chen, *Energy & Environmental Science*, 2013, **6**, 2338-2360.
7. J. Braconnier, C. Delmas and P. Hagenmuller, *Materials Research Bulletin*, 1982, **17**, 993-1000.
8. A. Maazaz, C. Delmas and P. Hagenmuller, *Journal of inclusion phenomena*, 1983, **1**, 45-51.
9. C. Fouassier, C. Delmas and P. Hagenmuller, *Materials Research Bulletin*, 1975, **10**, 443-449.
10. M. S. Whittingham, *Chem Rev*, 2004, **104**, 4271-4301.
11. M. Armand and J.-M. Tarascon, *Nature*, 2008, **451**, 652-657.
12. N. Yabuuchi, K. Kubota, M. Dahbi and S. Komaba, *Chemical reviews*, 2014, **114**, 11636-11682.
13. D. Kundu, E. Talaie, V. Duffort and L. F. Nazar, *Angewandte Chemie International Edition*, 2015, **54**, 3431-3448.
14. M. Guignard, C. Didier, J. Darriet, P. Bordet, E. Elkaim and C. Delmas, *Nat Mater*, 2013, **12**, 74-80.
15. C. Didier, M. Guignard, C. Denage, O. Szajwaj, S. Ito, I. Saadoune, J. Darriet and C. Delmas, *Electrochem Solid St*, 2011, **14**, A75-A78.
16. I. Saadoune, A. Maazaz, M. Menetrier and C. Delmas, *J Solid State Chem*, 1996, **122**, 111-117.
17. J. J. Ding, Y. N. Zhou, Q. Sun and Z. W. Fu, *Electrochem Commun*, 2012, **22**, 85-88.
18. Y. Sun, L. Zhao, H. L. Pan, X. Lu, L. Gu, Y. S. Hu, H. Li, M. Armand, Y. Ikuhara, L. Q. Chen and X. J. Huang, *Nat Commun*, 2013, **4**.
19. C. Delmas, C. Fouassier and P. Hagenmuller, *Physica B+ C*, 1980, **99**, 81-85.
20. S. Guo, P. Liu, H. Yu, Y. Zhu, M. Chen, M. Ishida and H. Zhou, *Angewandte Chemie*, 2015.
21. E. Lee, J. Lu, Y. Ren, X. Luo, X. Zhang, J. Wen, D. Miller, A. DeWahl, S. Hackney and B. Key, *Advanced Energy Materials*, 2014.
22. N. Yabuuchi, R. Hara, M. Kajiyama, K. Kubota, T. Ishigaki, A. Hoshikawa and S. Komaba, *Advanced Energy Materials*, 2014, **4**.
23. Z. Jian, W. Han, X. Lu, H. Yang, Y. S. Hu, J. Zhou, Z. Zhou, J. Li, W. Chen and D. Chen, *Advanced Energy Materials*, 2013, **3**, 156-160.
24. S.-M. Oh, S.-T. Myung, J. Hassoun, B. Scrosati and Y.-K. Sun, *Electrochemistry Communications*, 2012, **22**, 149-152.

25. A. William III, *Energy & Environmental Science*, 2015.
26. M. D. Slater, D. Kim, E. Lee and C. S. Johnson, *Advanced Functional Materials*, 2013, **23**, 947-958.
27. S. Guo, H. Yu, P. Liu, X. Liu, C. Mingwei, M. Ishida and H. Zhou, *Journal of Materials Chemistry A*, 2014.
28. Y. Lu, L. Wang, J. Cheng and J. B. Goodenough, *Chemical communications*, 2012, **48**, 6544-6546.
29. J. Song, L. Wang, Y. Lu, J. Liu, B. Guo, P. Xiao, J.-J. Lee, X.-Q. Yang, G. Henkelman and J. B. Goodenough, *J. Am. Chem. Soc.*, 2015, **137**, 2658-2664.
30. S. Komaba, W. Murata, T. Ishikawa, N. Yabuuchi, T. Ozeki, T. Nakayama, A. Ogata, K. Gotoh and K. Fujiwara, *Advanced Functional Materials*, 2011, **21**, 3859-3867.
31. Y. Wang, X. Yu, S. Xu, J. Bai, R. Xiao, Y.-S. Hu, H. Li, X.-Q. Yang, L. Chen and X. Huang, *Nature communications*, 2013, **4**.
32. H. Yu, Y. Ren, D. Xiao, S. Guo, Y. Zhu, Y. Qian, L. Gu and H. Zhou, *Angewandte Chemie*, 2014, **126**, 9109-9115.
33. Y. Xu, Y. Zhu, Y. Liu and C. Wang, *Advanced Energy Materials*, 2013, **3**, 128-133.
34. J. Qian, X. Wu, Y. Cao, X. Ai and H. Yang, *Angewandte Chemie*, 2013, **125**, 4731-4734.
35. J. B. Goodenough and Y. Kim, *Chemistry of Materials*, 2010, **22**, 587-603.
36. J. M. Tarascon and M. Armand, *Nature*, 2001, **414**, 359-367.
37. H. J. Yu and H. S. Zhou, *J Phys Chem Lett*, 2013, **4**, 1268-1280.
38. J. F. Qian, M. Zhou, Y. L. Cao, X. P. Ai and H. X. Yang, *Adv Energy Mater*, 2012, **2**, 410-414.
39. R. Berthelot, D. Carlier and C. Delmas, *Nat Mater*, 2011, **10**, 74-U73.
40. E. Hosono, T. Saito, J. Hoshino, M. Okubo, Y. Saito, D. Nishio-Hamane, T. Kudo and H. S. Zhou, *J Power Sources*, 2012, **217**, 43-46.
41. Y. Kawabe, N. Yabuuchi, M. Kajiyama, N. Fukuhara, T. Inamasu, R. Okuyama, I. Nakai and S. Komaba, *Electrochem Commun*, 2011, **13**, 1225-1228.
42. P. Vassilaras, X. H. Ma, X. Li and G. Ceder, *J Electrochem Soc*, 2013, **160**, A207-A211.
43. X. H. Ma, H. L. Chen and G. Ceder, *J Electrochem Soc*, 2011, **158**, A1307-A1312.
44. B. M. de Boisse, D. Carlier, M. Guignard and C. Delmas, *J Electrochem Soc*, 2013, **160**, A569-A574.
45. N. Yabuuchi, M. Kajiyama, J. Iwatate, H. Nishikawa, S. Hitomi, R. Okuyama, R. Usui, Y. Yamada and S. Komaba, *Nat Mater*, 2012, **11**, 512-517.
46. S. Komaba, N. Yabuuchi, T. Nakayama, A. Ogata, T. Ishikawa and I. Nakai, *Inorg Chem*, 2012, **51**, 6211-6220.
47. S. Komaba, T. Ishikawa, N. Yabuuchi, W. Murata, A. Ito and Y. Ohsawa, *Acs Appl Mater Inter*, 2011, **3**, 4165-4168.
48. Z. Jian, W. Han, X. Lu, H. Yang, Y. S. Hu, J. Zhou, Z. Zhou, J. Li, W. Chen and D. Chen, *Advanced Energy Materials*, 2012.
49. C. S. Park, H. Kim, R. A. Shakoob, E. Yang, S. Y. Lim, R. Kahraman, Y. Jung and J. W. Choi, *Journal of the American Chemical Society*, 2013, **135**, 2787-2792.
50. Y. You, X.-L. Wu, Y.-X. Yin and Y.-G. Guo, *Journal of Materials Chemistry A*, 2013,

- 1, 14061-14065.
51. Y. You, X.-L. Wu, Y.-X. Yin and Y.-G. Guo, *Energy & Environmental Science*, 2014, **7**, 1643-1647.
 52. J. Song, M. Xu, L. Wang and J. B. Goodenough, *Chemical Communications*, 2013, **49**, 5280-5282.
 53. M. Guignard, C. Didier, J. Darriet, P. Bordet, E. Elkaïm and C. Delmas, *Nature materials*, 2012.
 54. D. Su, C. Wang, H. j. Ahn and G. Wang, *Chemistry-A European Journal*, 2013, **19**, 10884-10889.
 55. X. Xia and J. Dahn, *Electrochemical and Solid-State Letters*, 2011, **15**, A1-A4.
 56. R. Berthelot, D. Carlier and C. Delmas, *Nature materials*, 2011, **10**, 74-80.
 57. E. Hosono, T. Saito, J. Hoshino, M. Okubo, Y. Saito, D. Nishio-Hamane, T. Kudo and H. Zhou, *Journal of Power Sources*, 2012, **217**, 43-46.
 58. Y. Cao, L. Xiao, W. Wang, D. Choi, Z. Nie, J. Yu, L. V. Saraf, Z. Yang and J. Liu, *Advanced Materials*, 2011, **23**, 3155-3160.
 59. H. Yu, S. Guo, Y. Zhu, M. Ishida and H. Zhou, *Chemical Communications*, 2014, **50**, 457-459.
 60. H. Yoshida, N. Yabuuchi, K. Kubota, I. Ikeuchi, A. Garsuch, M. Schulz-Dobrick and S. Komaba, *Chemical Communications*, 2014, **50**, 3677-3680.
 61. A. C. Larson and R. B. Von Dreele, *General Structure Analysis System. LANSCE, MS-H805, Los Alamos, New Mexico*, 1994.
 62. B. H. Toby, *Journal of Applied Crystallography*, 2001, **34**, 210-213.
 63. Y. Jeong and A. Manthiram, *Journal of Solid State Chemistry*, 2001, **156**, 331-338.
 64. Y. Jeong and A. Manthiram, *Electrochemical and solid-state letters*, 1999, **2**, 421-424.
 65. J. Awaka, J. Akimoto, H. Hayakawa, Y. Takahashi, N. Kijima, M. Tabuchi, H. Sakaebe and K. Tatsumi, *Journal of Power Sources*, 2007, **174**, 1218-1223.
 66. J. Akimoto, H. Hayakawa, N. Ishida, F. Funabiki, N. Kijima, H. Shibuya and J. Imaizumi, *Journal of Power Sources*, 2013, **244**, 382-388.
 67. D. Kim, S. H. Kang, M. Slater, S. Rood, J. T. Vaughey, N. Karan, M. Balasubramanian and C. S. Johnson, *Advanced Energy Materials*, 2011, **1**, 333-336.
 68. N. Yabuuchi, R. Hara, M. Kajiyama, K. Kubota, T. Ishigaki, A. Hoshikawa and S. Komaba, *Advanced Energy Materials*, 2014.
 69. D. H. Lee, J. Xu and Y. S. Meng, *Physical Chemistry Chemical Physics*, 2013, **15**, 3304-3312.
 70. Y. H. Jung, A. S. Christiansen, R. E. Johnsen, P. Norby and D. K. Kim, *Advanced Functional Materials*, 2015.
 71. S. P. Ong, V. L. Chevrier, G. Hautier, A. Jain, C. Moore, S. Kim, X. Ma and G. Ceder, *Energy & Environmental Science*, 2011, **4**, 3680-3688.
 72. S. Guo, H. Yu, P. Liu, Y. Ren, T. Zhang, M. Chen, M. Ishida and H. Zhou, *Energy & Environmental Science*, 2015, **8**, 1237-1244.
 73. M. Guignard, C. Didier, J. Darriet, P. Bordet, E. Elkaïm and C. Delmas, *Nature materials*, 2013, **12**, 74-80.
 74. Y. S. Wang, X. Q. Yu, S. Y. Xu, J. M. Bai, R. J. Xiao, Y. S. Hu, H. Li, X. Q. Yang, L.

- Q. Chen and X. J. Huang, *Nature Communications*, 2013, **4**.
75. A. Rudola, K. Saravanan, C. W. Mason and P. Balaya, *Journal of Materials Chemistry A*, 2013, **1**, 2653-2662.
 76. M. Shirpour, J. Cabana and M. Doeff, *Energy & Environmental Science*, 2013, **6**, 2538-2547.
 77. W. Weppner and R. A. Huggins, *Journal of The Electrochemical Society*, 1977, **124**, 1569-1578.
 78. S. Guo, H. Yu, Z. Jian, P. Liu, Y. Zhu, X. Guo, M. Chen, M. Ishida and H. Zhou, *ChemSusChem*, 2014, **7**, 2115-2119.
 79. K. Momma and F. Izumi, *Journal of Applied Crystallography*, 2008, **41**, 653-658.
 80. G. Kresse and J. Furthmüller, *Physical Review B*, 1996, **54**, 11169.
 81. P. E. Blöchl, *Physical Review B*, 1994, **50**, 17953.
 82. J. P. Perdew, K. Burke and M. Ernzerhof, *Physical review letters*, 1996, **77**, 3865.
 83. G. Mills, H. Jónsson and G. K. Schenter, *Surface Science*, 1995, **324**, 305-337.
 84. B. Dunn, H. Kamath and J.-M. Tarascon, *Science*, 2011, **334**, 928-935.
 85. H.-G. Jung, M. W. Jang, J. Hassoun, Y.-K. Sun and B. Scrosati, *Nature communications*, 2011, **2**, 516.
 86. S. W. Lee, N. Yabuuchi, B. M. Gallant, S. Chen, B.-S. Kim, P. T. Hammond and Y. Shao-Horn, *Nature Nanotechnology*, 2010, **5**, 531-537.
 87. C. K. Chan, H. Peng, G. Liu, K. McIlwrath, X. F. Zhang, R. A. Huggins and Y. Cui, *Nature nanotechnology*, 2007, **3**, 31-35.
 88. B. Kang and G. Ceder, *Nature*, 2009, **458**, 190-193.
 89. M. Pasta, C. D. Wessells, R. A. Huggins and Y. Cui, *Nature communications*, 2012, **3**, 1149.
 90. N. Yabuuchi, M. Kajiyama, J. Iwatate, H. Nishikawa, S. Hitomi, R. Okuyama, R. Usui, Y. Yamada and S. Komaba, *Nature materials*, 2012, **11**, 512-517.
 91. P. Barpanda, G. Oyama, C. D. Ling and A. Yamada, *Chemistry of Materials*, 2014, **26**, 1297-1299.
 92. S. Wang, L. Wang, Z. Zhu, Z. Hu, Q. Zhao and J. Chen, *Angewandte Chemie*, 2014, **126**, 6002-6006.
 93. D. Su and G. Wang, *ACS nano*, 2013, **7**, 11218-11226.
 94. X. Shu-Yin, W. Xiao-Yan, L. Yun-Ming, H. Yong-Sheng and C. Li-Quan, *Chinese Physics B*, 2014, **23**, 118202.
 95. R. Shanmugam and W. Lai, *ECS Electrochemistry Letters*, 2014, **3**, A23-A25.
 96. Y.-U. Park, D.-H. Seo, H.-S. Kwon, B. Kim, J. Kim, H. Kim, I. Kim, H.-I. Yoo and K. Kang, *Journal of the American Chemical Society*, 2013, **135**, 13870-13878.
 97. S. Y. Lim, H. Kim, J. Chung, J. H. Lee, B. G. Kim, J.-J. Choi, K. Y. Chung, W. Cho, S.-J. Kim and W. A. Goddard, *Proceedings of the National Academy of Sciences*, 2014, **111**, 599-604.
 98. S. K. Martha, J. Nanda, Y. Kim, R. R. Unocic, S. Pannala and N. J. Dudney, *J Mater Chem A*, 2013, **1**, 5587-5595.
 99. Y. Yue, A. J. Binder, B. Guo, Z. Zhang, Z. A. Qiao, C. Tian and S. Dai, *Angewandte Chemie*, 2014, **126**, 3198-3201.
 100. J. Xu, D. H. Lee, R. J. Clément, X. Yu, M. Leskes, A. J. Pell, G. Pintacuda, X.-Q.

- Yang, C. P. Grey and Y. S. Meng, *Chemistry of Materials*, 2014, **26**, 1260-1269.
101. B. Jache and P. Adelhelm, *Angewandte Chemie International Edition*, 2014, **53**, 10169-10173.
102. S.-M. Oh, S.-T. Myung, C. S. Yoon, J. Lu, J. Hassoun, B. Scrosati, K. Amine and Y.-K. Sun, *Nano letters*, 2014, **14**, 1620-1626.
103. L. S. Plashnitsa, E. Kobayashi, Y. Noguchi, S. Okada and J.-i. Yamaki, *Journal of the Electrochemical Society*, 2010, **157**, A536-A543.
104. P. Senguttuvan, G. Rousse, M. Arroyo y de Dompablo, H. Vezin, J.-M. Tarascon and M. Palacín, *J. Am. Chem. Soc.*, 2013, **135**, 3897-3903.
105. S. Li, Y. Dong, L. Xu, X. Xu, L. He and L. Mai, *Advanced Materials*, 2014.
106. E. Kobayashi, L. S. Plashnitsa, T. Doi, S. Okada and J.-i. Yamaki, *Electrochemistry Communications*, 2010, **12**, 894-896.
107. Y. Noguchi, E. Kobayashi, L. S. Plashnitsa, S. Okada and J.-i. Yamaki, *Electrochimica Acta*, 2013, **101**, 59-65.
108. P. Vassilaras, X. Ma, X. Li and G. Ceder, *Journal of The Electrochemical Society*, 2013, **160**, A207-A211.
109. H. Yu, Y. Ren, D. Xiao, S. Guo, Y. Zhu, Y. Qian, L. Gu and H. Zhou, *Angewandte Chemie*, 2014.
110. Y.-J. Shin and M.-Y. Yi, *Solid State Ionics*, 2000, **132**, 131-141.
111. Y.-J. Shin, M.-H. Park, J.-H. Kwak, H. Namgoong and O. H. Han, *Solid State Ionics*, 2002, **150**, 363-372.
112. S. Komaba, T. Nakayama, A. Ogata, T. Shimizu, C. Takei, S. Takada, A. Hokura and I. Nakai, *ECS Transactions*, 2009, **16**, 43-55.
113. M. Sathya, K. Hemalatha, K. Ramesha, J.-M. Tarascon and A. Prakash, *Chemistry of Materials*, 2012, **24**, 1846-1853.
114. I. Saadoune, A. Maazaz, M. Ménérier and C. Delmas, *Journal of Solid State Chemistry*, 1996, **122**, 111-117.